Dissertation submitted to the
Combined Faculties of the Natural Sciences and for Mathematics
of the Ruperto–Carola University of Heidelberg, Germany,
for the degree of Doctor of Natural Sciences

Equipartition and mass segregation

Simulations of star clusters with two mass–components

presented by
Dipl.–Phys. Emil Khalisi
born in Khalis

Oral examination: 2002, November 6th

Equipartition and mass segregation

Simulations of star clusters
with two mass–components

Emil Khalisi

Referees: Priv.–Doz. Dr. Rainer Spurzem
Prof. Dr. Hans–Walter Rix

Zusammenfassung

Äquipartition und Massensegregation

Die dynamische Entwicklung von isolierten, selbstgravitierenden Systemen wird unter den Gesichtspunkten der Massensegregation und Äquipartition untersucht. Wir analysieren idealisierte Sternhaufen mit zwei unterschiedlichen Massenkomponenten, deren individuelles Massenverhältnis $\mu = m_2/m_1$ zwischen 1,25 und 50 variiert. Der Gesamtanteil der schweren Komponente beträgt zwischen 5% und 40% des Haufens. Wir untersuchen die Eigenschaften wie den Kernkollaps, die Entwicklung des Zentralpotentials, die radiale Massenschichtung ebenso wie entweichende Sterne. Wir stellen neue Präzisionsrechnungen, sogenannte N–body–Simulationen, vor, die mit dem Programm NBODY6++ gewonnen wurden. Wir modellierten bis zu 20.000 Teilchen auf dem Parallelrechner CRAY T3E, während die statistische Signifikanz der Simulationen mit niedrigeren Teilchenzahlen durch Mittelung mehrerer Rechnungen erhöht wurde.

Unser Ziel ist es, die unterschiedlichen Theorien zur Sternentstehung und die dynamische Entwicklung zu untersuchen. Wir haben wesentliche Abweichungen der Entwicklungszeitskala im Bereich $\mu \to 1$ erkannt. Die Äquipartition bremst die gravothermische Kontraktion im Kern leicht ab. Jenseits eines kritischen Wertes von $\mu \approx 2$ kann sich keine Äquipartition unter den Masseteilchen einstellen, ein Phänomen, das als "Spitzersche Äquipartitionsinstabilität" bekannt ist; die schwere Komponente entkoppelt sich und kollabiert unter dem Einfluß der eigenen gravothermischen Instabilität. Die kritische Grenze zwischen den Spitzer–stabilen und –unstabilen Systemen wurde zum ersten Male in direkten N–body–Modellen aufgezeigt.

Abstract

Equipartition and mass segregation

The dynamical evolution of an isolated self–gravitating system is studied under the aspects of mass segregation and equipartition processes. We analyse the idealized case of a cluster with two distinct mass components. The individual ratio of the heavy to light bodies, $\mu = m_2/m_1$, is varied from 1.25 to 50.0 and the fraction of the total heavy mass is altered from 5% to 40% of the whole cluster. We also examine the cluster properties like the core collapse, the evolution of the central potential, the radial stratification of masses as well as escapers. We present new, high–accuracy collisional N–body simulations, using the high–order integrator NBODY6++. We modelled up to $N = 20{,}000$ particles on the parallel supercomputer CRAY T3E, and the statistical significancy of the lower–N simulations was improved by ensemble averages.

Our objective is to check the various theories on early star formation and dynamical evolution. We find significant deviations of the evolutionary time scale in the regime $\mu \to 1$. Equipartition slows down the gravothermal contraction of the core slightly. Beyond a critical value of $\mu \approx 2$, no equipartition can be achieved between the different masses, a phenomenon known as the Spitzer equipartition instability; the heavy component decouples and collapses under the influence of the gravothermal instability of its own subsystem. For the first time the critical boundary between Spitzer–stable and –unstable systems is demonstrated in direct N–body models.

Table of contents

1 Introduction

Stellar clusters like globular or open star clusters are a collection of many stars held together by their aggregate gravity. The simple case of a certain number of point–like masses suffering no more than the Newtonian law of gravity has incited modern astronomy to construct mathematical models in order to trace its global properties. Their research covers a vast amount of territory, e.g. stellar evolution, chemical enrichment, origins of the Universe, or galactic dynamics. Star clusters now serve as laboratories for testing astrophysical theories. Extensively studied for more than a century, they continue to yield surprising results and challenge our understanding.

It was only in the recent four decades that this field of research grew dramatically, while giving new and surprising insights into the astrophysical processes: On the theoretical side, the development of high–speed computers ventured numerical simulations with hardware and software improvements providing models with high particle numbers and excellent accuracy. On the observational side, CCD–technique combined with high spatial resolution allowed the analysis of faint objects even in the star–crowded fields of globular clusters. These clusters turned out to be a fundamental unit of astrophysics: They are the oldest known objects, close in proximity to the origin of the Universe and the sole surviving structures of the first stages in the formation of the Galaxy. As such they give us "an unparalleled opportunity to probe the depths of time that are the remotest to reach" (Ivan King).

In this broad and fascinating field of research of star clusters, we present a work particularly dealing with the segregation of masses in such stellar systems. Taken for itself, this subject has been touched several times in literature on stellar dynamics, but we wish to contribute to the rapidly advancing science by the present thesis, and try to reveal new, unknown details explaining how segregation works. The thesis is divided in two parts: In a more general one, we introduce stepwise the theoretical concepts of equipartition and the segregation of masses. Although the handling of the computational method is also a significant part of the work, we will sketch the main features of the software only briefly and refer to the more detailed publications. In the second, more specific part, we describe the simulation models as well as their initial conditions. We present the results of a wide parameter space, which has been exploited by direct N–body modelling for the first time. We also extract the important parameters governing the speed up of core collapse and equipartition of energies.

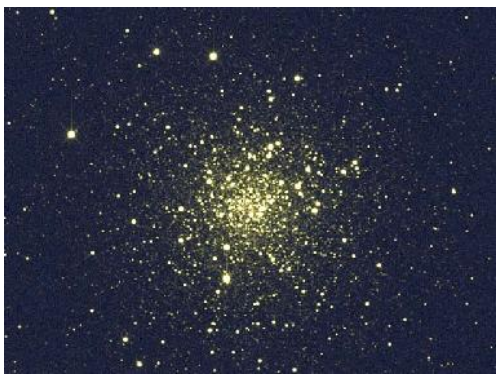

Figure 1.1: Globular cluster M 12 at a distance of 5 kpc has a diameter of 20 pc.

2 Historical cornerstones

During the first two centuries in the modern age, when stellar clusters were realized to be a huge swarm of stars in close vicinity to each other, the interest on them was rather an observational one: descriptions of appearance, locations on the sky, and first star counts for estimation purposes. This observational branch brought to light a heap of milestones in astrophysical research and still continues yielding more detailed information about the dynamics, the structures and the constituency of clusters as well as the properties of some of their particular members.

In the early years of the 20^{th} century, the first theoretical aspects were awaken by some studies of the radial density profiles and their physical cause. The statistical arrangement of stars in globular clusters was described by H.C. Plummer (1911), who found by means of star counts that the law $\rho(r) \propto (1 + r^2)^{-\frac{5}{2}}$ fits the observed distribution best, where ρ denotes the density at the radius r from the centre.

At the beginning of the 1940's, the cluster theory was extended to the formulation of the basic equations how a star assembly behaves and "relaxes" under its self–gravity (Spitzer 1940, Chandrasekhar 1942). Essential contributions were made on stellar encounters, investigating how a star's orbit would change if it is drowned into a sea of other stars that build up an approximately smooth potential (Fig. 2.1). The idea of the relaxation processes was introduced as well as the corresponding time scales.

Another breakthrough occurred in the early 1960's with a burst of papers by King (1962, 1966), Michie (1963) and Hénon (1965) among others. They analyzed the long–term consequences of stellar encounters and concluded that a cluster must evolve dynamically to various phases: On one hand the slow dissolution by evaporation due to escaping stars, on the other hand a rapid infall of the central parts merging into a singularity. This latter concept was called the "core collapse" and it was further investigated by Antonov (1962) and Lynden–Bell & Wood (1968). It became obvious that the structure of the cluster is intimately linked with its evolutionary stage, and vice versa. However, both models — the evaporation by King and Michie as well as Hénon's core collapse — turned out very successful.

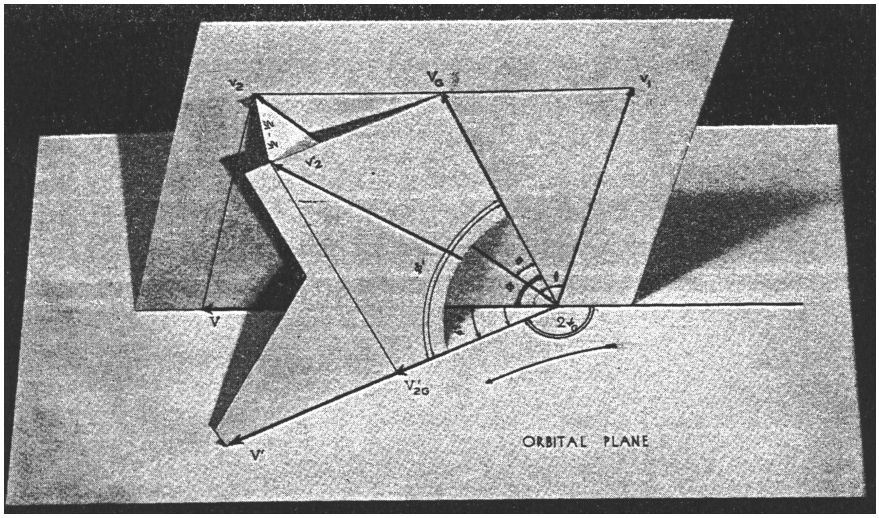

Figure 2.1: Trajectories of a stellar encounter modelled with cardboards to illustrate deflections (Chandrasekhar 1942).

The models were accompanied by a third branch of research: numerical simulations. In his pioneering work, von Hoerner (1960) performed calculations with $N = 16$ particles on the best computers available at that time. Such direct integrations of the gravitational force between each particle

have merged into the so–called "N–body simulations". Rapid improvements in computer technology (both hard– and software) soon facilitated larger as well as more accurate calculations. By the end of the $20^{\rm th}$ century, the amount of 10,000 particles was bridged (Spurzem & Aarseth 1996), and parallel machines and special purpose computers do even manage ten times more nowadays. The simulations had to be compared with theory, and the plausibility of a theory was controlled by the observational reality. For such comparisons, models should be as simple as possible and the simulations as realistic as possible.

N–body calculations have the advantage to yield most accurate results, but computational effort restricts them to relatively small particle numbers. Other algorithms have been developed which enable dynamical simulations of galaxies or large–scale structures of the Universe. The statistical methods could replace the "exact" solutions and disclose new physical processes: Fluid–dynamical models, Monte–Carlo–techniques, hierarchically structured mesh–codes as well as mixtures of them. Studying the post–collapse evolution of globular clusters with a gaseous model, Sugimoto & Bettwieser (1983) discovered gravothermal oscillations, i.e. a multiple contraction and expansion of the high–density core. The oscillations showed an amplitude of a factor as large as 10^6 in the central density (Fig. 2.2). Their simulations resolved the long–standing question why there are only some few globular clusters that are observed in a collapsed stage: The re–expansion of the core restores the system to a low–density state where it spends most of its time.

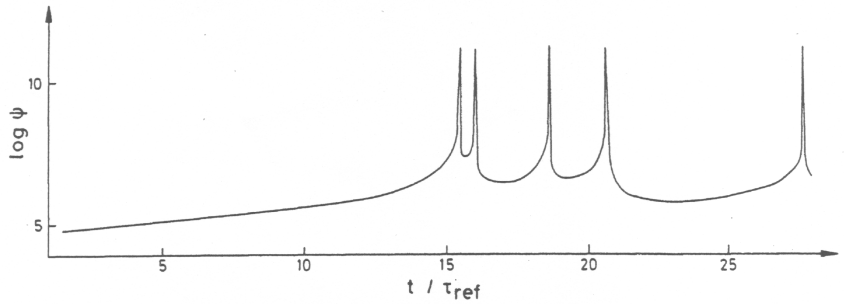

Figure 2.2: Central density plotted against time in units of the relaxation time (Sugimoto & Bettwieser 1983).

On the observational side again, the Hubble Space Telescope opened up new horizons and gave an opportunity to a check the theories. Being able to dissolve individual stars even in the most crowded areas of a collapsed cluster like M 15, it fixes a moment of positions which may be able to illustrate movements when successive observations would follow. Also, the theoretical research is still on work: Step by step, realistic models of star clusters are built up containing a mass spectrum, early–phase formation, stellar evolution, gas dynamics or chemistry.

A recent review on the scientific stage can be found in Meylan & Heggie (1997) or in the Proceedings of the star2000–Conference (Deiters *et al.* 2001) and the references therein.

3 Analytical models for clusters

A number of analytic models has been obtained to characterize star clusters mathematically. These models are based on simplifying assumptions regarding the environment and the initial conditions, and they are solutions of more general equations. The commonest way of defining a model of a star cluster is in terms of its distribution function $f(\mathbf{r}, \mathbf{v}, m)$, which defines the number of stars with positions in a small volume of space $d^3\mathbf{r}$, velocities in the range $d^3\mathbf{v}$ and masses in the interval dm; if evolution is considered, the function depends also on time t. In terms of this description a fairly general equation for the dynamical evolution is Boltzmann's equation:

$$\frac{\partial f}{\partial t} + \mathbf{v} \cdot \nabla f - \nabla \Phi \cdot \frac{\partial f}{\partial \mathbf{v}} = \left(\frac{\partial f}{\partial t} \right)_{\rm enc}, \tag{1}$$

where Φ is the smoothed gravitational potential, and the right–hand side describes the effect of two–body encounters. Under certain assumptions, however, the Boltzmann equation can be simplified greatly. If the system is self–gravitating, the distribution function f must correspond to the density ρ in order to provide its own potential Φ (Poisson's equation):

$$\nabla^2 \Phi = 4\pi G \rho, \tag{2}$$

with G being the Gravitational constant. Equations (1) and (2) are generally valid and may be applied to the evolution of a system. Depending on the approach, many different kind of models can be constructed (Binney & Tremaine 1987; Spitzer 1987; Meylan & Heggie 1997).

1. The simplest model is a sphere with the stars moving around the centre. For a constant density ρ, the tangential velocity $v_{\rm t}$ is just balancing the centrifugal force, while the radial distance remains unchanged. $v_{\rm t}$ varies with r as

   $$v_{\rm t}^2 = GM(r)/r \quad \text{and} \quad v_{\rm r} = 0. \tag{3}$$

   All stars have the same period of revolution about the centre, but a random distribution of orbital planes.

2. In the isothermal sphere the radial density distribution is

   $$\rho(r) = \frac{\langle v^2 \rangle}{2\pi G r^2}, \tag{4}$$

   and $\langle v^2 \rangle$ means the velocity dispersion. The distribution of velocities (dispersion) is isotropic everywhere as found in gases of statistical equilibrium. Unfortunately, this model cannot serve as a realistic one because it has infinite mass, $M(r) = \int \rho(r) 4\pi r^2 dr \propto r$. Nevertheless, it is a useful approximation for parts of a cluster.

3. The Plummer sphere is frequently used by theorists for analytical convenience. It provides a good fit to the observations of some globular clusters with a compact core and an extended outer envelope. The radial density distribution is

   $$\rho(r) = \frac{3M}{4\pi R^3} \cdot \frac{1}{(1 + r^2/R^2)^{5/2}} \tag{5}$$

   with M being the total mass and R a scaling radius (see Ch. 8.3). On application to real clusters this model fails at large radii, because the outer parts of elliptical galaxies fall off less steeply than $\rho \propto r^{-4}$ while the Plummer model continues its decline $\propto r^{-5}$.

   It can be shown that the isothermal and the Plummer sphere pursue the density distribution of a polytropic gas sphere, which is described by $p = k\,\rho^\gamma$, where p is the pressure that varies with the density ρ, k is a constant and γ the "polytropic (adiabatic) index", identical with the ratio of heat capacities, $\gamma \equiv c_{\rm p}/c_{\rm V}$ (Binney & Tremaine 1987).

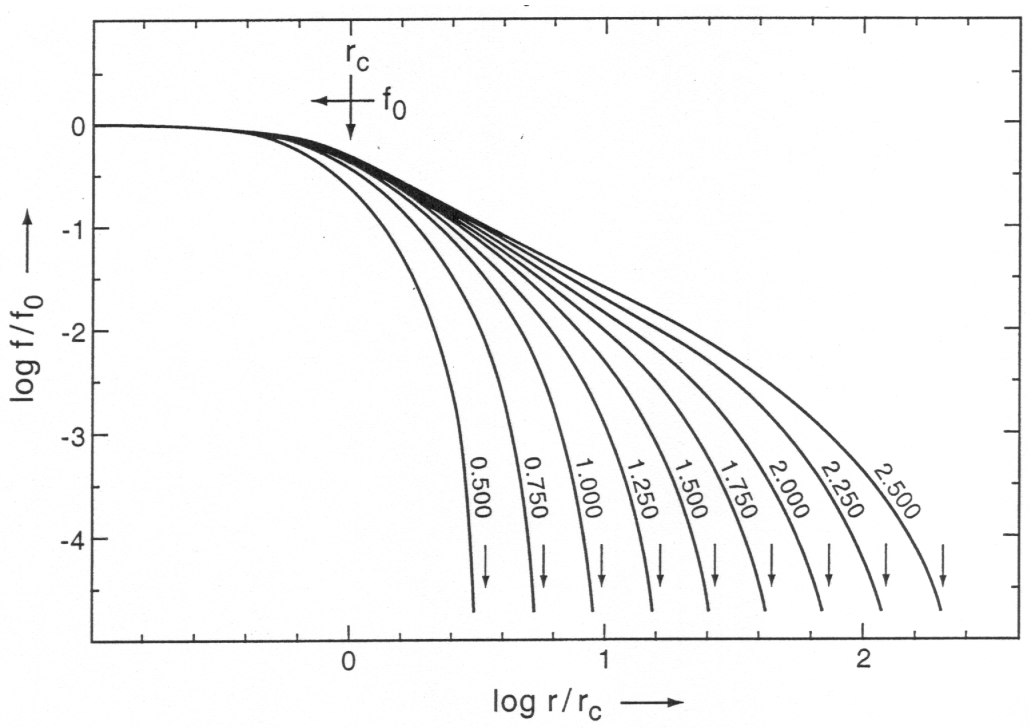

Figure 3.1: Surface density profiles as a function of the radius scaled to the core radius, r_c, for a family of dynamical King models. The number associated with each curve is a concentration parameter $c = \log(r_t/r_c)$ (Elson 1999; after King 1966).

4. The King model, also called "Lowered Maxwellian", provides an ideal combination of both theoretical construction and observed structure. It incorporates three essential dynamical processes: (i) dynamical equilibrium, (ii) the effect of gravitational encounters which tend to set up a Maxwellian distribution of velocities, and (iii) a cut–off in energy above which stars are deemed to have escaped from the cluster (Meylan & Heggie 1997). Unfortunately, the density cannot be given as a function of r but of the potential energy W (King 1966); ρ is constructed numerically from suitable boundary conditions (central density ρ_c, a special parameter for the central velocity dispersion σ^2, and the tidal radius r_t). The distribution function of energies is given by

$$f(\mathcal{E}) = \frac{\rho_c}{(2\pi\sigma^2)^{3/2}} \left(e^{-\mathcal{E}/\sigma^2} - e^{-\mathcal{E}_t/\sigma^2} \right), \tag{6}$$

where $\mathcal{E} = v^2/2 + \Phi(r)$ is the dimensionless energy per unit mass of a star, and $\mathcal{E}_t$ is the energy of a star that just reaches the edge of the cluster; stars of higher energy would escape entirely, so that $f(\mathcal{E} > \mathcal{E}_t) \equiv 0$ (Binney & Tremaine 1987). An example for a set of King models with different boundary conditions is shown in Figure 3.1.

Taking into account the velocity anisotropy expected in the halo, these models can be extended to King–Michie models (Michie 1963). Here, the velocity distribution is isotropic at the centre and nearly radial in the outer parts.

Other models have been designed to satisfy the Boltzmann equation, some of them including rotation or a multiple masses, however, the few mentioned above have achieved the greatest prominence in applications.

4 Evolutionary processes in star clusters

The internal evolution of a star cluster is governed by its tendency towards a Maxwellian velocity distribution. The small energy changes of each star during several encounters sum up on a relaxation time scale (Ch. 5.2), which tries to "smooth out" the energetic differences. Since a gravitating system is liable to an attractive force, the collapse of the central core makes up an important phase and probably the most fascinating aspect of the dynamical cluster evolution. There are three mechanisms acting in different ways in order to achieve the collapse: gravothermal instability, equipartition, and evaporation. In a real cluster of stars all of these processes occur simultaneously, but in the idealized models, which we construct, it is possible to isolate the specific processes and to gain some understanding in the particular effects.

4.1 Gravothermal instability

By analogy with the particles in an ideal gas, the kinetic energy K in a self–gravitating system of N equal point masses can be expressed by its mean temperature:

$$K = \frac{1}{2} N m \langle v^2 \rangle = \frac{3}{2} N k_{\mathrm{B}} \langle T \rangle, \tag{7}$$

where m is the stellar mass, k_{B} is Boltzmann's constant, and $\langle v^2 \rangle$ and $\langle T \rangle$ are the mean velocity dispersion and temperature, respectively, both usually depending on the position in the cluster. According to the virial theorem, $2K + W = 0$, the total energy is

$$E = K + W = -K = -\frac{3}{2} N k_{\mathrm{B}} \langle T \rangle. \tag{8}$$

Thus, the heat capacity c turns out to be negative:

$$c \equiv \frac{dE}{d\langle T \rangle} = -\frac{3}{2} N k_{\mathrm{B}}. \tag{9}$$

This result is valid for any bound, self–gravitating system, and it exhibits a quite unusual behaviour: The system becomes hotter as it loses energy and cools as it is heated. If such an apparently paradox system is in thermal contact with a heat sink at some constant temperature, a small instability would cause the heat flux going into the sink. This energy loss increases the kinetic energies of the remaining particles (heating), and the total binding energy W becomes even more negative. Consequently, the system contracts. The temperature difference between the bound system and the sink becomes larger and, again, the heat flux is intensified — a runaway process takes place. The central core of a cluster can be regarded as an isothermal system being in contact with an outer halo; the former is the heat source, the latter serves as the heat sink. Thus, it is possible for the core to lose energy, contract and heat up.

The situation is summarized in Fig. 4.1, where the total energy (vertical axis) is compared with the thermal energy (horizontal axis). At temperatures very much larger than the gravitational energy, a system of any particles behaves like an ideal gas with the total energy saved in the random kinetic motions (point A). If the temperature is reduced, the system moves down along the curve. At point B the energy passes through zero, and the gravitational attraction becomes significant. As the temperature is decreased further to point C, the system will be dominated by self–gravity and it becomes unstable between C and D for the reasons given above: Heat flows from the shrinking centre to the sink, and the temperatures of both the core and the halo rise. Beyond point D, *any* isothermal gas, even without a heat sink, would collapse and develop a core–halo–structure (Binney & Tremaine 1987).

The collapse of a star cluster is stopped by the formation of binaries in the very centre. With the density rising high, triple encounters are likely to take place. The orbital motions of temporary triple

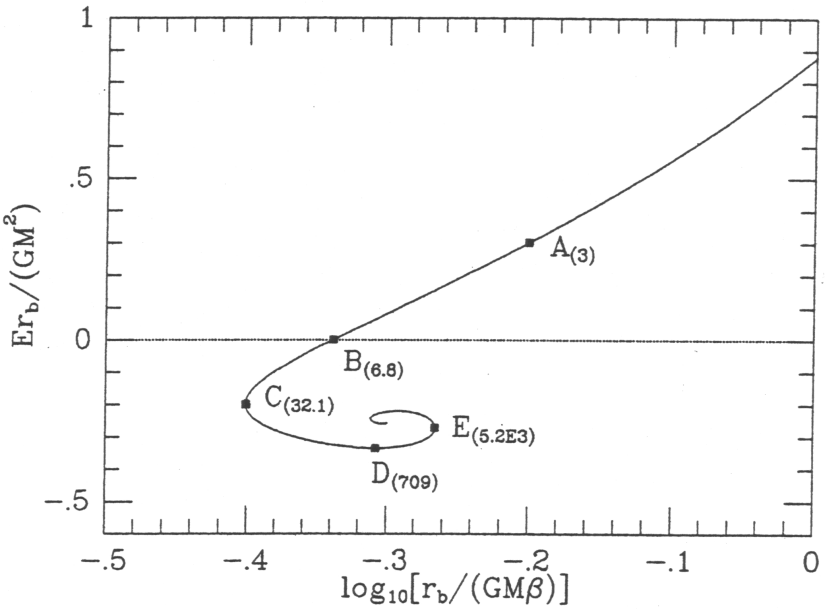

Figure 4.1: Relation between the total energy and temperature for an isothermal gas. The marked points are explained in the text, the subscripts in brackets denote the density contrast between the centre and the outermost layer, ρ_c/ρ_{r_b} (Binney & Tremaine 1987).

stars have a lot of chaotic aspects, for the particles exchange an enormous amount of energy while accelerating, decelerating and scattering. Numerical studies of the three–body problem reveal that a binary star is formed at the end of the interaction process, and one star receives a kinetic energy high enough to be pushed to larger distances, eventually escaping. Binaries will absorb more gravitational energy either by hardening during subsequent encounters or by breaking up in collisions with other stars, especially other binaries; then they transfer the binding energy to the other system. In any case, binaries open up a vast range of parameters (e.g. cross sections, masses, eccentricities) that will dominate the internal evolution of the cluster. The heat flux can indeed be brought to an end, and the collapse of the core is halted.

The consequences of all these interactions alter the dynamics and physics of the system as a whole. For example, they channel the formation of blue stragglers, mass transfer between the binary components, and X–ray sources. See Bailyn (1992) for more details on the astrophysical effects that arise in real star clusters.

4.2 Escaping stars

Stars, whose velocity exceed the local escape velocity, leave the cluster causing a slow but irreversible leakage. During each relaxation time an approximately constant fraction of stars is scattered to energies above that velocity. If they are removed, the escape energy also drops in proportion to the remaining mass. The energy required to remove a unit of mass, $\frac{1}{2}\langle v_{\rm esc}^2\rangle$, equals $-2W/M$, so we have

$$\langle v_{\rm esc}^2\rangle = -4W/M. \tag{10}$$

Recalling the virial theorem, $-W = 2K$, where $K = \frac{1}{2}M\langle v^2\rangle$ is the total kinetic energy, one finds that

$$\langle v_{\rm esc}^2\rangle = 4\langle v^2\rangle, \tag{11}$$

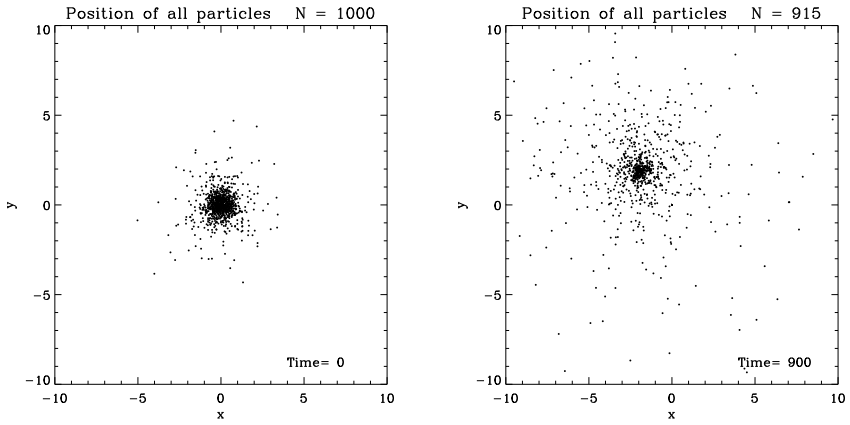

Figure 4.2: Illustration of the evaporation process due to escaping stars. This simulation started with 1000 particles in a Plummer sphere (*left*) and it has lost 85 of its stars after ≈ 50 relaxation times (*right*; Ch. 5.2).

i.e. the mean escape speed is just twice the velocity dispersion.

The escape can happen by two conceptionally different mechanisms: (a) A close encounter with another star can produce a velocity change with the speed exceeding the escape velocity — we shall call that process "ejection"; (b) a myriad of weak (i.e. more distant) encounters can continuously accumulate the kinetic energy of a star, until one single weak fly–by gives the star a slightly positive energy and it escapes — this effect is termed "evaporation". Evaporation is a more complicated process since it is much like a diffusion in energy space (Hénon 1969). An example from our simulations is shown in Figure 4.2, where the positions of the stars are projected onto the x–y–plane.

In tidally truncated clusters the escape rates are higher than in isolated clusters, and an introduction of a mass spectrum also leads to an enhanced mass loss (Wielen 1975). Evaporation heads for a complete disintegration of the cluster, where its final stage would be represented by a hard bound binary on a Kepler orbit that has "survived".

The escape of single stars causes a kind of core collapse: When a star leaves the cluster, it takes away some energy — kinetic as well as potential. In order to keep the virial equilibrium, the reduction of the total kinetic energy makes the potential W become more negative. The stars get stronger bound and the cluster contracts. The remaining stars need to find a new Maxwellian, but meanwhile develop a new "Maxwellian tail" with some other stars exceeding the escape velocity.

In addition, the tidal border of a host Galaxy reinforces the dissolution of the cluster: It shrinks because of losing its members *and* the tidal border moving inwards, stripping away the stars. Many factors concerning the environment (presence of a disk and passages through the galactic plane, bulge, molecular clouds etc.) shorten the time scale for evaporation. More details on the dissolution are given in Baumgardt (2001).

4.3 Equipartition

Additionally to the previous two effects, this mechanism occurs in multi–mass systems only. Stars of all masses try to balance out their energy differences: The heavy masses slow down, while the lighter ones gain kinetic energy. If the number of the heavy stars is sufficiently large, they will continue to give up their energy to the lighter stars without reaching equipartition and hence draw closer and closer. The subsystem of heavy masses contracts rapidly and leads to a core instability. The details are subject of the upcoming chapters.

5 Evolutionary time scales

In a system of many particles, an estimation of the time scales tells one about the physical processes that are likely to govern the particular dynamical state. The time scales are not independent but relate to overall changes of the spatial distribution, nevertheless, they provide a useful guide when viewed from an initial state.

5.1 Crossing time

The crossing time is an approximate time that a star with velocity v needs to traverse half of its orbit with radius r:

$$t_{\rm cr} = \frac{r}{v}. \tag{12}$$

A common convention is the choice of the size of a cluster R (more specifically, the virial radius, but the half–mass radius is also a good approximation) for the orbit and the velocity dispersion $\langle v^2 \rangle$ (Meylan & Heggie 1997).

The crossing time is approximately equal to the dynamical time, which expresses the motion of a harmonic oscillator in a gravitational potential,

$$t_{\rm dyn} = \frac{P}{4} = \frac{1}{4} \cdot \frac{2\pi r}{v_c},$$

with P being the orbital period, and v_c the circular velocity at distance r. Since the velocity depends on the local density, $v_c = \sqrt{4\pi G\rho/3} \cdot r$, we have

$$t_{\rm dyn} = \sqrt{\frac{3\pi}{16 G\rho}} \approx t_{\rm cr}. \tag{13}$$

Therefore, no matter what is the initial distance from the centre, a mass particle at rest will reach $r = 0$ in this time or a quarter of a "period" (Binney & Tremaine 1987).

5.2 Relaxation time

The most important time scale for the evolution of a globular cluster is the two–body relaxation time. It is the time after which a star's moving direction has been deflected by 90 degrees relative to its original direction: $\langle \Delta\Theta^2 \rangle^{1/2} \approx \frac{\pi}{2}$. This deflection has been accumulated due, not to a single close encounter, but to the cumulative effect of many distant encounters. These many mild encounters produce major changes in the structure of the cluster, without significantly disturbing its dynamical equilibrium. Equivalently, it is the time required for a star to suffer a velocity change comparable to its original velocity: $\langle \Delta v^2 \rangle \approx v^2$.

The relaxation time depends on the density and is therefore a function of the radius in the cluster. Although several precise definitions exist, among dynamicists widely accepted is the one by Spitzer (1987, eq. 2–62):

$$t_{\rm rx} = \frac{0.065 \langle v^2 \rangle^{3/2}}{G^2 \langle m \rangle \rho \ln(\gamma N)}. \tag{14}$$

Here, $\langle v^2 \rangle$ is the velocity dispersion of the stars, ρ the mass density, $\langle m \rangle$ the average stellar mass, G the Gravitational constant, and $\ln(\gamma N)$ the Coulomb logarithm with a value for γ favoured in this work to be about 0.11 (Giersz & Heggie 1994a). This will be matter of detailed discussion in Chapter 9.6.

In different regions of a star cluster, the relaxation time usually varies by several orders of magnitude. The inner regions will relax most quickly, while in the halo the time may be much longer than the age of the Universe. For rough estimates a useful global quantity is the *half–mass* relaxation time. It is obtained when the density ρ is replaced by the mean density inside the half–mass radius, and the velocity dispersion, which is also a local quantity, is obtained from the virial theorem. The result is

$$t_{\rm rh} = 0.138 \frac{M^{1/2} r_{\rm h}^{3/2}}{G^{1/2} \langle m \rangle \ln(\gamma N)} = 0.138 \frac{N r_{\rm h}^{3/2}}{(GM)^{1/2} \ln(\gamma N)}, \tag{15}$$

with M, $r_{\rm h}$ and N being the total mass, the half–mass radius and the total number of stars, respectively. The half–mass relaxation time has the advantage that it changes relatively little during the evolution.

When comparing the time scale of relaxation in eq. (15) with the crossing time at $r_{\rm h}$ in eq. (13), a fundamental proportionality turns out that is of high interest for internal dynamics:

$$\frac{t_{\rm rh}}{t_{\rm cr}} \propto \frac{N}{\ln(\gamma N)}. \tag{16}$$

5.3 Core collapse time

Two–body relaxation causes star clusters to redistribute the thermal energy among stars. Since this kind of heat transfer acts on the relaxation time scale, a core collapse is similarly ensued in gravitationally unstable systems. In general, the time of core collapse depends on the initial mass function (IMF), the initial density, and the degree of anisotropy. In addition, tidal shocking may accelerate the collapse, while mass loss due to escapers may delay it (Elson 1999).

The core collapse time is best studied numerically. For equal–mass models it ranges about 330 central relaxation times ($t_{\rm rx,core}$) or about 12—19 half–mass relaxation times, $t_{\rm rh}$. Quinlan (1996) gives a time scale of $15.7\,t_{\rm rh}$ for an isolated cluster, if an isotropic velocity distribution is assumed. Takahashi (1995) modelled Plummer spheres for an anisotropic case, and determined the collapse time to about $17.6\,t_{\rm rh}$. Other authors find similar factors (Fig. 5.1), and we shall adopt

$$t_{\rm cc} \approx 17.5\,t_{\rm rh}. \tag{17}$$

Though the values are used in most studies of the core collapse, they are a poor guide for real star clusters, e.g. globular clusters have central relaxation times that are typically ten, sometimes a hundred times shorter than their half–mass relaxation times (Quinlan 1996). So far, the core collapse time is only found empirically from a large number of numerical simulations, for there exists no analytical theory which would predict it a priori from cluster properties, e.g. the star number, IMF, or concentration parameters. One of the problems in its determination is the large statistical uncertainty, particularly when the number of stars involved in the collapse is small.

5.4 Equipartition time

When different masses are on work, two–body relaxation turns also into an equipartition process: The exchange of energies between light and heavy stars proceeds on the relaxation time scale, so the time at which equipartition will be achieved is of the same order of magnitude. The time scale was introduced by Spitzer (1969) as:

$$t_{\rm eq} = \frac{(\langle v_1^2 \rangle + \langle v_2^2 \rangle)^{3/2}}{8(6\pi)^{1/2} G^2 m_2 \rho_1 \ln(\gamma N)}. \tag{18}$$

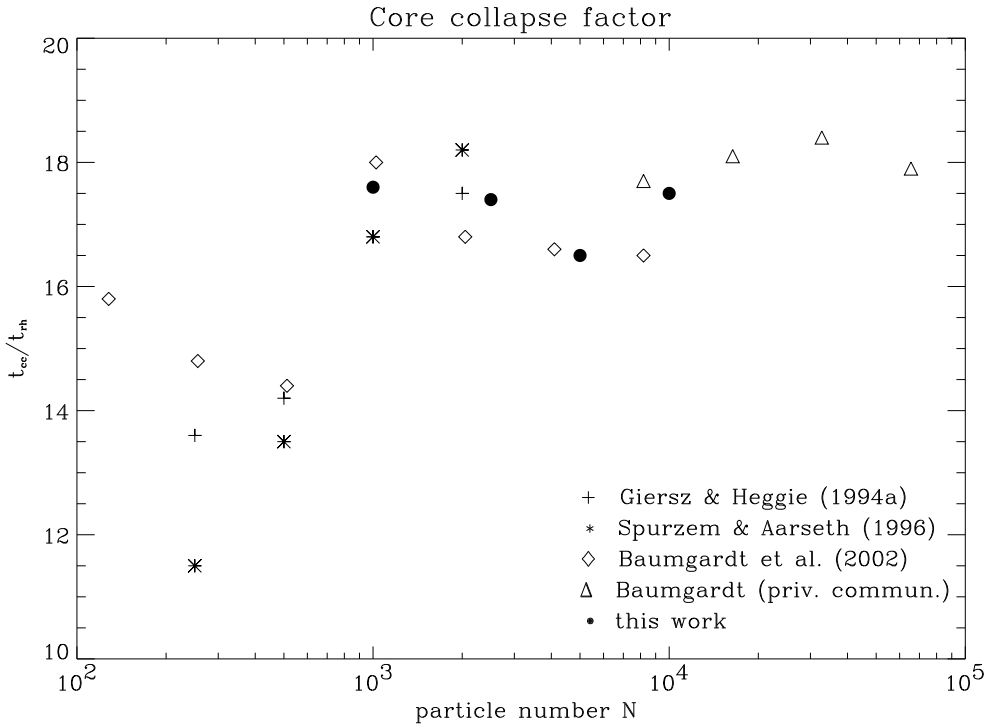

Figure 5.1: Factor of the relaxation time at which the core collapse occurs, as determined numerically by some authors. For small particle numbers the determination is rather unsure, but it depends also on assumptions made in the theory.

If the rms velocities of the two stellar types are equal, the ratio of $t_{\rm eq}/t_{\rm rx}$ is about proportional to m_1/m_2. In order to be able to establish equipartition, the system has to fulfill the stability criteria which are discussed in Chapter 6.

5.5 Evaporation time

Facing the differences between the ejection time and evaporation time (Ch. 4.2), the mean time for a star to be ejected in a three–body encounter is

$$t_{\rm ej} = 1.1 \cdot 10^3 \ln(\gamma N)\, t_{\rm rh}, \tag{19}$$

where the value is expressed in units of the half–mass relaxation time (Binney & Tremaine 1987). The rate by which the cluster loses its stars is then

$$\frac{dN}{dt} = -\frac{N}{t_{\rm ej}} = -8.8 \times 10^{-4} \frac{N}{t_{\rm rh} \ln(\gamma N)}. \tag{20}$$

The evaporation time and rate can analogously be estimated to

$$t_{\rm evap} \approx 100\, t_{\rm rh} \qquad \text{and} \qquad \frac{dN}{dt} = -3 \cdot 10^{-3} \frac{N}{t_{\rm rh}}, \tag{21}$$

respectively. For typical values of the Coulomb logarithm, $\ln(0.1N) \approx 10$, one finds that the ejection time is much longer than the evaporation time.

6 Theories on equipartition

In a particle system with several different masses, encounters between the objects tend to produce an equipartition of kinetic energy. The exchange of energies takes place via heat fluxes, and equipartition is achieved when the thermal gradients vanish. A self–gravitating system such as a cluster of stars also tends to a thermal equilibrium (equipartition) disregarded whether it is in dynamical equilibrium (virial) or not.

Equipartition is extremely important in constructing models of stellar clusters containing a realistic distribution of masses. We consider the case of a system with two masses for simplicity. In the following, the quantities of the lighter particles will be denoted by the subscript 1, and the heavier ones by 2:

m_1, m_2: light and heavy masses of the individual particles,
N_1, N_2: their total numbers,
M_1, M_2: total mass of the two components,
R_1, R_2: radii of spheres containing *half* of the indexed mass (close to virial radii),
ρ_1, ρ_2: mean densities inside a sphere with radius R_i,
$\langle v_1^2 \rangle, \langle v_2^2 \rangle$: velocity dispersions of the stars of mass 1 and 2, respectively.

The cluster as a whole consists of $N_1 + N_2 = N$ particles, and its total mass is $m_1 N_1 + m_2 N_2 = M_1 + M_2 = M_{\rm tot}$. The ratio of the individual masses is denoted by $\mu = m_2/m_1$, the total fraction of the heavy component by $q = M_2/M_{\rm tot}$.

6.1 The heuristical picture

During two–body encounters all stars exchange their energies and try to find a thermodynamic equilibrium. The main distinction between systems of equal and unequal masses concerns the question of equipartition, or, more generally, how the velocity dispersion differs from one particle population to another. Equipartition between the populations is obtained, when the kinetic energies of the individual particles are the same:

$$m_1 \langle v_1^2 \rangle = m_2 \langle v_2^2 \rangle. \tag{22}$$

Assuming an isotropic velocity distribution for all masses initially, the most massive stars have on average the largest kinetic energy at any point in the cluster, and in the course of encounters they lose it to the lighter ones and slow down. Attracted by the central potential, the heavies are accelerated towards the gravitational centre. This new gain of kinetic energy, they lose again in subsequent two–body interactions. Thus, the heavies become selectively concentrated in the inner parts and have lower random velocities on average. They also will not rise so far out against the gravitational potential of the cluster. On the other hand, the light stars speed up and their orbits expand; they remain most of their orbital time in the outer parts of the system. The star cluster appears like stratified by mass. Hence, mass segregation is an associated consequence of the equipartition process. The congregation of heavy masses in the inner regions has widely been observed throughout all kinds of stellar clusters (Bonnell & Davies 1998).

If the mass stratification proceeds far enough, then the self–gravity of the heavier stars will dominate the potential in the core. Their subsystem will undergo gravothermal collapse, while the light ones will not. In his pioneering paper on equipartition, Spitzer jr. (1969) predicted the conditions, for which the stability prevails. His main ideas and the impact on other works will be reiterated in the following sections.

6.2 Conditions for equipartition

We limit the discussion on two cases: On one hand, we assume that the mass fraction of the heavy component, q, is sufficiently small so that ρ_2 is everywhere negligible compared to ρ_1, and on the

other hand, vice versa, that q is sufficiently large and ρ_1 can be neglected. The former case is more important for the initial setup of actual clusters. But, where mass stratification increases ρ_2 in the central regions, we shall see that the latter case takes over the equalization process locally and causes the collapse of the subsystem of heavy stars.

As for the first case, the velocity dispersion of the heavy component can be derived from the virial theorem,

$$2K_2 + (W_2 + W_{1,2}) = 0, \tag{23}$$

where $K_2 = \frac{1}{2}M_2\langle v_2^2\rangle$ is the kinetic energy of the heavy stars, $W_2 = -fGM_2^2/R_2$ is the potential energy arising from the interactions of the heavy stars with themselves[1], and $W_{1,2}$ is the potential energy from the interactions of the heavy with the light stars. We will compute the latter term first. Since M_2 is assumed to be small, the contribution of the heavy stars to the total cluster potential will also be small, i.e. $\Phi_{\rm tot} \approx \Phi_1$. For the heavies, the potential Φ_1 caused by the light stars appears like an "external" potential, and we may write

$$W_{1,2} = \int \rho_2 \Phi_1 dV = \int_0^\infty \rho_2(r)\frac{-GM_1(r)}{r}4\pi r^2 dr. \tag{24}$$

We replace $M_1(r)$ by $4\pi\rho_1 R^3/3$, and set the density of the light stars to its constant central value, because the heavy system will not strongly perturb it, $\rho_1(r) \equiv \rho_{\rm c,1}$. We get

$$\begin{aligned} W_{1,2} &= -4\pi G\rho_{\rm c,1}\int_0^\infty \rho_2(r)\frac{4\pi}{3}r^4 dr \\ &= -4\pi G\rho_{\rm c,1}\cdot\frac{\langle R_2^2\rangle}{3}\int_0^\infty \rho_2(r)4\pi r^2 dr \\ &= -\frac{4\pi}{3}G\rho_{\rm c,1}\langle R_2^2\rangle M_2. \end{aligned} \tag{25}$$

Here, we approximated the integral of r^4 for one part by the mean squared value of r of the heavy stars using the theorem of the mean value integral and denoted this by $\langle R_2^2\rangle$, and the other part of the integral we solved for the sphere.

Putting now the three terms in eq. (23) together and solving for the velocity dispersion of the heavies, one finds:

$$\langle v_2^2\rangle = f\frac{GM_2}{R_2} + \frac{4\pi G}{3}\rho_{\rm c,1}\langle R_2^2\rangle. \tag{26}$$

An analogous virial (23) for the light component can be constructed: $2K_1 + (W_1 + W_{2,1}) = 0$. The corresponding term of componentwise interaction, $W_{2,1}$, is negligible, provided that M_2 (and consequently Φ_2) is small and has no significant effect on the velocity dispersion of the light stars. We get

$$\langle v_1^2\rangle = f\frac{GM_1}{R_1}. \tag{27}$$

When substituting the velocity dispersions (26) and (27) in the equation for equipartition (22), it reads:

$$\frac{m_1 M_1}{R_1} = m_2\left(\frac{M_2}{R_2} + \frac{4\pi}{3f}\rho_{\rm c,1}\langle R_2^2\rangle\right). \tag{28}$$

[1] f is a dimensionless constant between 0.44 and 0.38 for polytropes of index n between 2 and 5, respectively. The value of 0.4 adopted by Spitzer (1969, 1987) should be a reasonable approximation for most systems.

Some lengthy but straightforward reorganization of these terms lead to the stability condition found by Spitzer (1969). Using the definitions $\frac{1}{2}M_2 = \frac{4\pi}{3}R_2^3\rho_2$ and $(R_1/R_2)^3 = (M_1/M_2)(\rho_2/\rho_1)$, one finally obtains:

$$\frac{M_2}{M_1}\left(\frac{m_2}{m_1}\right)^{3/2} = \frac{(\rho_1/\rho_2)^{1/2}}{\left(1+\frac{1}{2f}\frac{\rho_{c,1}}{\rho_1}\frac{\langle R_2^2\rangle}{R_2^2}\frac{\rho_1}{\rho_2}\right)^{3/2}}. \tag{29}$$

We define the left hand side as χ and express the ratios M_2/M_1 and m_2/m_1 in terms of q and μ defined at the beginning of this chapter:

$$\chi \equiv \left(\frac{q}{1-q}\right)\mu^{3/2} = \frac{(\rho_1/\rho_2)^{1/2}}{(1+\alpha\rho_1/\rho_2)^{3/2}} < \chi_{\max}. \tag{30}$$

The function $\chi = \chi(q,\mu)$ depends on the density ratio of the two subsystems and has got a maximum value $\chi_{\max}$, which is determined below. The quantity $\alpha = \frac{1}{2f}\frac{\rho_{c,1}}{\rho_1}\frac{\langle R_2^2\rangle}{R_2^2}$ introduced can be considered as a constant of value 5.6 for the following reasons: The root mean square radius, $\langle R_2\rangle$, equals 1.13 R_2 in a parabolic potential well. This results from a constant $\rho_{c,1}$ in the core, and a Maxwellian velocity distribution of the heavy stars (Spitzer 1987). The ratio $\rho_{c,1}/\rho_1$ represents a density contrast between the centre and a confining layer close to the half–mass radius. Though widely variable, it is a criterion for the gravothermal stability of the system. If this ratio does not exceed unity much, the self–gravitational attraction will be a relatively small effect and the system remains stable; only for large values the self–attraction of the core outweighs the pressure of the surrounding shells, and the cluster becomes thermally unstable. The critical ratio, at which it becomes unstable, is about 709 for the isothermal sphere (Fig. 4.1), but for polytropes with n between 3 and 5, its value increases rather moderately from 2.5 to 4.4 (Spitzer 1987). We shall set here $\rho_{c,1}/\rho_1$ equal to 3.5 (Spitzer 1969). So, the constant α can be computed to 5.6, and it appears to be insensitive to the detailed density distribution.

Thus, the condition for equipartition (30) depends only on the density ratio between the two particle species, ρ_1/ρ_2. The function $\chi = \chi(\frac{\rho_1}{\rho_2})$ has got a maximum at the point $\rho_1/\rho_2 = 1/(2\alpha)$. With 5.6 assumed for α, the function's maximum value is

$$\chi_{\max} = 0.38\alpha^{-1/2} \approx 0.16. \tag{31}$$

The physical meaning of the maximum is that equipartition will only be possible, if the left hand side of (29) does not exceed this critical value. In case of $\chi > \chi_{\max}$, the condition is not fulfilled, inferring that the heavy stars cannot find an appropriate equilibrium with the light stars; either their total mass fraction q is too large to validate our assumption of a negligible ρ_2, or the ratio of the particle masses μ, indeed. This boundary condition is drawn as a dotted line in the q–μ–plane of Fig. 8.1.

It becomes obvious that the equipartition–based collapse is a somewhat self–limiting phenomenon. Also, when the heavy stars far outnumber the light ones (this is likely to happen in the central core during the process of mass segregation), the relative number of the lighter stars is inadequate to carry the energy rapidly away from the core. The heavies will continue sinking towards the centre, increase their kinetic energy and thus increase the departure from equipartition. They make up a subsystem, which rather collapses due to the own gravothermal instability than to the equipartition instability. In this sense, simultaneous thermal and dynamical equilibrium is impossible.

6.3 Multiple equipartition solutions

Another theory for the evolution of a two–component star cluster was developed by Lightman & Fall (1978). Their approach differs to Spitzer's in that sense that they use a homogeneous sphere instead

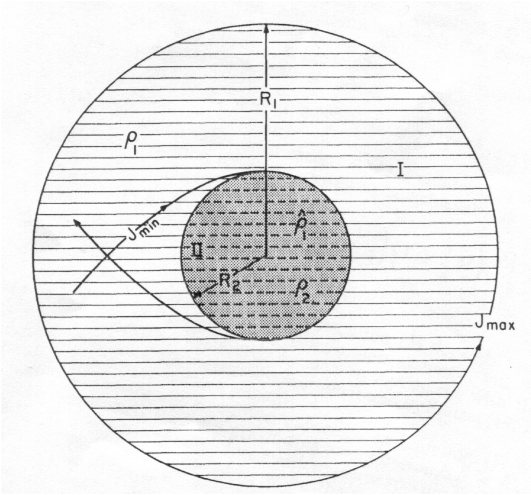

Figure 6.1: The two spatially distinct core regions of the light and heavy stars. The heavy particles are located with constant density ρ_2 in region II, $R \leq R_2$ (shaded); the light ones populate both regions, each with different densities, ρ_1 and $\hat{\rho}_1$. At a later evolutionary stage, some heavy particles of region II will evaporate into I. After Lightman & Fall (1978).

of a polytrope. They distinguish two separate regions for the light and heavy stars with radii R_1 and R_2, respectively. Exactly, these regions are the associated with the sizes of the homogenous spheres, but one can also identify them with the core radii of the two subsystems (Fig. 6.1). The constant f, which Spitzer introduces for polytropes (see footnote on page 16), turns out to be 3/5. From separate virial relations for each mass group, the velocity dispersions can be derived:

$$\begin{aligned} \langle v_1^2 \rangle &= \frac{3}{5}\frac{GM_1}{R_1} + \frac{3}{2}\frac{GM_2}{R_1} - \frac{9}{10}\frac{GM_2R_2^2}{R_1^3} \\ \langle v_2^2 \rangle &= \frac{3}{5}\frac{GM_2}{R_2} + \frac{3}{5}\frac{GM_1R_2^2}{R_1^3} \end{aligned} \tag{32}$$

Putting the dispersions into the requirement for thermal equipartition, eq. (22), one obtains

$$-\left(\frac{R_2}{R_1}\right)^3 \left(\frac{m_2}{m_1} + \frac{3}{2}\frac{M_2}{M_1}\right) + \frac{R_2}{R_1}\left(1 + \frac{5}{2}\frac{M_2}{M_1}\right) - \frac{m_2}{m_1}\frac{M_2}{M_1} = 0\,. \tag{33}$$

This is a cubic equation for the ratio of the two radii R_2/R_1. As such, it may have maximally three solutions. As the authors point out, the interesting result is that there may be two different equilibrium configurations for a given system. Physically it is understood from the fact that the heavy masses may achieve *either* a hydrostatic equilibrium in the whole system as given by the virial theorem, *or* a thermal equilibrium with the light masses in the core, depending on which of the two terms in the equations (32) dominates.

Avoiding complex solutions, the cubic function has got a maximum value at point

$$\left(\frac{R_2}{R_1}\right)_{\rm crit} = \left(1 + \frac{5}{2}\frac{M_2}{M_1}\right)^{1/2} \left(3\frac{m_2}{m_1} + \frac{9}{2}\frac{M_2}{M_1}\right)^{-1/2}\,. \tag{34}$$

When inserting that into eq. (33), one finds the value of the maximum; in analogy to Spitzer's theory, eq. (29) and (30), it is the border condition under which equipartition will be possible for the case of

the isothermal sphere:

$$\frac{M_2}{M_1}\left(\frac{m_2}{m_1}\right)^{\frac{3}{2}}\left[\left(1+\frac{3}{2}\frac{m_1}{m_2}\frac{M_2}{M_1}\right)\left(1+\frac{5}{2}\frac{M_2}{M_1}\right)^{-3}\right]^{\frac{1}{2}} \leq \left(\frac{4}{27}\right)^{\frac{1}{2}} . \tag{35}$$

In the notation of q and μ, it is

$$\left(\frac{q}{1-q}\right)\mu^{\frac{3}{2}}\left[\left(1+\frac{3}{2}\frac{1}{\mu}\frac{q}{1-q}\right)\left(1+\frac{5}{2}\frac{q}{1-q}\right)^{-3}\right]^{\frac{1}{2}} \leq 0.38\,, \tag{36}$$

or after further simplifying

$$q\mu^3\left[\left(1+\frac{3}{2\mu}q-q\right)\left(1+\frac{3}{2}q\right)^{-3}\right]^{\frac{1}{2}} \leq 0.38\,. \tag{37}$$

As visible from eq. (36), the functional term is in agreement with Spitzer's condition, but the term in brackets depends upon the particular density distribution. According to Lightman & Fall's theory, equations (35) to (37) describe the criterion for simultaneous dynamical and thermal equilibrium; if it is satisfied, the system will be stable. Moreover, a *thermally* unstable configuration arises when the ratio of the two region sizes, R_2/R_1, is less than the critical value in eq. (34); then, the self–gravity of the heavy subsystem will dominate and collapse under its gravothermal instability. Otherwise, a thermally stable configuration appears, when R_2/R_1 exceeds that critical value, meaning that the heavy subsystem is a "non–self–gravitating" one; then, the light stars can find an equipartition with the heavies. The condition border, eq. (37), is drawn as a dot–dashed line in Fig. 8.1.

6.4 Other theories

A theory very similar to Spitzer's has been derived by Inagaki & Wiyanto (1984). They actually combine both previous theories: While Spitzer incorporates the total masses of the two components when calculating the velocity dispersions, the latter consider just the situation in the core. The equations look virtually the same as eqs. (26) and (27), but they require the additional index c for the core:

$$\langle v_1^2\rangle = 0.4\frac{GM_{\mathrm{c},1}}{r_{\mathrm{c},1}} \qquad \text{and} \qquad \langle v_2^2\rangle = 0.4\frac{GM_{\mathrm{c},2}}{r_{\mathrm{c},2}} + \frac{GM_{\mathrm{c},1}\,r_{\mathrm{c},2}^2}{r_{\mathrm{c},1}^3} \tag{38}$$

During the process of equipartition in the early stages of the evolution, the quantities $M_{\mathrm{c},1}$, $r_{\mathrm{c},1}$, and $M_{\mathrm{c},2}$ are nearly constant, but $r_{\mathrm{c},2}$ shrinks. $\langle v_2^2\rangle$ will also have a minimum that can be found from the derivation of the second equation in (38):

$$\begin{aligned} \frac{d\langle v_1^2\rangle}{dr_{\mathrm{c},2}} &= -0.4\frac{GM_{\mathrm{c},2}}{r_{\mathrm{c},2}^2} + 2\frac{GM_{\mathrm{c},1}\,r_{\mathrm{c},2}}{r_{\mathrm{c},1}^3} = 0 \\ \Longrightarrow \qquad r_{\mathrm{c},2} &= 0.2^{1/3}(M_{\mathrm{c},2}/M_{\mathrm{c},1})^{1/3}\,r_{\mathrm{c},1}. \end{aligned}$$

Thus, when the core radius of the heavies, $r_{\mathrm{c},2}$, shrinks to that value, the minimum velocity dispersion of the heavy stars is attained; we have

$$\langle v_2^2\rangle_{\min} = 1.026\frac{GM_{\mathrm{c},2}^{2/3}\,M_{\mathrm{c},1}^{1/3}}{r_{\mathrm{c},1}}. \tag{39}$$

Equipartition is achieved when $m_2\langle v_2^2\rangle_{\rm min} = m_1\langle v_1^2\rangle$, or

$$\left(\frac{M_{\rm c,2}}{M_{\rm c,1}}\right)\left(\frac{m_2}{m_1}\right)^{3/2} \leq 0.4^{3/2} = 0.25\,. \tag{40}$$

This condition just differs from the one by Spitzer, eq. (29), in the upper border which we called $\chi_{\rm max}$. The line runs parallel to Spitzer's but shifted slightly upwards (the dot–dot–dot–dashed line in Figure 8.1). — In fact, Inagaki & Wiyanto did not explicitly point to the formula, eq. (40), but obtained an equation for the temperature *difference* between the two mass–components.

Another analysis of models in thermal and dynamical equilibrium was provided by Watters *et al.* (2000). Without deriving an analytical theory as in the foregoing theories, they performed Monte Carlo simulations with two mass bins in a certain parameter range, q and μ, to check for equipartition of energies. They made a fit to their results and acquired an empirical formula that renders more precisely the border between the stable and unstable regime:

$$\left(\frac{M_2}{M_1}\right)\left(\frac{m_2}{m_1}\right)^{2.4} \leq 0.32\,. \tag{41}$$

The boundary is strictly valid for $1.75 < \mu < 7$. For smaller μ, equipartition was always achieved in their simulations. The function is plotted as a dashed line in Fig. 8.1.

7 Simulation tools: NBODY6++

Numerical simulations give us a powerful tool to examine the basic processes of stellar dynamics and check the hypotheses on mass stratification presented in the previous chapter. But, however, the numerical simulation of a simple cluster containing some hundred thousand or even a million members still places heavy demands on the available tools. A balance has to be found between two constraints: On one hand the *realism*, i.e. the input of profound physics, inclusion of all the physical effects mentioned above, and also the maintenance of the accuracy of calculations; and on the other hand, the *efficiency*, i.e. the limitations given by the computational effort and suitable codes to be finished in a reasonable time. Many different kinds of approaches have been undertaken to suffice both:

- codes based on the direct force integration (Aarseth 1985 and 1999b),
- statistical models, which themselves divide into several subgroups (Fokker–Planck approximation by Cohn 1980; Monte–Carlo method by Hénon 1971; Gas models by Spurzem 1994),
- usage of high-performance parallel computers (Spurzem 1999),
- or the construction of special hardware devoted for these purposes (Makino *et al.* 1997).

All the aspects have their advantages as well as disadvantages. The most promising way to follow accurately the evolution of star clusters is based on the direct method of integrating the Newtonian equation of motion. The design of an efficient algorithm for this has peaked in the NBODY6–code by Aarseth (1999a), so far, which has been extended to its latest version, NBODY6++, suitable for parallel computers (Spurzem 1999). The basic features of the code increasing the efficiency may be considered under four separate headings: Prediction–correction method (Hermite scheme), individual and block time–steps, regularization of close encounters, and a neighbour scheme (Ahmad–Cohen scheme). We describe briefly these ideas, while a detailed description can be found in Aarseth (1993).

7.1 The Hermite integration method

Each particle is completely specified by its mass m, position $\mathbf{r}_0$, and velocity $\mathbf{v}_0$, where the subscript 0 denotes an initial value at a time t_0. The equation of motion for a particle i is given by its momentary acceleration $\mathbf{a}_{0,i}$ due to all other particles and its time derivative $\dot{\mathbf{a}}_{0,i}$ as

$$\mathbf{a}_{0,i} = -\sum_{i \neq j} G m_j \frac{\mathbf{R}}{R^3}, \tag{42}$$

$$\dot{\mathbf{a}}_{0,i} = -\sum_{i \neq j} G m_j \left[\frac{\mathbf{V}}{R^3} + \frac{3\mathbf{R}(\mathbf{V}\cdot\mathbf{R})}{R^5} \right], \tag{43}$$

where G is the gravitational constant; $\mathbf{R} = \mathbf{r}_{0,i} - \mathbf{r}_{0,j}$ is the relative coordinate; $R = |\mathbf{r}_{0,i} - \mathbf{r}_{0,j}|$ the modulus; and $\mathbf{V} = \mathbf{v}_{0,i} - \mathbf{v}_{0,j}$ the relative space velocity to the particle j. The NBODY6++ code follows the trajectory of the particle by firstly "predicting" a new position and new velocity for the next time step t. A Taylor series for $\mathbf{r}_i(t)$ and $\mathbf{v}_i(t)$ is formed:

$$\mathbf{r}_{p,i}(t) = \mathbf{r}_0 + \mathbf{v}_0(t-t_0) + \mathbf{a}_{0,i}\frac{(t-t_0)^2}{2} + \dot{\mathbf{a}}_{0,i}\frac{(t-t_0)^3}{6}, \tag{44}$$

$$\mathbf{v}_{p,i}(t) = \mathbf{v}_0 + \mathbf{a}_{0,i}(t-t_0) + \dot{\mathbf{a}}_{0,i}\frac{(t-t_0)^2}{2}. \tag{45}$$

The direct values of $\mathbf{r}_p$ and $\mathbf{v}_p$, which result from this simple force calculation, do not fulfill the requirements for an accurate high–order integrator; they give just a clue to the "real" $\mathbf{r}_1$ and $\mathbf{v}_1$ at

the upcoming time t_1. Even if the time step, $t_1 - t_0$, is chosen impracticably small, a considerable error will quickly occur, let alone the inadequate computational effort. Therefore, an improvement is made by the Hermite interpolation which approximates the higher accelerating terms by an own Taylor series:

$$\mathbf{a}_i(t) = \mathbf{a}_{0,i} + \dot{\mathbf{a}}_{0,i} \cdot (t - t_0) + \frac{1}{2}\mathbf{a}^{(2)}_{0,i} \cdot (t - t_0)^2 + \frac{1}{6}\mathbf{a}^{(3)}_{0,i} \cdot (t - t_0)^3, \quad (46)$$

$$\dot{\mathbf{a}}_i(t) = \dot{\mathbf{a}}_{0,i} + \mathbf{a}^{(2)}_{0,i} \cdot (t - t_0) + \frac{1}{2}\mathbf{a}^{(3)}_{0,i} \cdot (t - t_0). \quad (47)$$

Here, the values of $\mathbf{a}_{0,i}$ and $\dot{\mathbf{a}}_{0,i}$ are already known, but a further derivation of equation (43) for the two missing orders on the right hand side turns out to be quite cumbersome. Instead, one determines the additional acceleration terms from the predicted ("provisional") $\mathbf{r}_p$ and $\mathbf{v}_p$; we calculate their acceleration and time derivative according to the equations (42) and (43) anew and call these new terms $\mathbf{a}_{p,i}$ and $\dot{\mathbf{a}}_{p,i}$, respectively. Because these values ought to be generated by the former high–order terms also (which we avoided), we put them into the left–hand sides of (46) and (47). Solving equation (47) for $\mathbf{a}^{(2)}_{0,i}$, then substituting it into (46) and simplifying yields the third derivative:

$$\mathbf{a}^{(3)}_{0,i} = 12\frac{\mathbf{a}_{0,i} - \mathbf{a}_{p,i}}{(t - t_0)^3} + 6\frac{\dot{\mathbf{a}}_{0,i} + \dot{\mathbf{a}}_{p,i}}{(t - t_0)^2}. \quad (48)$$

Similarly, substituting (48) into (46) gives the second derivative:

$$\mathbf{a}^{(2)}_{0,i} = -6\frac{\mathbf{a}_{0,i} - \mathbf{a}_{p,i}}{(t - t_0)^2} - 2\frac{2\dot{\mathbf{a}}_{0,i} + \dot{\mathbf{a}}_{p,i}}{t - t_0}. \quad (49)$$

Note, that the desired high–order accelerations are found just from the combination of the low–order terms for $\mathbf{r}_0$ and $\mathbf{r}_p$. We never derived higher than the first derivative, but achieved the higher orders easily through (42) and (43). This is called the Hermite scheme. The accuracy of the integrator is virtually the same as in the case of an explicit high–order derivation (Makino & Hut 1988).

Finally, we extend the Taylor series for $\mathbf{r}_i(t)$ and $\mathbf{v}_i(t)$, eqs. (44) and (45), by two more orders, and find the "corrected" position $\mathbf{r}_{1,i}$ and velocity $\mathbf{v}_{1,i}$ of the particle i at the computation time t_1 as

$$\mathbf{r}_{1,i}(t) = \mathbf{r}_{p,i}(t) + \mathbf{a}^{(2)}_{0,i}\frac{(t - t_0)^4}{24} + \mathbf{a}^{(3)}_{0,i}\frac{(t - t_0)^5}{120}, \quad (50)$$

$$\mathbf{v}_{1,i}(t) = \mathbf{v}_{p,i}(t) + \mathbf{a}^{(2)}_{0,i}\frac{(t - t_0)^3}{6} + \mathbf{a}^{(3)}_{0,i}\frac{(t - t_0)^4}{24}. \quad (51)$$

The integration cycle for other upcoming steps may now be repeated from the beginning, eqs. (42) and (43). The error in $\mathbf{r}$ and $\mathbf{v}$ within the two time steps $\Delta t = t_1 - t_0$ is expected to be proportional to Δt^4 (Makino 1991).

7.2 Individual and block time steps

Stellar systems are characterized by a fair range of densities which gives rise to different time scales of the orbital parameters. In the classical picture, the two closest bodies would determine the time–step of force calculation for the whole rest of the system. However, bodies in regions where the variation in force is relatively small, a permanent re–computing of the force terms is time consuming, so, in order to economize the calculation, these objects shall be allowed to move a longer distance before a recomputation becomes necessary. This is the idea of a vital method for assigning different time–steps, $\Delta t = t_1 - t_0$, between the force computations, the so–called "individual time–step scheme" (Aarseth 1963).

Each particle is assigned its own Δt_i which is first illustrated for the case of "block time–steps" in Figure 7.1. The particle named i has the smallest time step at the beginning, so its phase space

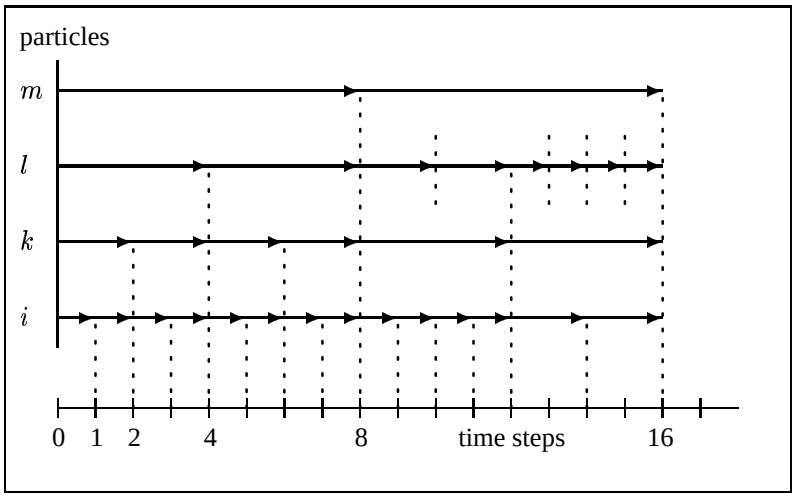

Figure 7.1: Block time steps exemplary for four particles.

coordinates are determined at each time step. The time step of k is twice as large as i's, and its coordinates are just extrapolated ("predicted") at the odd time steps, while a full force calculation is due at the dotted times. The step width may be altered or not after the end of the integration cycle for the special particle, as demonstrated for k and l beyond the label "8". The time steps have to stay commensurable with both, each other as well as the total time, such that a hierarchy is guaranteed. This is the block step scheme.

As a first estimate, the rate of change of the acceleration seems to be a reasonable quantity for the choice of the time step: $\Delta t_i \propto \sqrt{\mathbf{a}_i/\dot{\mathbf{a}}_i}$. But it turns out that for special situations in a many-body system, it provides some undesired numerical errors. After some experimentation, the following formula was adopted (Aarseth 1985):

$$\Delta t_i = \sqrt{\eta \frac{|\mathbf{a}_{1,i}||\mathbf{a}^{(2)}_{1,i}| + |\dot{\mathbf{a}}_{1,i}|^2}{|\dot{\mathbf{a}}_{1,i}||\mathbf{a}^{(3)}_{1,i}| + |\mathbf{a}^{(2)}_{1,i}|^2}}, \tag{52}$$

where η is a dimensionless accuracy parameter which controls the error. In most applications it is taken to be $\eta \approx 0.02$ to 0.04, see also next section.

For the block–time steps, the synchronization is made by taking the next–lowest integer of Δt_i; the time steps are quantized to powers of 2 (Makino 1991). Then, there will be a group (block) of several particles which are due to movement at each time step. If one keeps the exact Δt_i's evaluated from (52) for each particle, the commensurability is destroyed, and we arrive at the so–called "individual time steps"; in this case, there exists one sole particle being due. The latter concept is realized in the code NBODY4, where a neighbour scheme is renounced (see next section).

In the running code, the time–steps are adjusted to their appropriate values fairly quick. Although successive steps normally change smoothly, it is prudent to restrict the growth by a stability factor of 1.2.

7.3 The Ahmad–Cohen scheme

The computation of the full force for each particle in the system makes simulations very time–consuming for large memberships. Therefore, it is desirable to construct a method in order to speed up the calculations while retaining the collisional approach. One way to achieve this is to employ a "neighbour scheme", suggested by Ahmad & Cohen (1973).

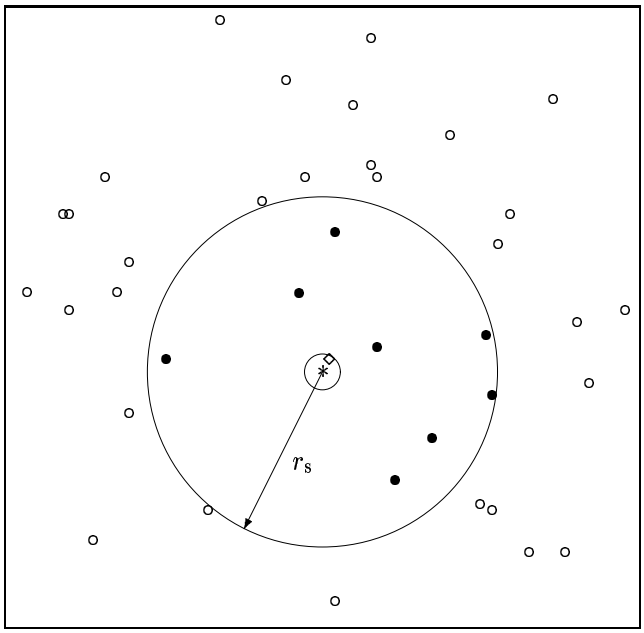

Figure 7.2: Illustration of the neighbour scheme for particle i marked as the asterisk (after Aarseth 1985).

The basic idea is to split the force polynomial on a given particle i into two parts, an irregular and a regular component:

$$\mathbf{a}_i = \mathbf{a}_{i,\mathrm{irr}} + \mathbf{a}_{i,\mathrm{reg}}. \tag{53}$$

The irregular acceleration $\mathbf{a}_{i,\mathrm{irr}}$ results from particles in a certain neighbourhood of i. They give rise to a stronger fluctuating gravitational force, so it is determined more frequently than the regular one of the more distant particles that do not change their relative distance to i so quickly. We can replace the full summation in eq. (42) by a sum over the N_{nb} nearest particles for $\mathbf{a}_{i,\mathrm{irr}}$ and add a distant contribution from all the other. Whether a particle is a neighbour or not is determined by its distance; all members inside a specified sphere ("neighbour sphere" with radius r_{s}) are held in a list, which is modified at the end of each "regular time–step" when a total force summation is carried out. In addition, approaching particles within a surrounding shell satisfying $\mathbf{R} \cdot \mathbf{V} < 0$ are included. This "buffer zone" serves to identify fast approaching particles before they penetrate too far inside the neighbour sphere.

Figures 7.2 and 7.3 show how the Ahmad–Cohen scheme works for one particle (Makino & Aarseth 1992). At the beginning of the force calculation, a list of neighbour objects around the particle i is created first (filled dots). From this neighbour list the irregular component $\mathbf{a}_{i,\mathrm{irr}}$ is calculated, and then the summation is continued to the distant particles obtaining $\mathbf{a}_{i,\mathrm{reg}}$. At the same time we also calculate the first time derivative. From the equations (46) and (47) the position and velocity of the particle i are predicted. At time $t_{1,\mathrm{irr}}$ we apply the "corrector" only for $\mathbf{a}_{i,\mathrm{irr}}$ from the neighbours; the regular component we do not correct but obtain by extrapolating $\mathbf{a}_{i,\mathrm{reg}}$. At the next step, $t_{2,\mathrm{irr}}$, the same predictor–corrector method proceeds for the neighbour particles, while the correction of the distant acceleration term is still neglected. When t_1 is reached, the total force is calculated on the basis of the full application of the Hermite predictor–corrector method. Also, a new neighbour list is constructed using the positions at time t_1.

For a neighbour list of size $N_{\mathrm{nb}} \ll N$, this procedure can lead to a significant gain in efficiency, provided the respective time scales for $\mathbf{a}_{i,\mathrm{irr}}$ and $\mathbf{a}_{i,\mathrm{reg}}$ are well separated. The actual size is controlled by choosing an appropriate radius for the neighbour sphere, r_{s}. Practically, this is controlled by

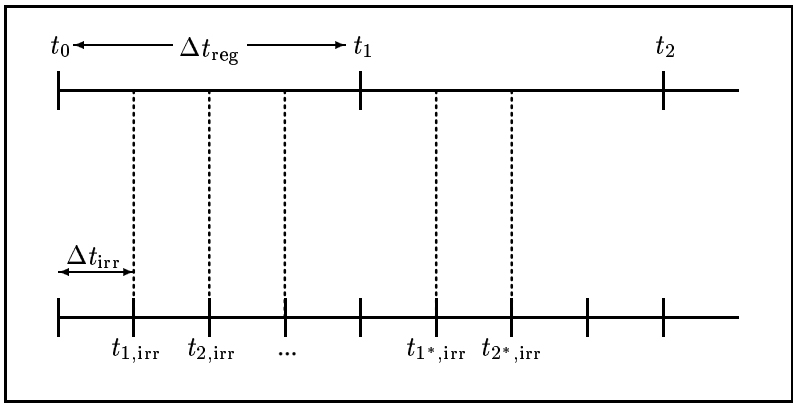

Figure 7.3: Regular and irregular time steps (after Makino & Aarseth 1992).

some kind of "contrast of the local density" (Aarseth 1985):

$$\frac{N_{\rm nb}}{N/2}\left(\frac{r_{\rm h}}{r_{\rm s}}\right)^3 \approx \frac{n_{\rm nb}}{n_{\rm h}}, \tag{54}$$

where N is the total particle number; $r_{\rm h}$ and $r_{\rm s}$ are the half–mass radius and the radius of the neighbour sphere; and $n_{\rm nb}$ and $n_{\rm h}$ are the particle densities inside the neighbour sphere and inside the half–mass radius, respectively. The approximation in the equation is due to the fact, that one–half of the total particle number is not necessarily the half of the total mass, to which $r_{\rm h}$ is related.

The method of the two particle groups is squeezed into the hierarchical time–step scheme making the overall view quite complex. Each particle is moved due to its time–step order *and* the time–steps, because the force calculation is divided: In eq. (52) a further subscript is needed which distinguishes the regular and irregular time step. The accuracy can be tuned by $\eta_{\rm irr} \approx 0.02$ and $\eta_{\rm reg} \approx 0.04$, again.

Both, the neighbour scheme and the hierarchical time–step scheme have in common that they are centered on one particle i, and they distinguish between nearby and remote stars, and they save computational time. One may ask: What is the intriguing difference between them? — The neighbour scheme is a *spatial* hierarchy, which avoids a frequent force calculation of the remote particles, because their totality provides a smooth potential which does not vary so much with respect to the particle i; that potential is rather superposed by some fluctuating peaks of close–by stars which will be "worked in" by the more often force determination. The time step scheme, in contrast, exhibits the *temporal* behaviour of the intervals for re–calculation of the full force in order to maintain the exactness of the trajectory; time steps chosen too small slow down the advancing calculation losing the computer's efficiency.

7.4 KS–Regularization

The fourth main feature of the Nbody6–code is the treatment of close encounters. This is to happen in the cluster centre when two (or even more) stars come very close together in an hyperbolic encounter or upon the presence of binaries. As their relative distances become small ($R \to 0$), strong singularities would occur according to equations (42) and (43). The "regularization" is an elegant trick in order to deal with such particles which are as close as the diamond in the Figure 7.2.

The idea is to take both stars out of the main integration cycle, replace them by their centre of mass and advance the usual integration with this composite particle instead of resolving the two components. The orbit of the pair will be determined by switching to a different (regularized) coordinate system. This transformation involves a set of four regular spatial coordinates and a fictious time. A 4×4 matrix transforms the space and velocity into a form resembling a harmonic oscillator. The

equations of motion become regular then. The method itself goes back to Kustaanheimo & Stiefel (1965) and makes an accurate calculation of a perturbed two–body motion possible. The time–step of such a "KS–regularized pair" is independent of the eccentricity and the KS–period can involve several Kepler orbits in case of a physical binary.

Close encounters between single particles and binary stars are also a central feature of cluster dynamics. Such temporary triple systems often reveal irregular motions, ranging from just a perturbed encounter to a very complex interaction, in which disruption of binaries, exchange of components and ejection of one star may occur. Although not analytically solvable, the general three–body problem has received much attention. The KS–regularisation was expanded to the isolated 3– and 4–body problem, and later on to the perturbed 3–, 4–, and N–body problem. These features were developed in the 1970ies and 1980ies and termed "Chain Regularisation". The mathematical method is described in more detail by Aarseth (1993), Mikkola (1997) and references therein.

8 Organization of the simulations

Although many studies in stellar dynamics use single mass models, it is essential to take into account a realistic mass spectrum, and the simple case of a bimodal mass spectrum is regarded as a first step towards that. Such two–mass simulations are exclusively studied in this work. Since this analysis aims to isolate the essential physical process of mass segregation, we ignore stellar evolution, cluster rotation and neglect a tidal field as well as primordial binaries; binary formation occurs only during the late stage of the evolution and do not effect our objectives.

8.1 Nomenclature

All simulations reported here start as Plummer spheres (Ch. 3) in global virial equilibrium. The particles are treated as point masses, i.e. without softening of the gravitational force, but regularization of close encounters instead (Ch. 7.4). In our notation, a **model** will be determined by its fraction of the heavy mass component, $q = M_2/M_{\rm tot}$, and the mass ratio of the individual particles, $\mu = m_2/m_1$. The model is assigned to a capital Roman letter. Each model consists of a number of **runs** that differ only in their random number seed; it returns no more than another initial setup of positions and velocities of the particles. The runs are physically equivalent. Models making up a logical unit for comparison are gathered to a **series**, see Table 1.

Table 1: Overview of the simulations. A model is described by q and μ and assigned to a capital Roman letter. RND = random setup; INS = all heavy masses placed inside; OUT = all heavy masses outside.

Series	Distribution	q	μ–models	Remarks
I	RND	0.1	A ... H	various N
II	INS, OUT	0.1	A ... H	all m_2 inside / outside
III	RND	0.05	K ... R	$N = 2500$
IV	RND	0.2	T ... Z	$N = 2500$
V	RND	0.4	T′ ... Y′	$N = 2500$
VI	RND,INS,OUT	0.26	20.0	$N = 5000$, Orion Nebula

Inspired from a result of Inagaki & Wiyanto (1984) that a cluster evolves fastest for $q = 0.1$, we concentrate our main investigations on that value (Series I), and study the evolution for a wide range of μ's (from 1 to 50). This choice is guided by observations in youngest star clusters like the Trapezium in the Orion Nebula Cloud, where a mass range of $\approx$ 0.1–50 $M_\odot$ is found (Hillenbrand & Hartmann 1998). This cluster also exhibits clear mass segregation that cannot be explained by the simple theory of "general" mass segregation driven by two–body relaxation. Given the extreme youth of the stars with highest mass, a primordial segregation has been suggested, in which they were formed by a runaway growth at locations close to the dense centre (Bonnell & Davies 1998).

We examine the time scales for a random setup of particles (RND) that is realized by assigning a mass m_1 and m_2 to each body. With μ being a relative quantity, we fix m_1 to unity, and vary m_2 in steps that are given in the top row of Table 2. So, the two mass populations have got N_1 and N_2 members (for the determination of their numbers see next section), whose spatial coordinates are given by random numbers placing them along the Plummer sphere (method by Aarseth, Henon & Wielen 1974). The velocities are scaled in accord to the virial ratio of the kinetic and potential energy.

In Series II, we place the heavy particles completely either in the centre (INS) or to the outskirts (OUT) and compare the evolutionary patterns with the random setup of Series I. In Series III, IV and V we alter the fraction of heavy masses, q, to test for this parameter. The full parameter space is graphically illustrated in Figure 8.1. Moreover, we performed simulations of a special configuration, which is related to a mass ratio in the Orion Nebula Cloud (Series VI).

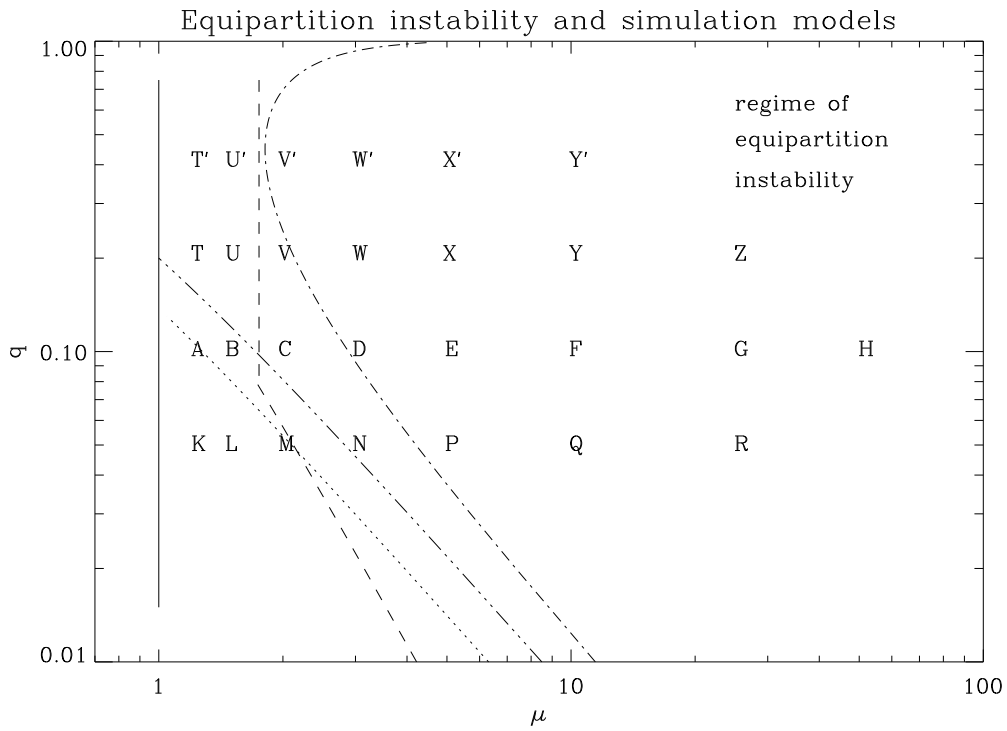

Figure 8.1: Parameter space of the models examined in this work. The position of the Roman letters indicate a model determined by its q and μ. The dotted line is the boundary of the equipartition stable region after Spitzer (1969), eq. (30); The dashed–dotted line is the stability criterion after Lightman & Fall (1978), eq. (37); the dot–dot–dot–dashed line is the formula eq. (40) by Inagaki & Wiyanto (1984); and the dashed line is the empirically proposed condition by Watters *et al.* (2000), eq. (41).

Usually, we are not interested in the results of one particular run, but in the average behaviour of several runs with identical parameters, i.e. we are interested in the properties of the model. In order to reduce the statistical noise, we performed a large number of runs and averaged the data set into an ensemble–model. The statistical quality of such an ensemble–averaging is comparable with one single calculation containing the full particle set of all runs (Giersz & Heggie 1994a). For example: Since most of our models are clusters with $N = 2500$ particles (our "standard" case), we carried out 20 runs and the whole set would represent one single run containing $N = 50{,}000$. In Series I, we also performed 50 runs for $N = 1000$, and 10 runs for $N = 5000$. These runs were performed on the PCs of the Linux–cluster of the Astronomisches Rechen–Institut, Heidelberg, Germany. One typical 5000–particle run of Model A lasted about 160 CPU–hours (7—8 days) on an 800 MHz Pentium III until it reached core collapse.

Additional models containing 10,000 particles (4 runs) and 20,000 particles (1 run) were calculated on the CRAY T3E parallel computer at the Hochleistungsrechenzentrum in Stuttgart. The run with $N = 20{,}000$ was started on 128 processors, but when it approached core collapse, the number of processors was reduced to 16. This A–model used nearly 1350 CPU–hours (two months) till collapse.

8.2 Parameters of two–mass models

In order to describe a model, a set of three parameters is needed:

$$N = N_1 + N_2; \qquad \mu = m_2/m_1; \qquad q = M_2/M_{\rm tot}. \tag{55}$$

Since the number of the force calculations scales with N^2, computational efforts restrict the choice of N, therefore this value has to be fixed as well as an appropriate number distribution N_i for the i-th mass–component found. While N is chosen to the aptitude of the computers used, particular models are conveniently distinguished by μ and q. The definitions give:

$$\begin{aligned} q &= \frac{M_2}{M_1+M_2} = \frac{m_2 N_2}{m_1 N_1 + m_2 N_2} \\ &= \frac{m_1 \mu N_2}{m_1 N_1 + m_1 \mu N_2} \\ &= \frac{\mu(N-N_1)}{N_1 + \mu(N-N_1)}. \end{aligned} \tag{56}$$

The absolute number of light particles is then

$$N_1 = \frac{(1-q)\mu N}{q - \mu q + \mu}. \tag{57}$$

Some authors (e.g. Inagaki & Wiyanto 1984) define a slightly different parameter $\hat{q} = M_2/M_1$, then equation (57) turns into $N_1 = \mu N/(\hat{q}+\mu)$. In the following, we continue to stick to the notation of Spurzem & Takahashi (1995), as defined in (55). In the models of Series I ($q = 0.1$), the absolute numbers of the heavy particles, $N_2 = N - N_1$, are shown in Table 2. μ is given in brackets on top of each column.

Table 2: Absolute numbers of heavy stars for models of Series I.

N	A (1.25)	B (1.5)	C (2.0)	D (3.0)	E (5.0)	F (10.0)	G (25.0)	H (50.0)
1000	82	69	53	36	22	11	4	–
2500	204	172	132	89	54	27	11	6
5000	408	345	263	179	109	55	22	11
10,000	816	690	526	357	217	110	44	22
20,000	1633	1379	1053	714	435	220	88	44

A different way of fixing the mass ratio μ is by means of the average mass of the stars:

$$\tilde{\mu}_i = m_i/\langle m \rangle, \tag{58}$$

where $\langle m \rangle = M_{\rm tot}/N$ and m_i is the i-th component in a multi–mass cluster. With $q_i = M_i/M_{\rm tot}$, we have for the general case of k different mass components

$$N_i = \frac{q_i N}{\tilde{\mu}_i} = \frac{\langle m \rangle q_i N}{m_i} = \frac{M_i}{m_i} \tag{59}$$

particles in the i–th mass bin. The advantage of this expression lies in the simpler handling, if more than two masses are present. In the equation (57), $(k-1)!$ parameters of m_i/m_j would be necessary for k mass components, while here the usage of $\langle m \rangle$ reduces the amount of the a–priori–definitions of m_i's to $k-1$.

8.3 Nbody–units

Dimensionless units, so–called "Nbody units", were used throughout the calculations. They are obtained when setting the gravitational constant G and the initial total cluster mass M equal to 1, and the initial total energy E to $-1/4$ (Heggie & Mathieu 1986; Aarseth, Hénon, Wielen 1974).

Since the total energy E of the system is $E = K + W$ with $K = \frac{1}{2}M\langle v^2\rangle$ being the total kinetic energy and $W = -(3\pi/32)GM^2/R$ the potential energy of the Plummer sphere, we find from the virial theorem that

$$E = \frac{1}{2}W = -\frac{3\pi}{64}\frac{GM^2}{R}. \tag{60}$$

R is a quantity which determines the length scale of a Plummer sphere, namely its virial radius. Using the specific definitions for G, M, and E above, this scaling radius becomes $R = 3\pi/16$ in dimensionless units. The half mass radius $r_{\rm h}$ can easily be evaluated by the formula (e.g. Spitzer 1987):

$$M(r) = M\frac{r^3/R^3}{(1 + r^2/R^2)^{3/2}} \tag{61}$$

when setting $M(r_{\rm h}) = \frac{1}{2}M$. It yields $r_{\rm h} = (2^{2/3} - 1)^{-1/2}R = 1.30\,R$. The half–mass radius is located at the scale length of $R = 0.766$, or about 3/4 "Nbody–radii".

It is also convenient to choose a unit of time that is proportional to the relaxation time, rather than to the crossing time. The initial half–mass crossing time of a particle is

$$t_{\rm cr} = \frac{GM^{5/2}}{(2E)^{3/2}}. \tag{62}$$

Since the Nbody–unit of time, $t_{\rm NB}$, is 1 when

$$t_{\rm NB} = \frac{GM^{5/2}}{(-4E)^{3/2}}, \tag{63}$$

immediately follows that $t_{\rm cr}/t_{\rm NB} = 2\sqrt{2}$. In fact, this time is not related to any meaning in cluster physics, but it is just an easy handling of the time measurement in simulations. However, it can be shown that the factor $2\sqrt{2}$ is rather close to the crossing time at half–mass radius in a Plummer sphere.

9 Results for $q = 0.1$

This chapter deals with the results of the simulations on two–component star cluster evolution if the fraction of heavy stars make up 10% of the whole cluster mass. We investigate the physical processes occurring from a random initial distribution and compare them with previous studies. The essential facts about the evolution have been introduced in Chapter 4 and are qualitatively visible in Figure 9.2: The core radius shrinks with time, and the cluster collapses under its self–gravity. The time scale for the collapse is the more shortened the larger the ratio of individual stars gets. The core collapse is shifted to smaller time values. The formation of binaries in the core stop the collapse and let it expand again. We direct our attention on the variations of the evolutionary processes for different μ.

9.1 Data of ensemble averages

We varied μ from 1.25 to 50.0 and obtained the core collapse time, $t_{\rm cc}$, for each run by considering two values: first, the moment of the minimum core radius, $t(\mathrm{r_c} = \min)$ and, second, the deepest central potential, $t(\Phi = \min)$. The output data was written each Nbody time unit. Because of large fluctuations between two subsequent data points, we applied a "smoothing function" over $r_{\rm c}$ and Φ, which returns an averaged value of a boxcar of the specified width w ("smoothing window"). The function works by the algorithm

$$R_i = \frac{1}{w} \sum_{j=0}^{w-1} A_{i+j-w/2}, \tag{64}$$

where R_i is the resulting value of the original variable A_i having been averaged among w neighbouring data points. The choice of $w = 5$ turned out to be useful with respect to both, clearing out noisy peaks and maintaining precision (an example for the raw data is shown in Figure 9.9). The median of the times found from the minima of $r_{\rm c}$ and Φ was taken to be that special run's core collapse time:

$$t_{\rm cc} = \frac{t_{r_{\rm c}} + t_\Phi}{2}. \tag{65}$$

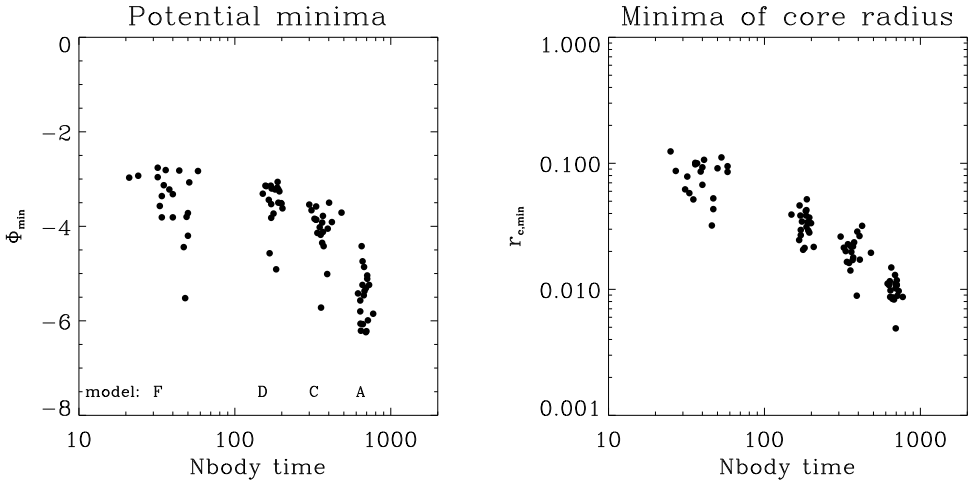

Figure 9.1: Models A, C, D, and F of Series I with $N = 2500$. Each point represents the minimum value of the central potential $\Phi_{\rm c}$ (*left*) and core radius $r_{\rm c}$ (*right*) at the time when these parameters attain their minimum. The average values for all models are listed in the Appendix.

Figure 9.1 illustrates the distribution of the data points of $r_{\rm c}$ and $\Phi_{\rm min}$ at their corresponding core collapse times for four selected models. The logarithmical time–axis was chosen to show the relative scatter between the point clouds. When viewed at a particular run, the core collapse times are likely to show a significant discrepancy between the determination from the potential or from the core, i.e. t_Φ does not necessarily equal $t_{\rm r_c}$, but the averages of both kinds, $\langle t_{\rm r_c}\rangle$ and $\langle t_\Phi\rangle$, coincide well for the whole model. So, $\langle t_{\rm cc}\rangle$ is a good value to characterize the core collapse time of the model, anyway:

$$\langle t_{\rm cc}\rangle = \frac{\sum\left[(t_{\rm r_c}+t_\Phi)/2\right]}{N_{\rm runs}} \approx \frac{\langle t_{r_{\rm c}}\rangle + \langle t_\Phi\rangle}{2}. \tag{66}$$

As seen in the figure, the relative variance of the core collapse times increases for smaller values of $\langle t_{\rm cc}\rangle$. Since the core collapse is driven by two–body relaxation, it shows virtually the equivalent problems in its determination: For high μ's, the relaxation time becomes very short in the centre, and, consequently, the exact moment of the minima Φ and $r_{\rm c}$ is difficult to fix. Additionally, the depth of the collapse is not clearly distinct (see next section) such that an ambiguity arises when fixing a peak for the moment of collapse.

The mean values for the eight models of our Series I are summarized in the Table in the Appendix. The errors given there are the standard deviation from the runs' mean $t_{\rm cc}$, divided by the square root of the number of the runs $\sqrt{N_{\rm runs}}$. The error of $\langle t_{\rm cc}\rangle$ is roughly 2–5% for most of the models, consistent with the relative errors determined by Spurzem & Aarseth (1996) and the half–mass evaporation times by Baumgardt (2001).

9.2 Evolution of the core radius

The evolution of the core radii for the models A–G is plotted in Figure 9.2. Each curve is an ensemble average of 20 runs. For models with μ approaching to unity, the core radius shrinks as in an equal–mass system (at late collapse times, to the right). A linear time scale (not shown here) suggests that the collapse phase sets in when the core radius has contracted to about 25% of its initial radius. This is in agreement with the results of Giersz & Heggie (1994a). For high μ's, the infall begins immediately from the start of the simulations. The rapid contraction of $r_{\rm c}$ is due to the very massive stars falling quickly to the centre on the crossing time scale. The contraction stops at higher $r_{\rm c}$–values than for the low–μ models, and a quick expansion of the core follows.

The behaviour at the moment of core bounce is illustrated in Figure 9.3, where the minima of the potential and the core radius are plotted versus μ. For a fixed N and moderate $\mu \approx 3$ — 10, the core collapse is carried out by approximately the same number of particles, but they do not draw together as close as for the equal–mass case or very small μ's. Therefore, the density and the central potential are less deep than for $\mu \lesssim 2$, and the minimum of the core radius is not so profound. At extraordinary high μ's, the effect is reversed: Even some few heavies are massive enough to deepen the potential due to their mere existence. The collapse itself is less distinct, as seen from the shallower $r_{\rm c}$ in the right panel. In the intermediate μ–regime ≈ 3 – 10, the depth of the potential results from the combination of these two effects: Heavy masses build up a strong gravitational field, but their kinetic motion does not allow a long–lasting vicinity. It is only natural that equipartition becomes impossible (Chapter 11). The differences of the depths for *various* N are discussed in Section 9.6 below.

The development after the collapse appears indifferent. The theory by Goodman (1987) proposed an expansion of both, the half–mass and the core radius, as

$$r_{\rm c} \propto (t - t_{\rm cc})^{2/3}. \tag{67}$$

This results from the fact, that the cluster maintains a constant total mass during the expansion (ejection from three–body interactions is ignored):

$$M_{\rm c}\,(t) \propto \rho_{\rm c} r_{\rm c}^3 = {\rm const.}, \tag{68}$$

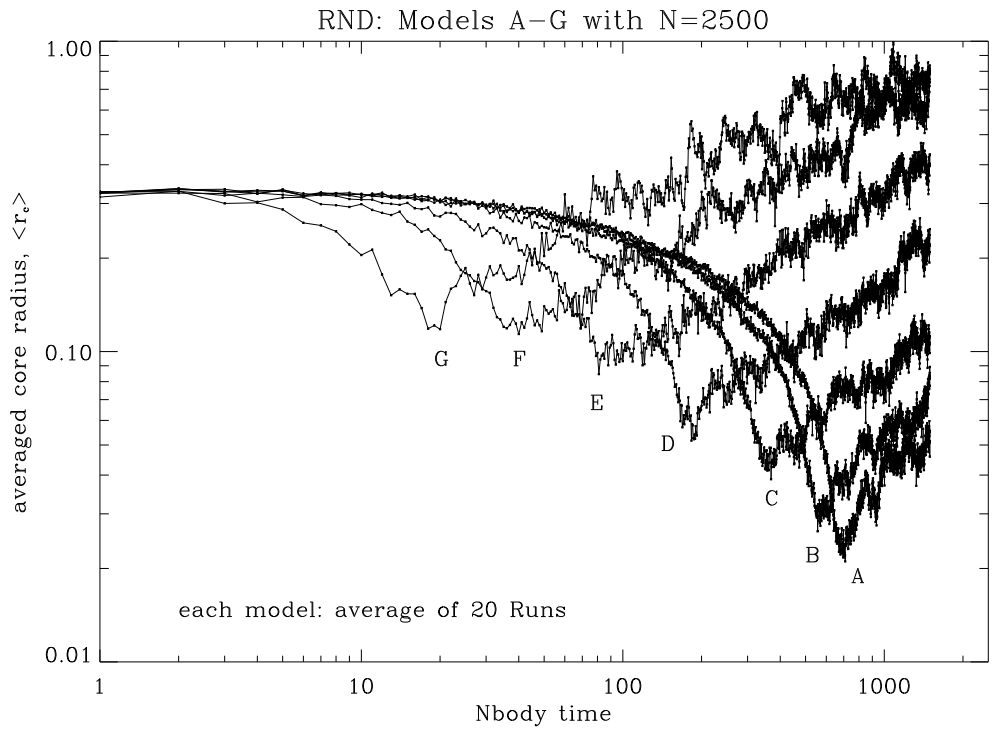

Figure 9.2: Comparison of the shrinking core radius in the models A–G of Series I.

where the index c denotes the quantities for the core. Since the central density ρ decreases proportional to t^{-2} (Spurzem & Takahashi 1995), the post–collapse evolution goes as the two–thirds power–law in the formula (67).

We measured the slopes of the expanding r_c's in Figure 9.2 by fitting two straight lines embracing the fluctuating data of each model to construct an upper and a lower margin. These lines give two (more or less) independent measurements for the slope and are presented in Table 3, and they show a decreasing trend for higher μ.

Table 3: Measured slopes of the core radii in the post–collapse phase.

slope	A	B	C	D	E	F	G
up	0.631	0.666	0.680	0.525	0.522	0.490	0.420
low	0.940	0.864	0.662	0.615	0.524	0.517	0.445
mean	0.7855	0.765	0.671	0.570	0.523	0.5035	0.4325

The results actually incorporate two biases. First, the lower lines seem to be steeper than the upper ones for the most of the models. The reason for that is not clear, but it is likely an error in the precise determination of the cutting points at the logarithmical axes. Second, the simulations reach different stages of the post–collapse evolution, and the expanding branches exhibit different lengths. Especially, the low–μ models (A and B) are not far advanced for precise measurements, while the high–μ models (F and G) appear distorted too much about the time of collapse such that the onset of the self–similar expansion is difficult to find (see also Giersz & Heggie 1994b). So, we cannot judge definitively whether or not the core expansion is really the same for all of our models. From the theoretical point of view, there is no argument for a different behaviour of the core expansion when unequal masses are present.

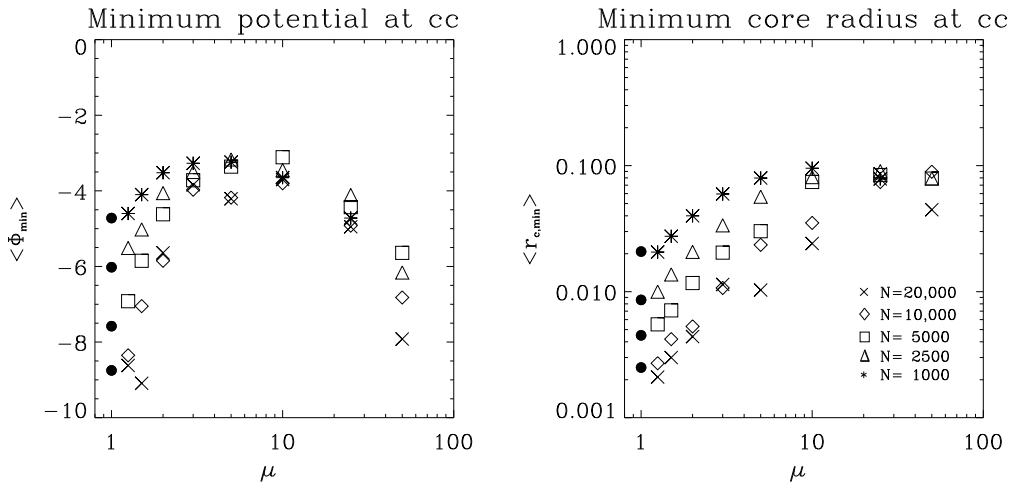

Figure 9.3: Minima of potential (*left*) and core radius (*right*) at the moment of core bounce. The collapse is carried out by a less number of core particles when μ rises. See text for explanations in more detail.

9.3 Core collapse times

It was stated before that the nucleus consisting of two mass–components collapses in a time shorter than the equal–mass cluster by a factor of $1/\mu$ (Khalisi & Spurzem 2001; Fregeau *et al.* 2002). This is reasonable, because the equipartition time is shortened according to eq. (18). The left panel of Figure 9.4 shows new and more detailed calculations in a wider μ–range. The mean times, $\langle t_{\rm cc} \rangle$, have been plotted versus μ for the complete sample of our models in Series I, the simulations with $N = 2500$ are connected with a solid line for optical clarity. The circles at left are the collapse times for an equal–mass cluster according to eq. (17), and the dotted line is the stability boundary by Spitzer with $\chi_{\rm max} = 0.16$, eq. (29).

In the left panel, the core collapse times converge smoothly against the collapse time for an equal–mass cluster, $t_{\rm cc,1}$, as μ approaches unity. The non–linearity in this region is a clear evidence that equipartition mingles with the gravothermal instability. Between $\mu \approx 2$ and 10, a somewhat linear decline is visible, but far beyond the stability boundary, the core collapse times run towards a constant value. That constant can be regarded as the minimum time for the high masses to reach the cluster centre and collapse in the frame of their own subsystem.

In the right panel, the factor of "collapse acceleration" is plotted for various μ's. It is to be a measure to which percentage a cluster with two masses of ratio μ evolves faster than its analogue with equal masses. The dashed line is the μ^{-1}–decline of expectation, i.e. a cluster with two mass–species having a ratio μ would collapse μ-times earlier than its single–mass equivalent according to

$$t_{{\rm cc},\mu} \propto \frac{1}{\mu} t_{\rm cc,1}. \tag{69}$$

At $\mu = 2$ the decoupling of the equipartition–based instability and the gravothermal instability takes place. For $\mu \longrightarrow 1$, the evolution proceeds slowlier than the $1/\mu$–decrease, because the tendency to equipartition drives the initial evolution and slows down a "purely" gravothermal collapse. As the mass difference between m_2 and m_1 becomes marginally, the system collapses like a single–mass cluster. Beyond the critical value $\mu = 2$, an early decoupling of the two mass populations occurs. The heavies try to reduce their large velocity dispersion, but they rapidly accumulate at the centre and interact preferably with themselves. As a consequence, equipartition is harder and harder to achieve and the evolution proceeds only due to the redistribution of heat within the two, almost separated

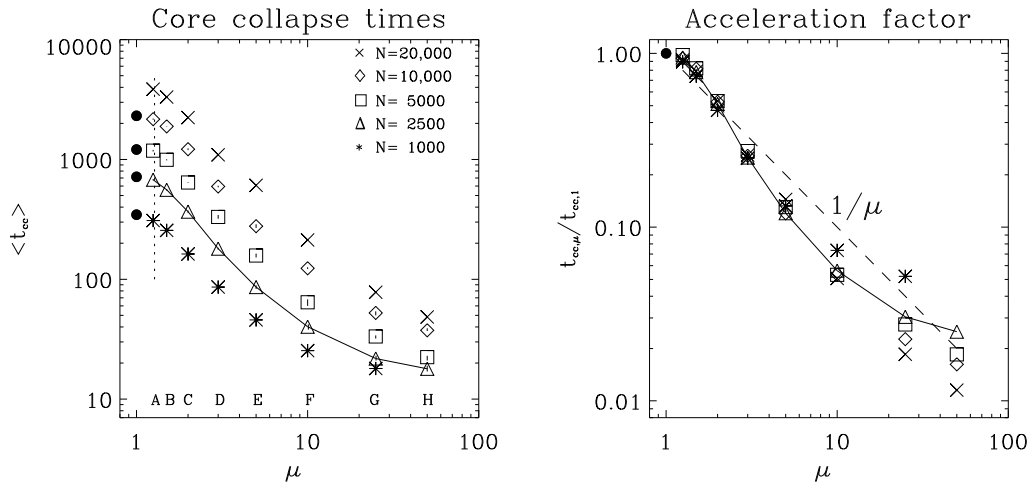

Figure 9.4: *Left*: Core collapse times of the models in Series I. The times shorten non–linearly with increasing μ. The dotted line at $\mu = 1.275$ is Spitzer's (1969) equipartition criterion given in eq. (29) for value of $\chi_{\max} = 0.16$ and $q = 0.1$. The core collapse times of the corresponding equal–mass clusters are indicated by filled dots. The error bars are smaller than the symbols. *Right*: All collapse times divided by the $t_{\mathrm{cc},1}$ of the corresponding equal–mass simulation.

components (Bettwieser & Inagaki 1985). The light stars evaporate out of the core and take away the thermal energy to the outskirts, while the heavies increase their binding energy. The latter ones collapse like a single–mass subcluster. The combined process, the release of energy by shrinking of the heavy component and the heat transfer by the light stars, works effectively and leads to an accelerated collapse.

If $\mu \gg 1$, the situation turns into a case of dynamical friction: A handful of particles are drowned into a homogeneous sea of light stars, and, like in an ordinary frictional drag, their motion suffers a deceleration. The core collapse of the system is not a direct matter of the few heavy masses anymore, so the curvature of the solid line at high μ's should be considered with care. It is instructive to see, that only for large N, the *absolute* number of heavy stars seems sufficient enough to maintain the linear slope of accelerated cluster evolution. The slope follows the dashed line a bit longer before bending towards that constant value. We expect that the μ^{-1}–decrease will be seen more clearly for even larger particle numbers.

9.4 Mass segregation

The process of mass segregation for the six models A–F is illustrated in the Figure 9.5, where the mean mass of the stars, that are inside a specified "Lagrangian shell", is shown (a Lagrangian shell is the volume between two Lagrangian radii, which contain a fixed mass fraction of the bound stars in the system; see [21]). The mean mass is computed by $\langle m \rangle = (m_1 N_1 + m_2 N_2)/(N_1 + N_2)$; since the total mass of the system is scaled to 1 for the sake of N–body units (Ch. 8.3), one low mass star becomes actually slightly smaller than $1/N$, while a heavy one is larger. This does not alter the discussion, because μ is a *relative* quantity of masses, which is always exactly kept. In Figure 9.5, the y–axis was multiplied by N for handy values, and the mean mass for each model is also indicated.

The process of mass segregation proceeds as follows. With the light and heavy masses randomly distributed, each shell exhibits the same average mass at the beginning. In the course of the evolution, the inner shells assemble the heavy bodies, and raise the mean mass. The half–mass radius and the outer shells lose their heavy stars rather quickly and remain below the value for the average

mass, because the light ones outnumber the heavies significantly. The cluster is stratified by mass, then. Note, that all shells remain rather static throughout the calculation.

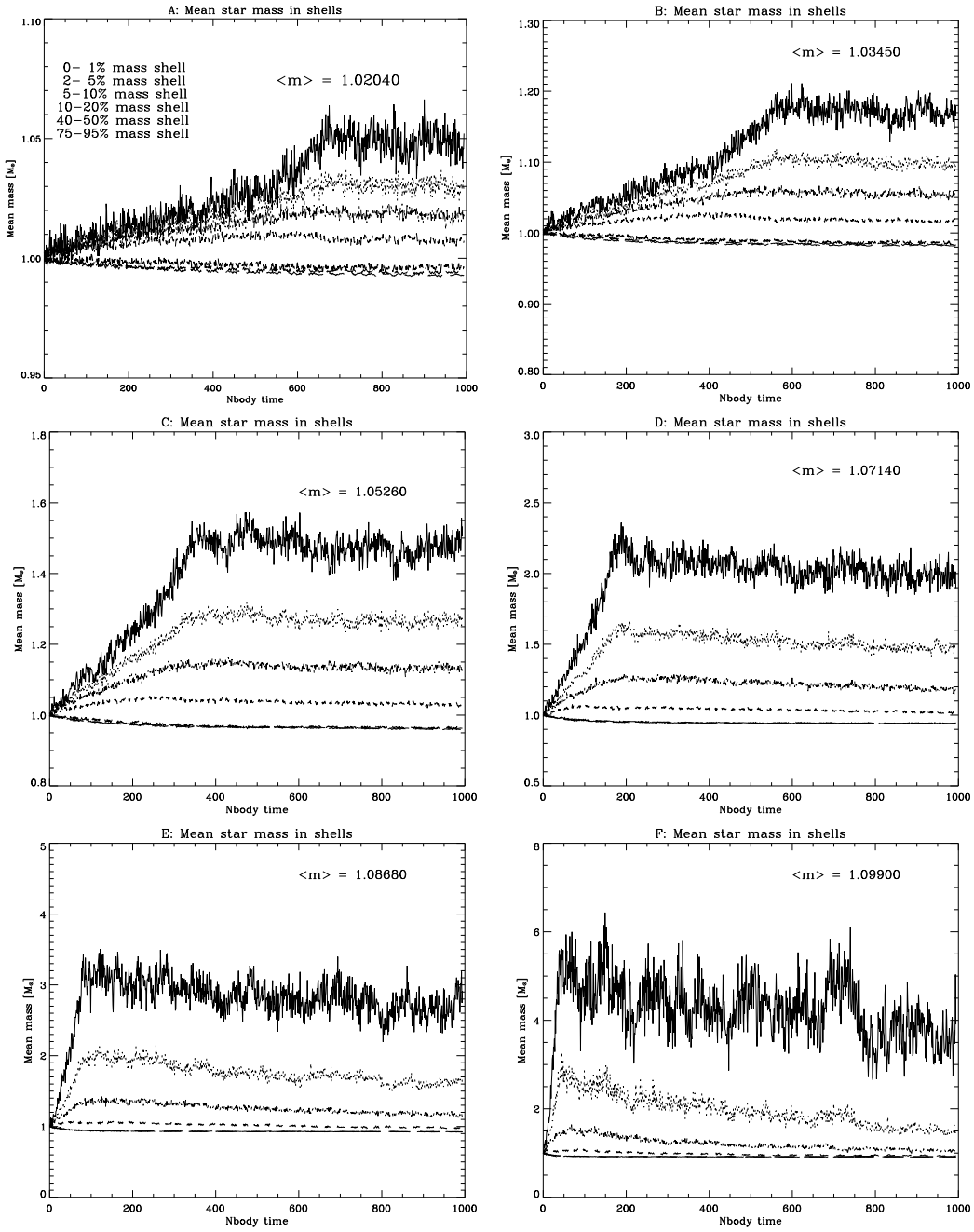

Figure 9.5: Average mass in Lagrangian shells for models A–F show the stratification of masses in the cluster. The segregation of heavy masses proceeds in agreement with the global evolution of the cluster. The mean mass is indicated.

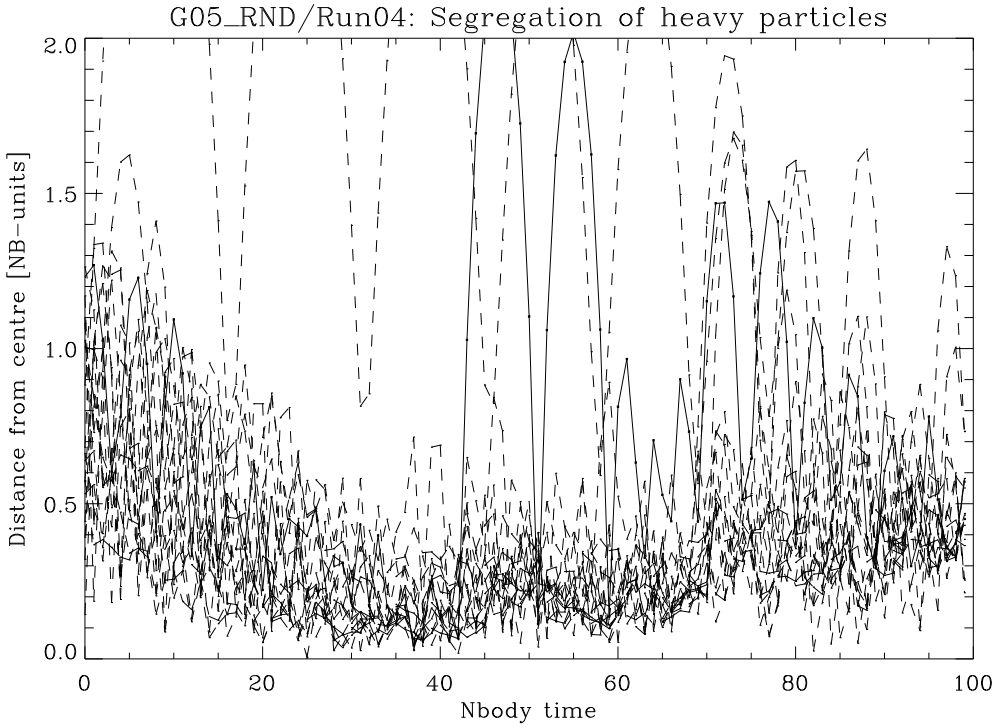

Figure 9.6: Distance moduli of 18 heavy mass particles in Model G with $N = 5000$. Each of the particles has got a mass 25 times larger than a light particle (their orbits not shown). The core collapse of this run occurred at $t_{\rm cc} = 33.5$.

The segregation of masses propagates simultaneously with the contraction of the core. Giersz & Heggie (1996) have already noticed the self–similarity of this process: In the models A and B it is nicely seen how the inner layers decouple stepwise one after the other until the final stage is reached. After the collapse, the profile does not change much, so, the effect has only influence on the early evolutionary phase, as expected, not in the post–collapse. The moderate decline in the models E and F can be explained by the heavy particles escaping: Because of their relatively small absolute number (see Table 2), they get ejected from the core and leave the cluster such that the surplus of small bodies depletes the mean value in the shells. A handful high–mass stars in the centre interact strongly in a few–body process and kick out each other, and the core is gradually "evacuated" from the perturbers. In our data we find an enhanced fraction of high–mass escapers occuring immediately after the collapse confirming this scenario; many of them exhibit enormous kinetic energies and some even escape as bound binaries (see Sec. 9.5). However, some heavy latecomers enter the inner regions, but a balance is found between the incoming and outgoing mass flux. In general, the dynamical processes in the core do not influence the properties of the cluster as a whole.

The mean mass in the 1%–Lagrangian shell never attains its full "capacity", i.e. the value of m_2, which could principally be gained if this shell was completely populated by heavy stars. It means that there is always a number of low–mass stars intruding and leaving the innermost region that keep $\langle m \rangle_{1\%}$ at a constant fraction of the maximally attainable level. This level is at about $0.8\,m_2$ if μ is small, and drops to $0.5\,m_2$ for the highest μ's. In this sense, the system "adjusts" its layers to an appropriate ratio of light and heavy stars, and picks up a constant flux of incoming and outgoing particles. The height of $\langle m \rangle$ in the innermost shell may depend on N slightly, but this kind of variation is not as clear as the variations on μ.

Another illustration of the segregation process is given in Figure 9.6. It shows the shrinking

distance moduli of 18 heavy–mass stars of one typical run of a model with a high mass–ratio (Model G, $\mu = 25$, Run no. 4, $N = 5000$); this model consists of 22 heavy mass stars initially, but 4 stars escaped at some time before the final plotting time unit, and they were excluded from the plot. 17 dashed lines were overlapped demonstrating how the orbits of most particles draw rapidly closer. The core collapse occured at $t_{\rm cc} = 33.5$. A solid line lifts off one particle of example that was knocked out of the chaotic region due to a close encounter, but its kinetic energy was not sufficient enough to leave the system. It segregated inwards again. One other particle, whose pericenter was at 0.9 Nbody–radii, remained in the halo and did not take part in the collapse, but it sank to the intermediate distances at about $t_{\rm cc} \approx 70$.

9.5 Escapers

The escape of stars has been studied many times in the past. The estimation of escape rates is often based on idealized models, whose simplifying treatments sometimes lead to different results. The complexity of this topic is reviewed by Meylan & Heggie (1997). We just give some keywords in order to outline the scope of the problem:

- Theories based on relaxation phenomena yield a different escape rate than theories involving individual two–body encounters; the former is often denoted as “evaporation”, the latter is related to “ejections”.
- The rate of escape is not a constant, while the evolution of the system proceeds, even in the pre–collapse phase.
- An increasing concentration in the core as well as the growth of anisotropy tends to enhance the escape rate.
- Furthermore, the escape rate is strongly mass dependent; different mass spectra and segregation alter it.
- A tidal field lowers the threshold for escape.
- A sufficient abundance of binaries (both, primordial and formed ones) has a substantial effect on high–velocity escapers which take away energy from the system and change the environmental constraints.

In view of these complications, care must be taken in the interpretation of the data. Nevertheless, we want to contribute to the list of simplified theories by our latest N–body simulations investigating the rates for various particle numbers and the variation on μ, in particular.

An escape is defined by a particle having both positive energy and its distance from the density centre exceeding a limiting radius. We have chosen the distance to be 20 times the half–mass radius, $r_{\rm h}$. The particles were removed from the calculation from a time when both conditions were fulfilled; we shall call them “removed escapers”. We will draw our attention only to escapers occured before the time of core collapse, $t_{\rm cc}$. Besides that, one run contains a number of particles which have gained positive energy but not reached the distance for a removal yet. Such kind of particles dominate when $t_{\rm cc}$ is extremely short. In particular, the high–μ models collapse within a few tens of Nbody–time units, and a large number of particles, that are going to escape, would be missed. This condition resembles the “energy cut–off” (Baumgardt 2001), and we shall call these particles “potential escapers”. Whether some of them will be scattered back to become bound members again or really escape, is a complex process that is out of the scope of our subject. Baumgardt (2001) estimated that a fraction of 2% of the potential escapers might return to the system. As a first approach to the general properties of escapers, we will account to the number $N_{\rm esc}$ all removed escapers plus potential escapers at the epoch of $t_{\rm cc}$. Because of the scatter of the core collapse times (Section 9.1), each run

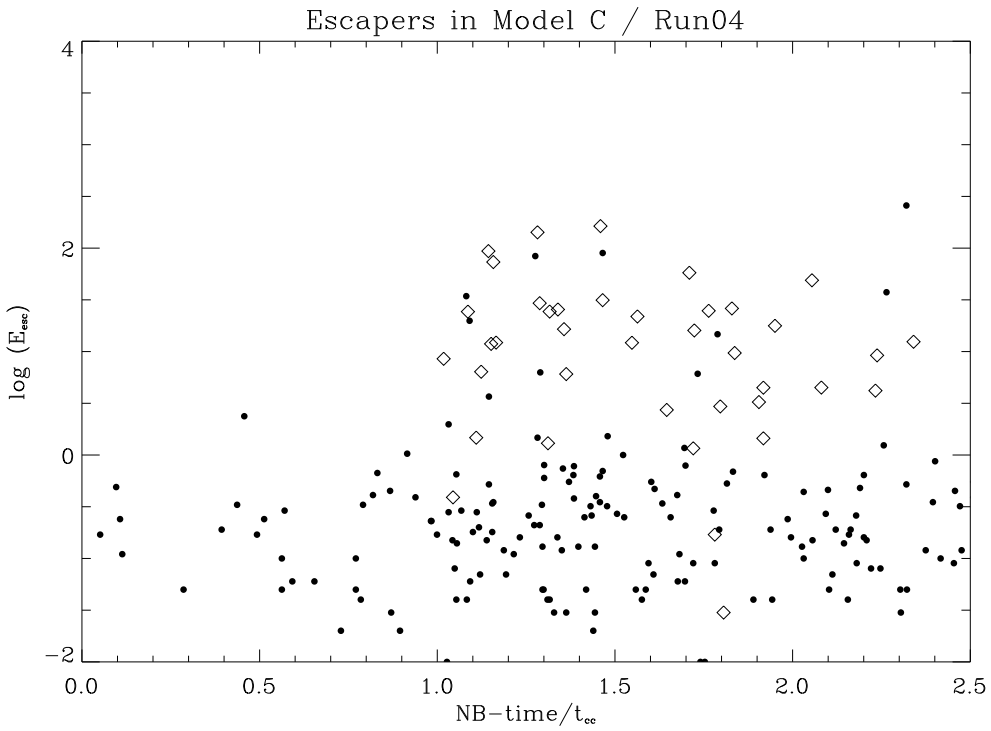

Figure 9.7: Model C ($\mu = 2.0$), Run no. 04, with $N = 5000$. Energy of an escaping particle is given in units of $k_{\rm B}T$ and plotted against its escape time scaled to the core collapse. Diamonds denote heavy masses.

was checked separately for its escapers that occured before that run's individual core collapse time — not the ensemble's $\langle t_{\rm cc}\rangle$. $\langle N_{\rm esc}\rangle$ is the average among the these individual $N_{\rm esc}$'s, divided by the square root of the number of runs performed.

Figure 9.7 gives a typical example for the energy distribution of all removed escapers in one run of Model C with $N = 5000$; the potential escapers are disregarded here. The energy is measured in units of $k_{\rm B}T$ and plotted against the time of removal; light bodies are represented by filled dots, heavy ones of $m_2 = 2.0$ by diamonds. The collapse occured at $t_{\rm cc} = 643.5$ for this run. In the beginning, the light particles diffuse slowly from the system with small energies (evaporational effect). After the core collapse, the mass dependence is more complicated, for a second class of escapers joins: high–energy particles, whose energies are higher by two orders of magnitude. A fair fraction of the escapers are heavy stars. As in the statistics for equal–masses by Giersz & Heggie (1994a), it is natural to associate them with ejected stars that go back to three–body interactions in the very centre. Mass segregation has widely finished at the time of core collapse, and interactions in the core start depleting the high–mass population. Other runs of the same model exhibit a similar picture.

The analysis of the models in regard to μ reveals interesting views on the escape mechanism. A summary is shown in Figure 9.8, and the legend for the symbols is given in panel (e). The error bars are usually omitted, though they are given for the $N = 2500$ set (triangles) except in the panels (c) and (d); the error bars are almost invisible in (c), and larger than the panel size in (d), because the number of high–mass escapers varies a lot among one model.

Panel (a) gives the fraction of escaped stars, $\langle N_{\rm esc}\rangle/N$. In a single–mass cluster ($\mu = 1$) about 2.5% of the stars leave the system before it collapses. When introducing a second mass, this fraction drops to 0.2–0.5% until $\mu \approx 3$. The reason is that the rate of escape (panel e) is nearly constant for small μ, but the shorter collapse times cause a smaller progress of the escape mechanism, thus a smaller $N_{\rm esc}$. When massive bodies $m_2 \gg m_1$ are present, a larger fraction of stars receives

positive energy and turns into potential escapers. The N–dependent spread is due to the fact that the individual mass of a particle, m, scales with $1/N$ in our Nbody units, thus the threshold for an escape is lower.

Panel (b) gives the ratio of the removed escapers to the potential escapers as described above, $\langle N_{\rm rem}\rangle/\langle N_{\rm pot}\rangle$. For μ close to the equal–mass case, the core collapse time is large. Thus, the accumulated number of removed particles is larger by ≈ 10 times than the number of potential escapers at the moment of $t_{\rm cc}$. For high μ's, removed particles are scarce, while potential escapers did not have time to cross the cluster and turn into removed ones. Thus, the potential escapers make the overwhelming majority. The slope of the decrease is -1 , and it is identical with the shortening of $t_{\rm cc}$ when μ increases. The vertical dependence on N mirrors the increasing amount of removed escapers due to the longer $t_{\rm cc}$–times for larger N.

Panels (c) and (d) deal with the individual masses of the escapers. When one m_2 escapes, it raises the average escaper mass. In the models $\mu \gtrsim 10$, the *absolute* number of high–mass escapers is zero for most of the runs. This is the converse situation of panel (a): For massive stars, the escape is difficult. It is just 1 or 2 heavies appearing more or less accidentally and take away a significant fraction of mass from the cluster. They are rather evaporated objects than ejected in a close encounter, for their energies are relatively small. Their statistics are extremely poor, and the error bars are close to zero in panel (c) and extraordinary large in (d) for the shortage of m_2–counts. Usually, the heavy escapers occur in the late post–collapse phase and do not receive our attention here. From panel (d) and $\mu \leq 5$, we find that $\approx 3\%$ of all escapers are heavies which leave the system before $t_{\rm cc}$.

Panel (e) presents the rates of escape within a crossing time for different μ. The computation was adopted from Wielen (1975) as

$$\left\langle \frac{dN}{dt} \right\rangle = t_{\rm cr} \frac{\langle N_{\rm esc}\rangle}{\langle t_{\rm cc}\rangle}, \tag{70}$$

where the brackets denote averages among the runs within a model. For equal–mass clusters our rate is ≈ 0.2—0.3 in pretty accordance with other N–body results listed by Giersz & Heggie (1994a). The slight decline till $\mu \approx 3$ and the stronger increase afterwards is in excellent agreement with the theoretical expectation by Hénon (1969), his Figure 1. Though his models differ from ours in q, the branch of the curve related to our models exhibits the same shape. We interpret the curve such that two different mechanisms produce escapers in the pre–collapse phase under consideration: Relaxation dominates if the individual masses do not differ much, thus evaporation causes a steady mass loss from the system. When μ is increased slightly, $t_{\rm cc}$ drops, and the effect of evaporation cannot advance so far. The escape rate is also reduced then. For higher μ's another mechanism takes over: Massive stars exhibit a strong gravitational focusing. The gravity of one single heavy particle attracts more light stars and its energy is distributed among them. So, a multitude of light stars easily gains positive energy and heads for escape. The frequent two–body encounters of one heavy particle leads rather to ejections involving high energies than an accumulation of small escape energies.

Panel (f) of Figure 9.8 shows the mean energy carried away by the stars. The near constancy suggests an independence from μ, but a subdivision into removed and potential escapers (not shown here) reveals differences between the two groups. For removed escapers, the mean energy increases as much as a factor of 10 over the whole μ–range. This confirms the ejection scenario explained for panel (e). On the other side, the potential escapers show a constant but somewhat lower energies on average. Since they make up the larger fraction, the mean is depleted in the high–μ regime. However, a more careful computation is needed to confirm this point and to check how the mean energy is evolving when expanding the view to these potential escapers to the moment when they are removed in the post–collapse phase.

Finally, we can conclude that models resembling the equal–mass model tend to lose their mass by a slow evaporation process, while energetic ejections outweight in high–μ models. At $\mu \approx 3$, both processes are exchanging their dominant role. After mass segregation has come to a stop near core bounce, three–body encounters in the core start depleting the population of m_2–stars.

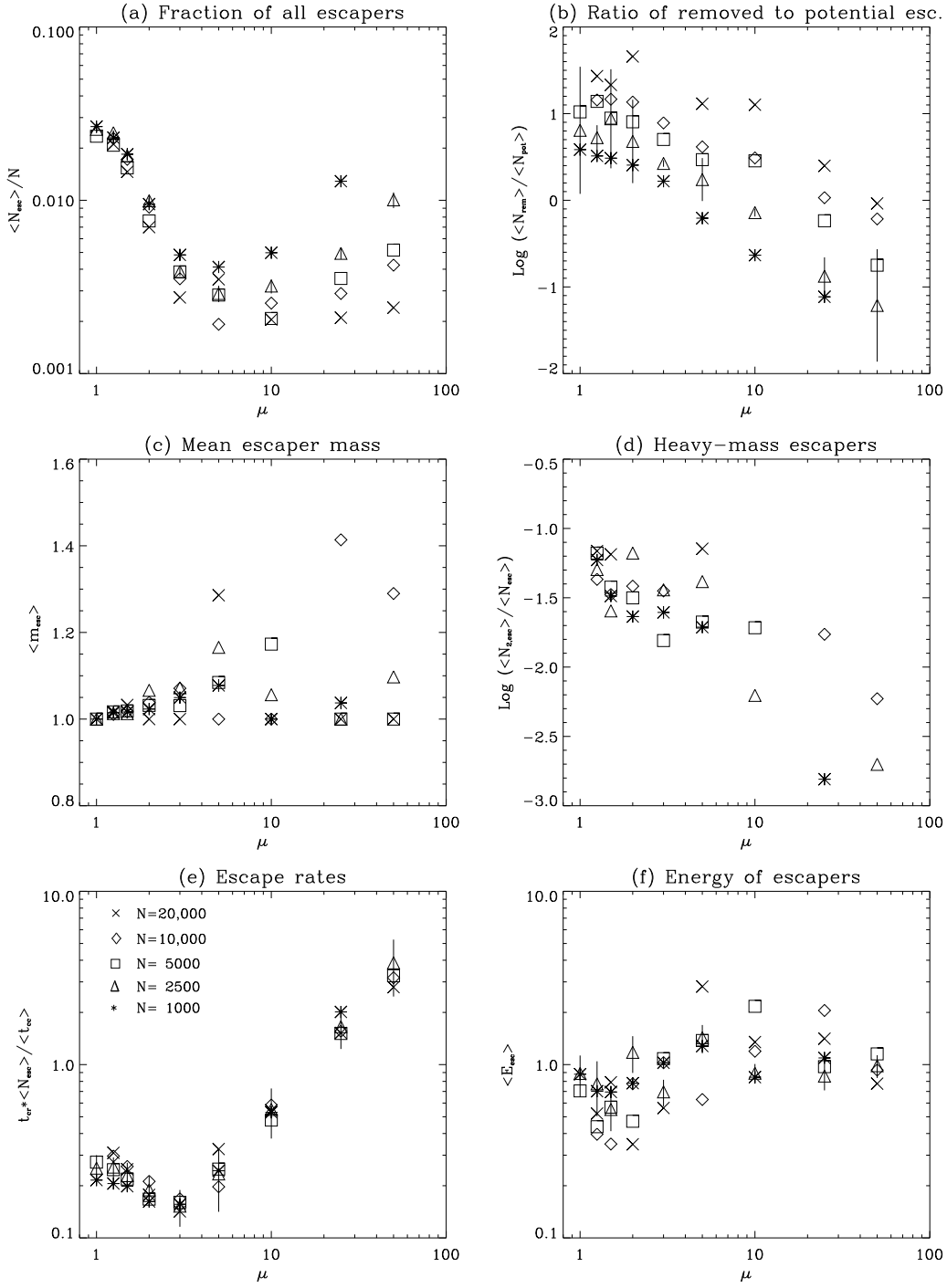

Figure 9.8: Summary of escaper data for the different models. (a) Fractions of removed escapers before the core collapse plus potential escapers at $t_{\rm cc}$. (b) Ratio of removed escapers to potential escapers. (c) Mean mass of escapers. (d) Relative number of m_2–escapers among all escaping particles. (e) Escape rates. (f) Mean energy of escapers in $k_{\rm B}T$.

9.6 Large particle numbers

Some dependencies on different particle numbers have already been touched in the foregoing sections. Here, we present a direct comparison of the cluster evolution for the A–models first. This model is close to the uniform mass case and has the longest evolution time. Figure 9.9 shows the raw data of the minimum potential for five runs, i.e. we applied no smoothing or averaging, but removed a couple of disturbing peaks. They are caused by two approaching particles that failed to regularization because they did not momentary fulfill the necessary criteria, but usually they are "caught" by the code in the subsequent time step (Ch. 7.4).

The most obvious feature, of course, is the increasing core collapse time in pretty accordance to the increasing relaxation time proportional to $N/\ln(\gamma N)$, eq. (15). Note, that the fluctuations of the data in the pre–collapse phase are smaller for higher N, because the global potential is smoother. In the post–collapse, the fluctuations are nearly the same, for the number of core particles, $N_{\rm c}$, is of the same order for each of the five runs.

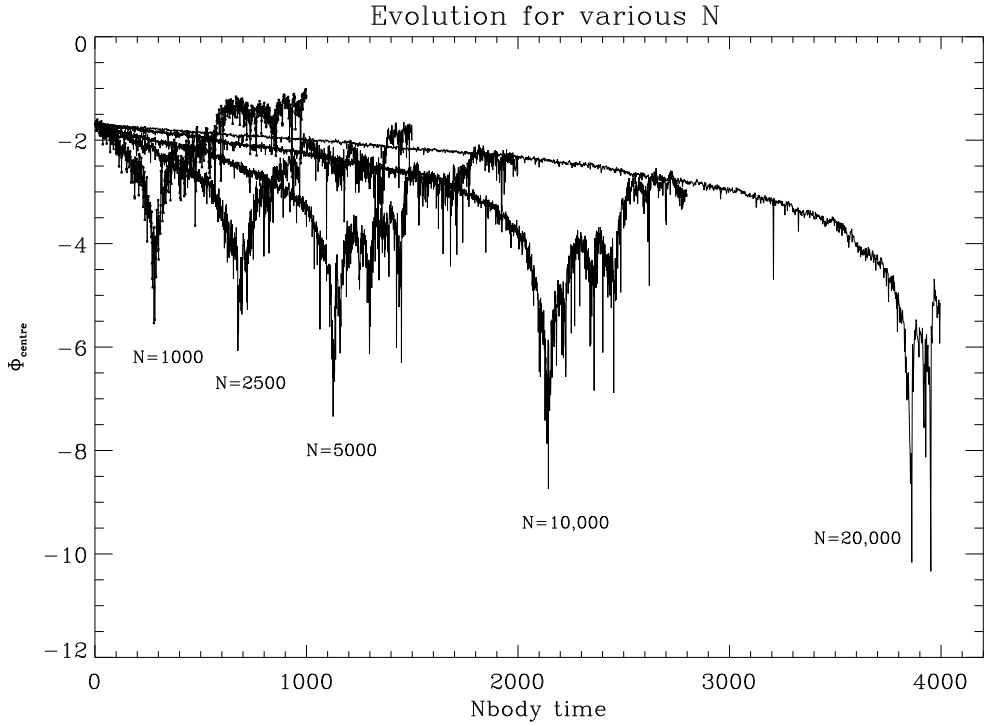

Figure 9.9: Evolution of the central potential of selected runs of Model A for $N = 1000$, 2500, 5000, 10, 000 and 20, 000 particles.

The assumed constancy of $N_{\rm c}$ leads to a second topic concerning the different amplitudes of the potential minima. This has already been mentioned in connection with Figure 9.3, though the left panel of Figure 9.10 points to the variations on N clearer. For models resembling the equal–mass case, the maximum depth is a function of N. The reason is that the collapse is only halted when the rate of energy production in the core becomes the same as the energy rate going in via the heat flux of the gravothermal instability (Goodman 1987). The outflowing energy is produced by the formation of binaries in three–body encounters, and the latter become important when the density is sufficiently high. As the core radius of a large–N cluster contains a larger number of stars initially, it has to get rid of almost all of them. Since the final $N_{\rm c}$ at core bounce is nearly a constant, the evolution of the core radius has to advance deeper in order to provide the density necessary for binary formation.

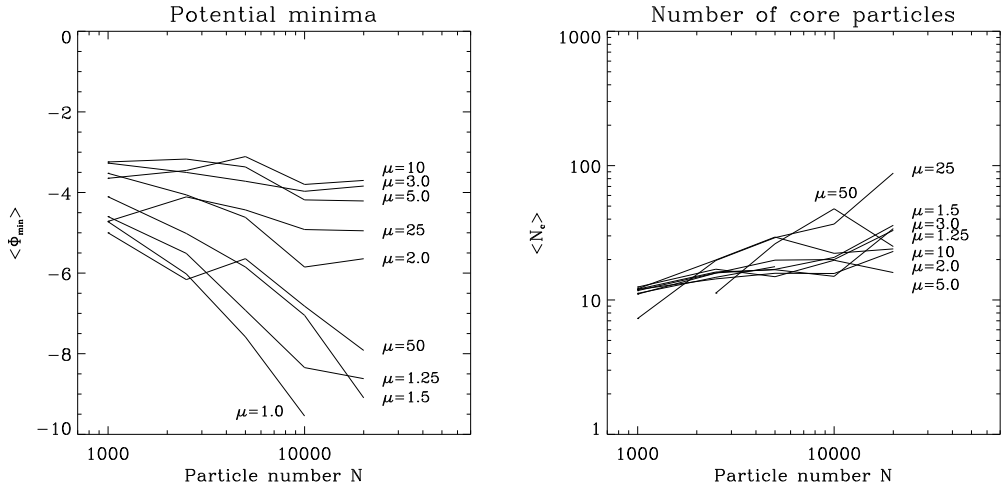

Figure 9.10: *Left*: The mean potential minima at the moment of core bounce as as function of the total particle number N. Models close to the equal–mass case show a deeper peak when N is rising than the high–μ models. Explanation is given in the text. *Right*: The mean core number increases only slightly with N. Disregarding the two highest μ, the number of minimum core particles is between 10 and 40.

Giersz & Heggie (1994b) described the same thing in terms of the fraction of core radius to half–mass radius, $r_\mathrm{c}/r_\mathrm{h}$: the larger N, the smaller that fraction. This is visible for models with μ close to unity in Figure 9.10. Though, the right panel suggests a slight increase of core particles for large–N models, the absolute values of N_c stay in the order between 10 and 40.

The situation looks somewhat different for models with high μ, in particular for μ = 25 and 50. The massive stars reach so fastly the centre that an "incomplete" evolution of the core occurs. The heavy masses collapse apart of any dynamical equilibrium, because the interactions among themselves are more important than those with the light stars. The central potential shows its deepest value when some few of them have gathered in the core, while the light stars have not changed their density distribution. The deeper potential is rather a matter of the presence of the massive stars than of a substantial collapse, and it appears not as profound as for nearly equal masses (see Figure 9.3 for comparison). Therefore, the amplitude of the collapse, $\langle\Phi_\mathrm{min}\rangle$, depends on N_c only weakly, if at all. — It should also be recalled that the data for $N = 20{,}0000$ are based on one single run for each μ, and their significance has to be taken with care: On one hand, the large N provides a number of 44 massive particles as a good basis for an analysis of the segregation process, on the other hand, one single run can just be considered as a trend, but its statistical value is low.

Now, we will focus on the coefficient γ in the Coulomb logarithm, $\ln(\gamma N)$. It has been subject of discussion several times, e.g. Giersz & Heggie (1994a) among others. Its value was estimated to be $\gamma = 0.11$ for a single–mass cluster, but the variations on μ are not known precisely. One way to determine this quantity is by comparing the evolution of the same model but for different N. We briefly repeat their method: The left panel of Figure 9.11 shows the ensemble–averaged Lagrangian radii of our Model A for two different N. For the time step t, the value of a Lagrangian radius in the 2500–body model was determined, and then the corresponding time t' at which the same value was reached in the 5000–body model. Because of the fluctuations, there are usually more than one such times, but choosing the first of them returns an appropriate result that is widely insensitive to other times. The ratio of these two times is a scale factor, S_f, that should be also equal to the ratio of the relaxation times for the different N:

$$\frac{t'}{t} = S_\mathrm{f} = \frac{N' \ln(\gamma N)}{N \ln(\gamma N')}. \tag{71}$$

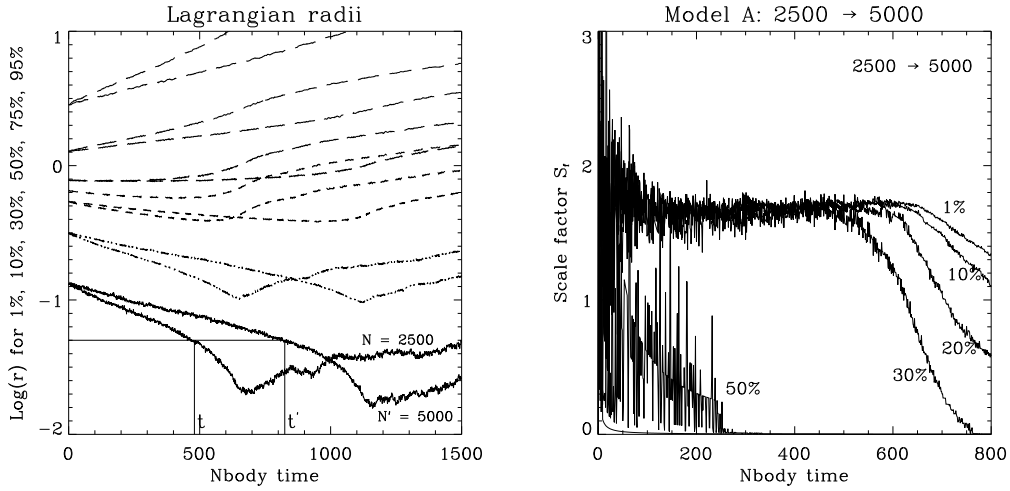

Figure 9.11: *Left*: Five selected Lagrangian radii of Model A for $N = 2500$ and $N' = 5000$. *Right*: Scale factor S_f for this model computed from the comparison of the Lagrangian radii.

Repeating this procedure for each time step and for each Lagrangian radius yields an S_f that is plotted in the right panel of Figure 9.11. Before the core collapse, the time ratios show a remarkable constancy (disregarding the initial settling period), and the inner Lagrangian radii agree very well. The other Langrangian radii (e.g. 50% radius) expand too early for a useful analysis. The scale factor in the constant pre–collapse range is $S_\mathrm{f} = 1.675$ for this model. With the definition $\nu = N'/N$, a re–arrangement of eq. (71) yields

$$\begin{aligned}
\frac{S_\mathrm{f}}{\nu}\ln(\gamma N') &= \ln(\gamma N) \\
\exp\left[\ln(\gamma N')^{S_\mathrm{f}/\nu}\right] &= \exp\left[\ln(\gamma N)\right] \\
\gamma^{S_\mathrm{f}/\nu}(N')^{S_\mathrm{f}/\nu} &= \gamma N \\
\gamma^{S_\mathrm{f}/\nu-1} &= \frac{N}{(N')^{S_\mathrm{f}/\nu}} \\
\gamma &= \left(\frac{N}{(N')^{S_\mathrm{f}/\nu}}\right)^{\frac{\nu}{S_\mathrm{f}-\nu}} . \qquad (72)
\end{aligned}$$

We computed the γ's for each model using the data sets of $N = 2500$ and $N' = 5000$. The results are given in Table 4 and plotted in Figure 9.12. The first two rows define the μ–model; the third gives the scale factor as determined from the figures analog to 9.11; the fourth is the error measured from the widths of the fluctuating lines in the stable regime (horizontal part); the fifth is the outer exponent in eq. (72) with $\nu = 2$; the sixth and the seventh row are the resulting γ's and their errors, respectively.

The comparison of the data sets "$2500 \to 5000$" provides a more accurate scale factor than the other data sets with lower N, because they rest upon a higher statistical significancy: Our set with $N = 10{,}000$ can be averaged over 4 runs only, and the 1000–set is biased to low–N physics. The results given in Table 4 show that γ actually varies too much for a meaningful interpretation. Very small variations in S_f cause large fluctuations in the two exponents of eq. (72) and alter γ enormously; the formula is "oversensitive" to both, S_f and ν. The error was computed as the difference of an "upper" and a "lower" γ that results from the thickness of the S_f–line. Systematic errors and biases

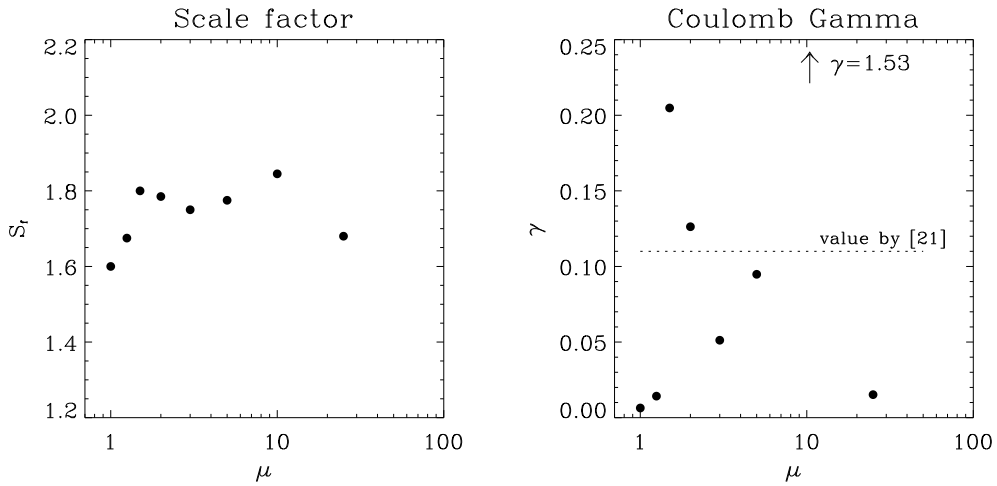

Figure 9.12: *Left*: Scale factors measured from figures analog to 9.11 for various μ. *Right*: Coulomb–γ as determined from N–body simulations with different particle numbers from eq. (72). The error bars are larger than the panel size.

Table 4: Scale factors and γ's for the models with different μ. The data were determined by comparing the data sets $N = 2500$ and $N' = 5000$, giving a particle ratio $\nu = 2$.

model	A	B	C	D	E	F	G
μ	1.25	1.5	2.0	3.0	5.0	10.0	25.0
S_f	1.675	1.800	1.785	1.750	1.775	1.845	1.680
ΔS_f	0.045	0.010	0.035	0.030	0.175	0.045	0.190
$\nu/(S_\mathrm{f} - \nu)$	-6.154	-10.00	-9.302	-8.000	-8.889	-12.903	-6.250
γ	**0.0142**	**0.2048**	**0.1263**	**0.0512**	**0.0948**	**1.5321**	**0.0152**
$\Delta\gamma$	0.0198	0.1477	0.3912	0.0808	—	—	—

in their estimation are very strong, but cannot be avoided. Therefore, the errors may give no more than an impression and recall the dangers of the interpretation.

As for different ν, we present another example illustrating the great variations when determining the Coulomb–γ. Table 5 shows the results for the equal–mass models using various particle numbers N and N'. The S_f shows a reasonable behaviour for different ν's and is conform to the result by Giersz & Heggie (1994a) shown in the last column. The resulting γ, however, differs at least by a factor of 5.

The value $\gamma = 0.11$ mentioned above is actually found due to the comparison of Nbody and Fokker–Planck simulations of equal–mass models (Giersz & Heggie 1994a, their figure 6). From their Nbody–Nbody simulations with particle numbers of $N = 500$ and $N' = 2000$ (their Figure 5), it is easy to extract an $S_\mathrm{f} = 2.95$ and get a $\gamma = 0.098$. For the same particle ratio, $\nu = 4.0$, we obtain a γ that is half of theirs (last two columns in Table 5). But, our absolute particle numbers are 5 times larger. From these discrepancies we just can conclude so far, that the choice of N and N' essentially contributes to the Coulomb–γ.

Finally, we are left with a fair range of possible values for the γ. They may be wrong by one order of magnitude; so does Model E for example when analyzing different $N \longrightarrow N'$ like in the Table 5. However, a crude estimate indicates that γ ranges somewhere between 0.01 and 0.20. A similar range was given by Giersz & Heggie (1996) for the case of a power–law mass spectrum: $0.016 \lesssim \gamma \lesssim 0.26$. Due to the uncertainties and dangers of interpretation, we cannot definitively judge whether a two–component system would really influence the Coulomb logarithm as much

Table 5: Comparison of our equal–mass models with four different particle numbers and the Nbody–analysis by Giersz & Heggie (1994a) in the last column.

Eq.Ms	$1000 \rightarrow 2500$	$1000 \rightarrow 5000$	$2500 \rightarrow 5000$	$2500 \rightarrow 10{,}000$	[21]
ν	2.5	5.0	2.0	4.0	4.0
$S_{\rm f}$	1.96	3.21	1.60	3.09	2.95
$\nu/(S_{\rm f}-\nu)$	-4.630	-2.793	-5.00	-4.396	-3.810
γ	0.028	0.018	0.006	0.044	0.098

as a continuous mass spectrum does. It is unclear how the fraction of heavy masses, q, could alter the results. A comparison of our two–mass models with analog Fokker–Planck simulations would provide a more reliable result. The rather constant scale factors, $S_{\rm f}$, for the majority of models give just a weak hint that the dependency of γ on μ could be marginally.

10 Extreme limits of segregation

The simulations of Series II discussed here are rather exotic ones. All the heavy masses m_2 were artificially placed at the two extreme parts:

- inside of the 10% Lagrangian radius, such that the two components would already be maximum segregated and no further process of stratification expected — those models will be called INS;
- and in the outside regions beyond the 90%–Lagrangian radius, in order to construct a most possible "anti–segregation" — these models are named OUT.

Though unrealistic, such extreme cases are of special interest for investigating the full range of the segregation process.

10.1 Motivation and setup

The idea for such a configuration goes back to the infrared observations of the young Trapezium cluster in the Orion Nebula Cloud by Hillenbrand & Hartmann (1998). They discovered a considerable amassing of heavy stars to the centre: The average mass within the core radius (0.205 pc) is three times larger than the average mass within 2 pc. Bonnell & Davies (1998) simulated young clusters between 500 and 1500 stars using the NBODY2 code and concluded from their results that the time scale for a dynamical mass segregation is much too long than is reflected by the positions and ages of the most massive stars in the Trapezium. Both papers argue for a primordial mass segregation.

The star formation theory by Murray & Lin (1996) also predicts a formation of the most massive stars near the cluster centre, since their proto–stellar clouds require many dissipative mergers with low–mass cloudlets for the growth. They happen, of course, in the dense regions. Such newly formed clusters will remain gravitationally bound with the massive stars remaining preferentially in the inner parts of the cluster. On the other side, Podsiadlowski & Price (1992) draw a scheme in which massive stars could also form in some cold gaseous clumps in the outskirts of a star–forming region. These individual massive stars sink to the centre (possibly while still forming), and are likely to affect the formation of other stars, for example by heating or disrupting their gas cloud. It is only the later phases of star formation that will be dominated by a sequential formation of massive stars surrounded by previously formed low–mass stars. However, the different results are conflicting.

We want to check the limits for mass segregation and core collapse in order to figure out the shortest and longest time scale for this process. As before, q is held fixed to 10% of the cluster's total mass, and the same μ–models are assumed as in the random particle distribution of Series I. The two populations, N_1 and N_2, consist of 2500 particles in total, and they are separately placed at the inner and outer regions. This is done by firstly selecting a distance r for one star from the formula which creates the Plummer profile

$$r = (M(r)^{-2/3} - 1)^{-1/2}, \tag{73}$$

where $M(r)$ is the accumulated mass of the bodies inside r; $M(r)$ is gained by iteration. So, the first star of mass $m_1 = (1 - m_2 N_2)/N_1$ has got a distance of $r = 0.074$ Nbody units. The actual position (x, y, z) is now computed by two random numbers that generate projections from the surface of that sphere with radius r (see Appendix of Aarseth, Hénon, Wielen 1974). This procedure places one body after the other along the mass function $M(r)$. The mean distance is predestined, the coordinates are optional. When placing all light bodies first, one gets the OUT–model, and vice versa the INS–model.

10.2 Mixture of the components

Figure 10.1 shows how the radial profile changes in the D–OUT simulation in an example run. Each panel is a snapshot of the momentary distribution of star numbers within a specified distance interval from the centre. The times are given in the upper right corner. Heavy stars are three times more massive and are marked as a shaded area, all of them placed far outside at the foothill of the Plummer profile at the start of the simulation. Those stars, whose velocity vector points accidentally inwards, are favoured for segregation and head for the centre as soon as a few crossing times but long before the collapse, anyway. The bulk of the other heavies widens and its members diffuse all over the space making up a more or less "flat" profile halfways to the collapse. Their strong tendency to the inner regions is visible. When their number in the inner shells has become sufficiently large (at $t \approx 250$), the collapse phase sets in. For this run, the collapse occurred at $t_{\rm cc} = 300.5$.

Now we turn to the contrary model, D–INS, presented in Figure 10.2. The heavy stars expand in all directions immediately from the start and form an own subsphere. This is because they are not in an energetic balance initially. Also, the light stars fall into the core and begin to mingle with the heavies from the very beginning. Relaxation between either components adjusts the energy distribution in the system. Both species try for the establishment of thermal and dynamical equilibrium. Whether it is achieved or not, depends on the mass ratio μ (this is discussed in more detail in the next chapter). These particles stay close to the potential well, and only a few of them succeed to reach out to the half–mass radius. While both species quickly mix and exchange their kinetic energies on the short relaxation time scale in the core, the gravothermal instability becomes effective and lets the core fall in. The collapse time proceeds by about 8% faster on average relative to the random setup. The difference between the INS– and the RND–results of Series I is not very large. Since the intermediate parts of the cluster do not exert an influence on the collapse, the initial expansion of the heavy stars does not have an effect, either. The collapse is only slightly faster.

Another comparison of the mixing process is shown for Model B ($\mu = 1.5$) in Figure 10.3. The mean mass between two Lagrangian radii is ensemble–averaged over 20 runs (see also Figure 9.5b for the corresponding RND simulation). In the right panel, the cluster starts from the INS–configuration: The 1%–Lagrangian shell has got a mean mass that is μ–times higher than the outer layers. The light stars penetrate immediately after the start into the innermost shell and reduce $\langle m \rangle$, as seen at the very left margin. The sphere of heavy bodies expands a little and raises the mean mass in the outer spheres (lower curves). After the short settling period of some few crossing times, the model turns into a configuration as in the RND–model. That is observed for any μ.

In the left panel of Figure 10.3, it is visible how slowly the heavy masses sink from the outskirts to the centre; the decreasing dashed line is the mean mass of the 75–95% shell. Its slow decline indicates that fair number of heavies remains in the halo for a long time before they start falling inwards. Their orbital velocity is also small, and their motion starts from a rather inert state. The collapse is performed a by those few heavy bodies that by chance moved quicker to the centre. As seen from the lower $\langle m \rangle$ in the innermost shell, the number of the heavies responsible for the collapse is smaller than in the INS– and RND–models.

Besides that, the stability of the shells in the post–collapse is remarkable: There is a fair balance in the amount of light and heavy masses far beyond the collapse. One might expect that all shells of the INS– and OUT–models would strive for the same level of $\langle m \rangle$, namely those of the analogous RND–model, within some relaxation times. Surprisingly, the different height of the levels indicate that evolution of the system has apparently slowed down after the collapse. However, it is not finished at all, for relaxation continues segregating the masses to the final state, which is given by the RND–model, indeed. The apparent stability is probably an effect which rests on the formation of binaries. In this phase, the energy production will be conducted into the core, while the outside regions expand. The expansion prohibits a subsequent infall. After very much later times, the shells reach the final $\langle m \rangle$–level of the RND–model when the mixture of the components has proceeded further.

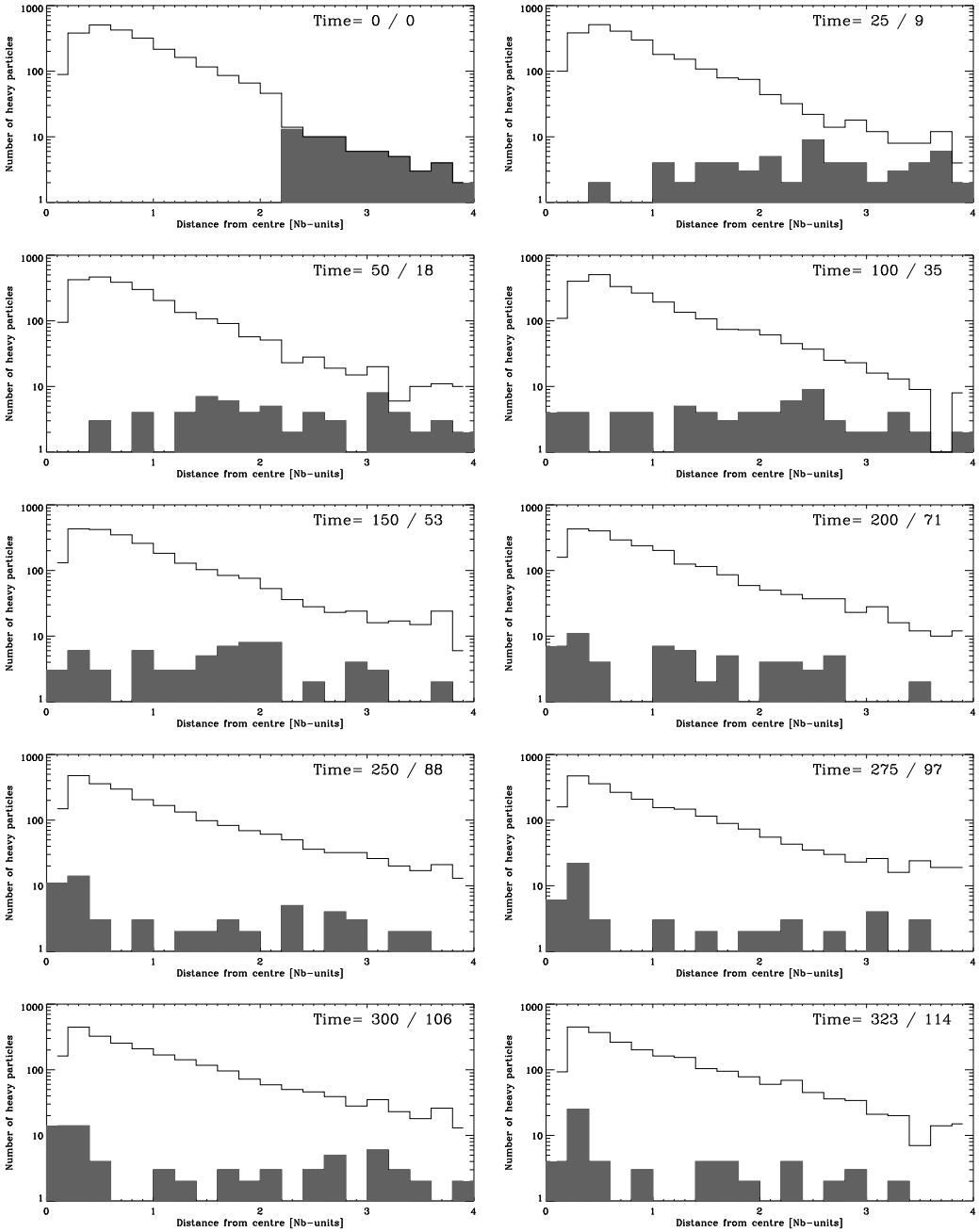

Figure 10.1: Model D–OUT, Run 19, with all heavy stars placed beyond the 90%–Lagrangian shell. Each panel shows a snapshot of the radial distribution of the heavy (shaded) and light stars. Their logarithmical number is plotted versus a distance intervall of bin width 0.2 in Nbody units of length (the half–mass radius is located at 0.766). The time is given in Nbody–units and in crossing times, respectively. The core collapse occured at time = 300.5 $t_{\rm NB}$ / 106.2 $t_{\rm cr}$.

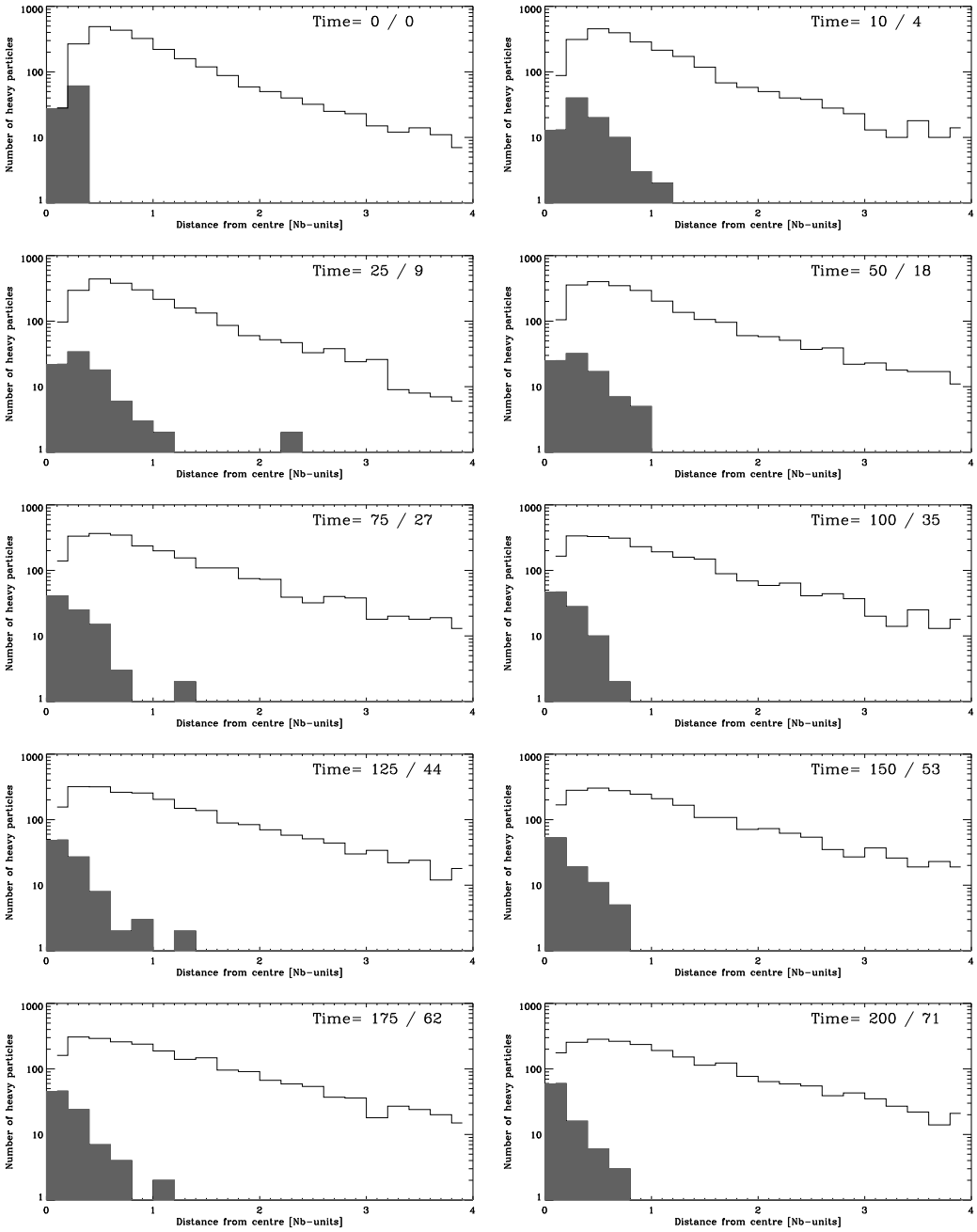

Figure 10.2: Model D–INS, Run 08, with all heavy stars (shaded) filling the 10%–Lagrangian shell completely; the light stars were placed thereafter. The axes and labels are the same as in Figure 10.1, but the snapshots were taken on different times. The core collapse occured at time = 124.0 $t_{\rm NB}$ / 43.8 $t_{\rm cr}$.

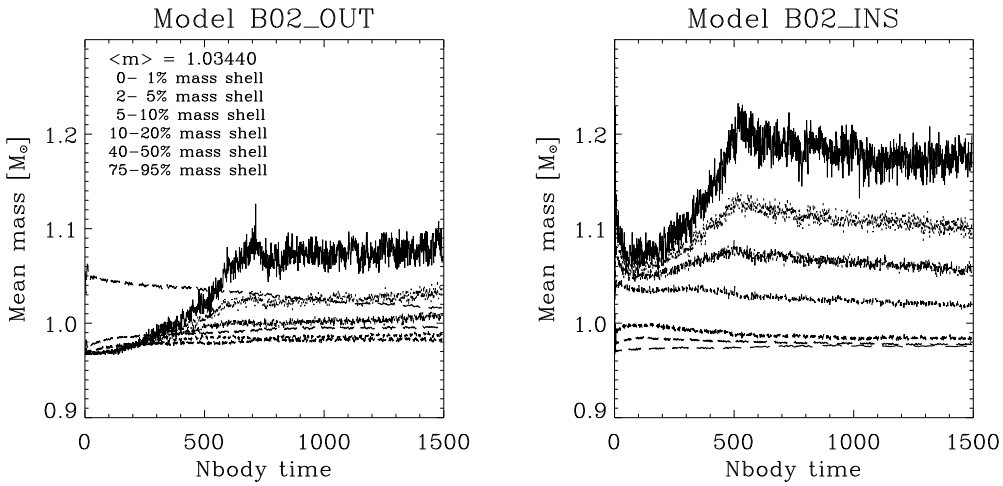

Figure 10.3: Comparison of the mean mass between Lagrangian radii for Models B–OUT (*left*) and B–INS (*right*). The data was averaged over an ensemble of 20 Runs; each run has $N = 2500$ particles.

10.3 The range of core collapse times

The core collapse times for the μ's with $N = 2500$ are summarized in Figure 10.4. The triangles indicate the values from the random setup of Series I (Fig. 9.4), and the dashed lines are the INS– and OUT–models discussed here. The error bars are also given, though they are again smaller than the symbols.

A remarkable feature is that the curved shape of the tube is present for all three configuration models (RND, INS, and OUT). We discuss the OUT–case first. The core collapse is delayed by a factor between 1.0 and 2.4 with respect to the random models. The heavy masses slowly start falling from their remote positions towards the centre. The flattening of the OUT–curve for high μ indicates that there is a minimum of time needed for the massive stars to spiral inwards. This minimum is plausibly taken to be the crossing time. In fact, taking into consideration that the crossing time is large in the halo ($t_{\rm cc} \approx$ 7–15 time units, depending on the actual distance), one heavy particle of Model H needs some 3–4 orbital revolutions to meet the other heavies and perform a collapse. The collapse is not so profound in terms of the core radius $r_{\rm c}$, as already discussed in connection with Figure 9.3. As an example for this scenario, the left panel of Figure 10.5 shows the shrinking orbits of the massive stars in Model H–OUT. It consists of 6 very heavy particles ($\mu = 50$), one of them is far outside at about 31 Nbody–radii and does not take part in the evolution. This run collapses at $t_{\rm cc} = 50$.

On the other side, the INS–models evolve faster than the RND–models by about 10–20%. The reason is that the density contrast between the core and the confining layers is built up quicker with respect to the RND–configuration. The heavy masses draw together, while the light ones enter and leave the core; the latter function efficiently as messengers that carry away the liberated heat from the core. In the RND–models, the heavy masses have to assemble first before the collapse sets in.

The flanking dashed lines in Figure 10.4 should not be considered as sharp borders, beyond which collapses would absolutely be impossible. Some few test simulations show that these boundaries can actually be crossed, if there is just very little "soiling" of the purely heavy–star region by a few light stars. These few light stars in the foreign field can cause a slight, but not significantly faster collapse. However, the dashed lines are an excellent approximation to the general limits of collapsing spheres, any tilted mass distribution should roughly fall between the given ranges.

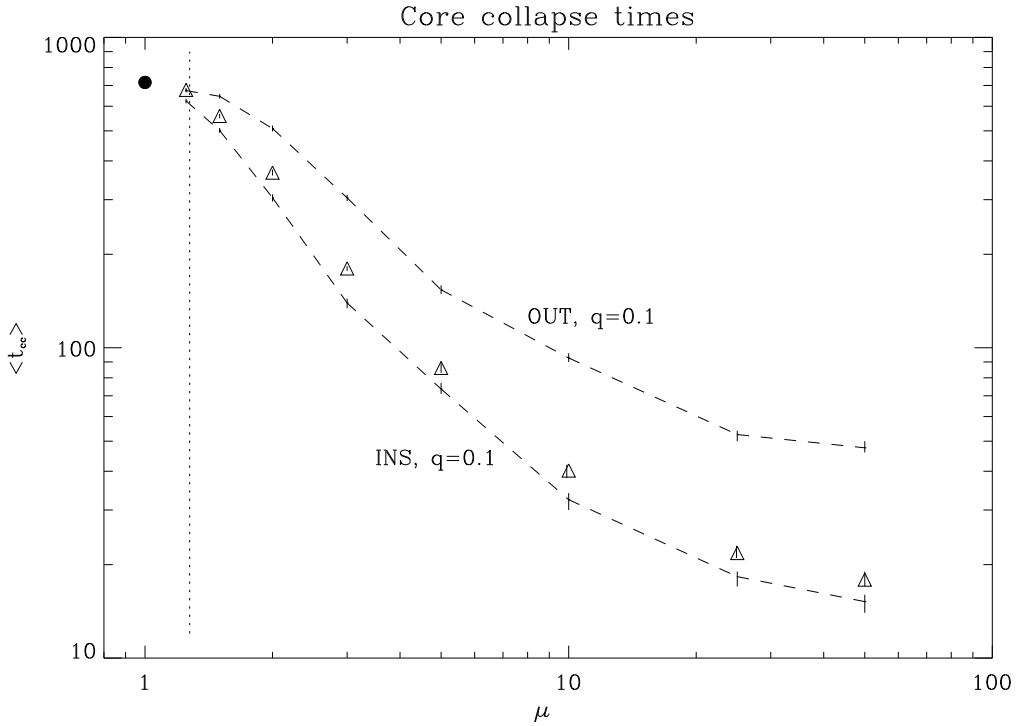

Figure 10.4: Core collapse times for models with $N = 2500$ of Series I (triangles) and II (dashed lines). The filled circle represents the value of the equal–mass system, and the dotted line is the Spitzer–instability border. The small error bars are also indicated.

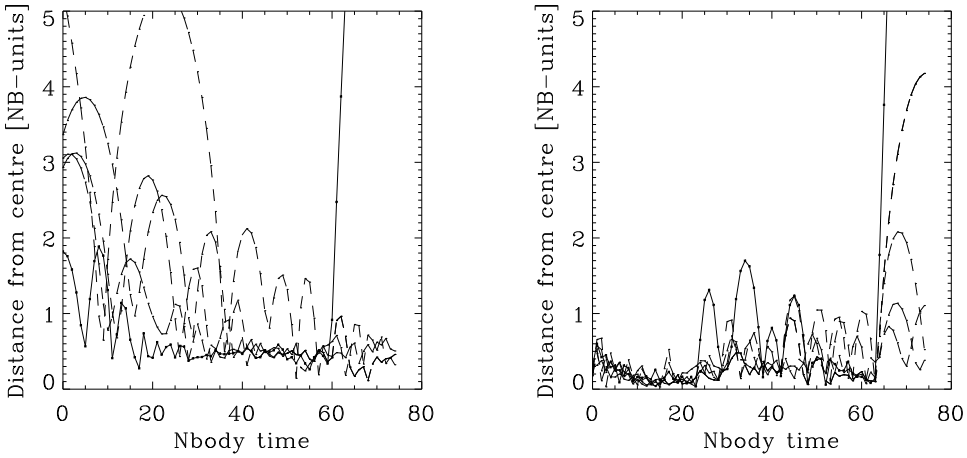

Figure 10.5: Similar to Figure 9.6. Distance moduli of 5 heavy–mass particles in Model H versus time. *Left*: Model H–OUT, Run 11, the core collapse occured at $t_{\rm cc} = 50.0$. *Right*: Model H–INS, Run 06, with a $t_{\rm cc} = 12.0$. The solid line highlights the orbit of an escaper.

10.4 Resume

The INS– and RND–models exhibit quite similar behaviour for their dynamical evolution. The core collapse is slightly faster if all heavy masses are initially placed close to the centre, but the speed up is rather low. Thus, we conclude that a newly formed cluster like the Orion Nebula Cloud (ONC), which has obviously a mass–segregated core, cannot be relaxed. This confirms the characteristics found by Hillenbrand & Hartmann (1998): The morphology of the core, i.e. the Trapezium area, supports a picture in which the structure is more likely a result of the initial conditions than the result of dynamical evolution. When including violent relaxation (Binney & Tremaine 1987), the massive stars could sink to the centre on the time scale of a single crossing time. The process, by which they lose kinetic energy to the less massive stars, becomes unnecessary (Bonnell & Davies 1998).

Of course, our highly idealized models are not intended to answer all questions on the segregation of a star–forming region, because a lot of factors remain neglected. For example: Simulations with a mass spectrum may reveal a faster evolution than the simple two–component model but also imply a more complicated treatment (Giersz & Heggie 1996); the total gravitational potential inside the ONC has a significant contribution from the molecular gas component that is usually thought to impede dynamical segregation (Hillenbrand & Hartmann 1998); stellar evolution, especially mass loss from rapidly evolving stars, is also a cause for different dynamics (Chernoff & Weinberg 1990); another question is connected to the formation of stars in clusters in general — it is known that only some 2% of the stars are really born in a gravitationally bound cluster, while the overwhelming majority is born in loose associations (Wielen 1971). In spite of the difficulties mentioned, we simulated the exceptional configurations of INS and OUT in this chapter in order to focus on the aspect whether pure dynamics is fast enough to disentangle masses to the observed stratification. The main property of these models is our analysis of the segregation time scales for different mass ratios μ for the first time. Figure 10.4 proves that any μ (even the largest at 50), does not provide a time scale short enough to explain the observations satisfactorily.

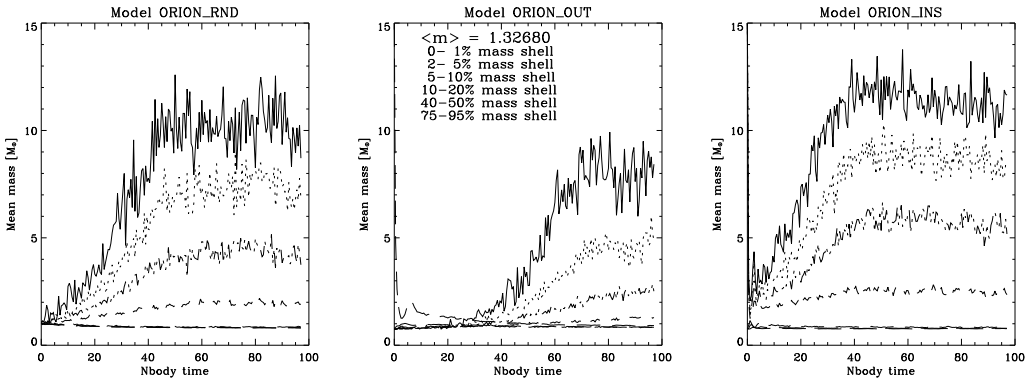

Figure 10.6: As in Figure 10.3. Mean mass in Lagrangian shells for a model with parameters $q = 0.26$, $\mu = 20.0$, and $N = 5000$. The data was ensemble–averaged from 10 runs with different random seed for the setup. *Left*: Model RND, positions of the heavy masses distributed at random across the Plummer sphere. The mean core collapse time is $\langle t_{\rm cc} \rangle = 49.6$. *Middle*: Model OUT, all heavy stars have been placed to the remote regions. The core collapse occured at $\langle t_{\rm cc} \rangle = 44.2$ on average. *Right*: Model INS, all heavies are filling the inner parts initially, $\langle t_{\rm cc} \rangle$ is at 12.0.

Our choice of $q = 0.1$ is to facilitate a comparison with the results of Series I, but less with the actual situation in the Trapezium. Nevertheless, a number of additional simulations have been made using the extreme ranges present in the star field of the ONC. With $q = 0.26$, $\mu = 20$, and $N = 5000$ taken from Hillenbrand & Hartmann (1998), we performed 10 runs for each of the distributions RND, INS, and OUT in order to test a two–component case with the parameters of the

Orion cluster. Figure 10.6 shows the mean mass between the Lagrangian radii similar to Figure 10.3. The basic features are the same as in the other models of that kind. The results of these simulations will be published in more detail elsewhere (Spurzem, Khalisi, Lin 2002).

11 Variations of the mass fraction q

So far, we have presented results on mass segregation for various μ. This chapter deals with three additional series, in which we altered the fraction of the heavy masses, q. Such kind of study has been discussed in detail by Inagaki & Wiyanto (1984) who simulated two–component clusters by means of Fokker–Planck modelling. They fixed μ to 2.0 and investigated the core collapse times as well as the achievement of equipartition. Figure 11.1 shows the evolution of the central potential in units of the half–mass relaxation time, $t_{\rm rh}$, for 4 different q's. The evolution is fastest when $q \approx 0.1$. Watters *et al.* (2000) repeated these simulations with a Monte Carlo code and added some more models at very low q's (see below).

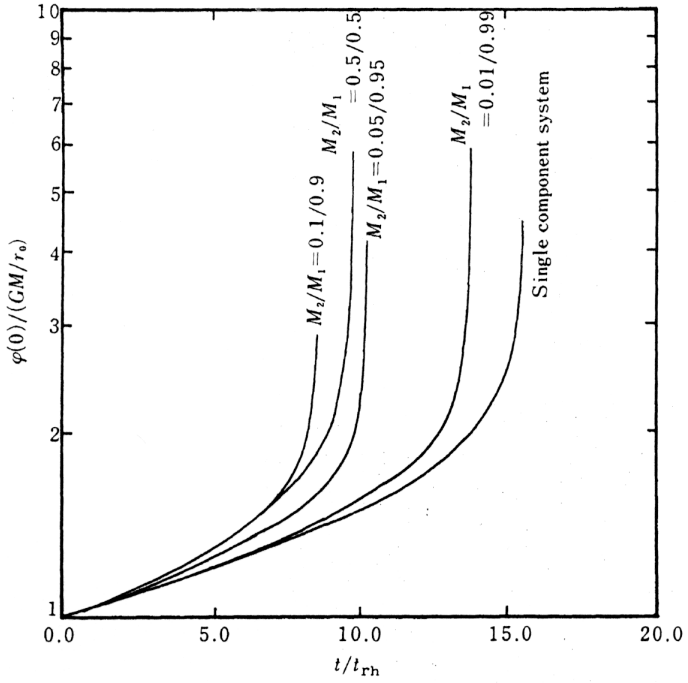

Figure 11.1: Time dependence of the central potential for q = 0.01, 0.05, 0.1, 0.5, and an equal–mass case (after Inagaki & Wiyanto 1984).

Our main aspect here is a comparison of the N–body data with the simulations mentioned, and also the question whether equipartition can be achieved between the two components while segregation is on work. We investigate the equipartition parameter

$$\xi = \frac{m_2\sigma_2^2}{m_1\sigma_1^2}, \tag{74}$$

which gives the ratio of the kinetic energies between the heavy and light stars in the core. At the start its value is about μ and heads for unity. When both mass species find a state of energy equipartition, $\xi = 1$ is reached, and we call the system "equipartition stable" as termed by Spitzer (1969; see also Chapter 6), otherwise a $\xi_{\rm min}$ indicates the closest approach to it.

In a particular run, the data of ξ is very noisy, especially, for small–N simulations. This fact aggravates the circumstances of analysis. In some cases, even the very rough mean does not immediately tend to equipartition, but staggers up and down before it meets (or even not) the value of 1. The main cause of these difficulties is the small number of particles inside the core radius, and it eventually becomes too small for a decent computation of the temperature ratio at late time steps.

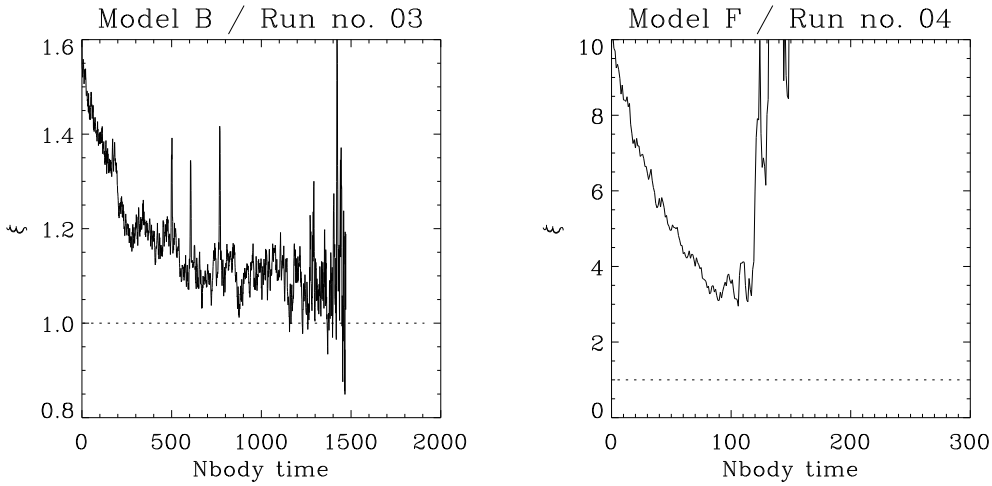

Figure 11.2: Equipartition parameter for two runs from model B (*left*) and F (*right*), respectively, containing 10,000 particles. The data was smoothed out with a smooth width $w = 5$ as described in Chapter 9.1.

For this reason, we decided to evaluate for the particles inside *twice* the core radius, and then apply the smoothing procedure of Section 9.1. We define $\xi_{\min} = 1$, if eq. (74) drops below unity at any time during the evolution; otherwise we set it to the deepest peak. Figure 11.2 shows an example for the parameter ξ from two models with $N = 10{,}000$. The B–model does reach equipartition at $t = 1157$, so $\xi_{\min}$ is set to 1; the F–model approaches to it up to $\xi_{\min} = 2.95$ at $t = 106$.

The average from all the runs' particular $\xi_{\min}$'s is denoted by $\langle \xi_{\min} \rangle$ and taken as the most reliable data for the model. Nevertheless, in some few cases, where $\xi_{\min}$ was not determinable at all because of the reasons above, the runs were excluded from averaging. The $\langle \xi_{\min} \rangle$'s are plotted versus μ in Figure 11.3. The symbols belong all to the Series I with $q = 0.1$, but a different particle number. The solid line connects the $N = 2500$ values (triangles). The additional Series III ($q = 0.05$), IV ($q = 0.2$), and V ($q = 0.4$) are shown as solid lines without a symbol. Error bars are given only for the four sets with $N = 2500$; they are smaller than the symbols in most cases.

As expected, the graphic shows that equipartition takes place for small μ's, but when μ becomes significantly greater than 2, $\langle \xi_{\min} \rangle$ recedes from unity. At $\mu = 2$, about half of the individual runs with $q = 0.1$ did succeed to reach $\xi_{\min} = 1$, at least for a moment. Those runs, which did not find a state of full equipartition, tried to reduce the kinetic difference halfways to the core collapse, but then departed shortly after the closest approach.

Table 6: Values of μ at which $\xi_{\min} > 1.05$. Equipartition cannot be attained anymore. See text.

Series	q	$\mu_{\rm crit}$	
III	0.05	2.49	
			2.032 ($N = 1000$)
			2.048 ($N = 2500$)
I	0.10	2.03	2.197 ($N = 5000$)
			2.111 ($N = 10$k)
			1.762 ($N = 20$k)
IV	0.20	1.87	
V	0.40	1.75	

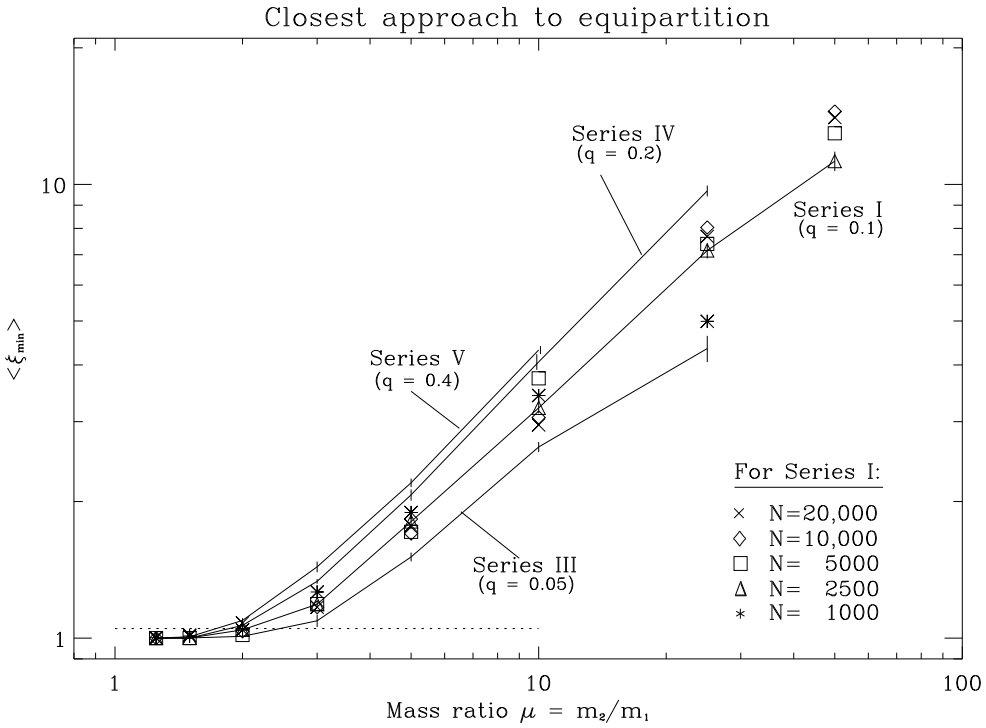

Figure 11.3: The averaged minimum of the equipartition parameter ξ for stars inside twice the core radius. When both mass components are in equipartition, $\xi_{\rm min}$ equals 1. The solid lines connect the data points for $q = 0.4$ (Series V), $q = 0.2$ (Series IV), $q = 0.1$ (Series I with triangles), and $q = 0.05$ (Series III). These four simulation series were made with $N = 2500$ particles, and error bars are given for them. The dotted line is an arbitrary threshold for equipartition stability at 1.05 as explained in the text.

That figure provides a good basis for the judgement on equipartition stability as theoretically introduced in Chapter 6. It is obvious that $\langle\xi_{\rm min}\rangle$ varies for different fractions of heavy masses, q: The less amount of heavy masses in a cluster, the closer equipartition is reached. This is consistent with the results by both Inagaki & Wiyanto (1984) and Watters *et al.* (2000). The latter explore an even wider range to very low q's down to 0.0015 (their set "B").

Now, it is desirable to find a "critical μ" at which equipartition stability is *not* given. This enables us to check the stability border. Instead of the orthodox requirement, that equipartition is to happen for $\langle\xi_{\rm min}\rangle = 1$ only, we will give a small tolerance and define the point of "turning away" from equipartition arbitrarily at $\langle\xi_{\rm min}\rangle = 1.05$, as Watters *et al.* (2000) did. It is denoted by the dotted horizontal line in Figure 11.3. By linear interpolation between the lower–next and upper–next data point, one obtains that this threshold is exceeded at the points $\mu_{\rm crit}$ given in Table 6.

The value for Series I was averaged from all simulation sets for different N. All $\langle\xi_{\rm min}\rangle$'s are plotted in the upper panel of Figure 11.4, and compared with the Monte Carlo results from Watters *et al.* (2000) below. The positions of our $\mu_{\rm crit}$ are marked by a small filled dot. The symbols have the same meaning as in the lower panel (see legend), and the lines are virtually the same as in Figure 8.1, but re–drawn in a dashed or in a solid style. The apparent difference for the line by Lightman & Fall (1978) is just an optical one: Watters *et al.* (2000) defined their fraction of heavy masses as $\hat{q} = M_2/M_1$, while this work uses $q = M_2/M_{\rm tot}$, see Chapter 8.2. For this reason, the axes have also been accommodated to the lower panel. Anyway, the graphics and the results are consistent with each other and ease the comparison.

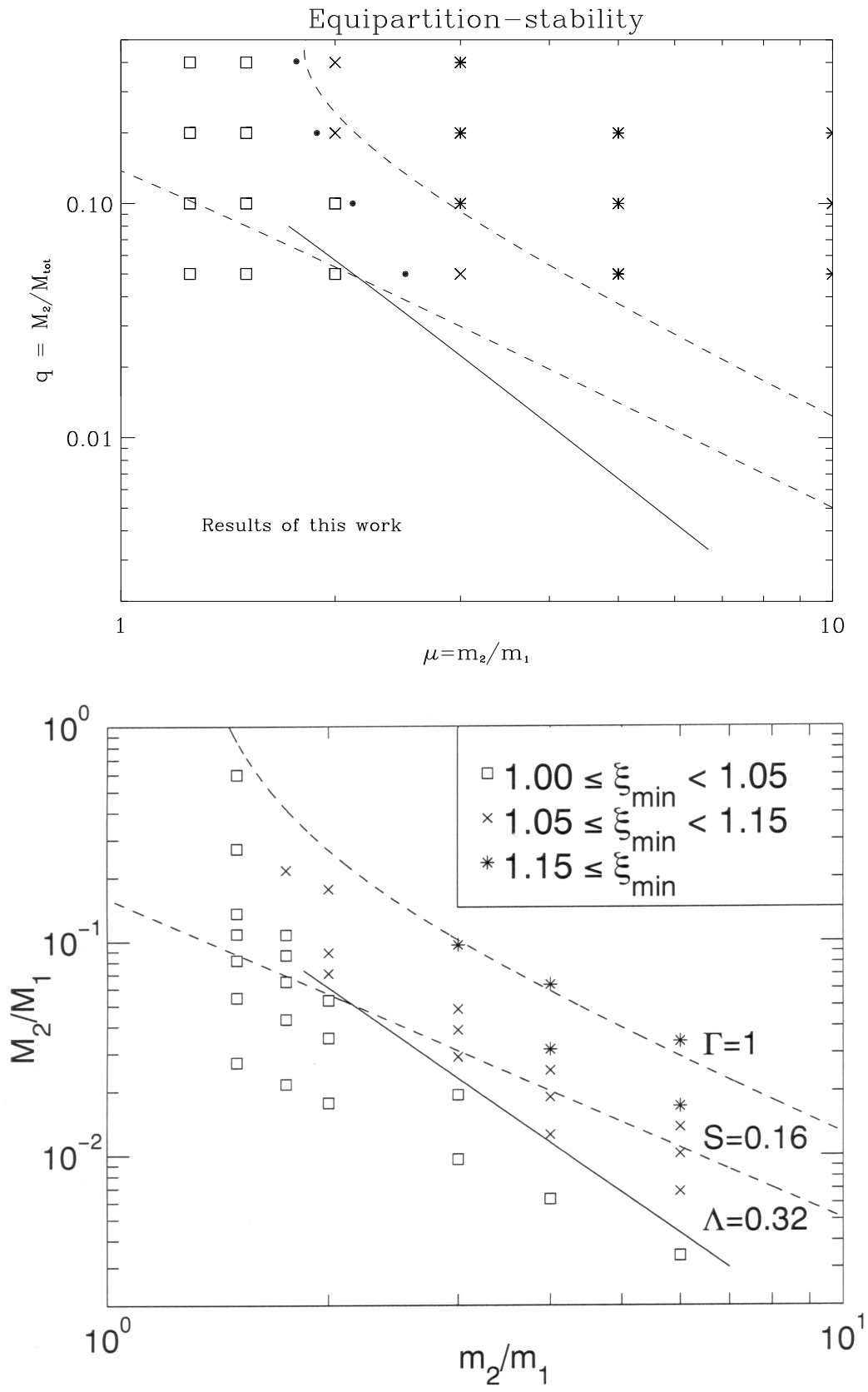

Figure 11.4: Closest approach to equipartition for the models in our parameter range (as in Figure 8.1). The lower panel repeats the results by Watters *et al.* (2000, their Fig. 6) for comparison. All symbols, axes, and lines are accommodated as explained in the text. The solid line is their stability criterion, eq. (41); the straight dashed line is from Spitzer (1969), eq. (30); and the curved dashed line is from Lightman & Fall (1978), eq. (36).

Although we have got just four points for $\mu_{\rm crit}$ in order to check the equipartition boundary, they follow the theoretical function by Lightman & Fall (1978) in fair agreement. The formula suggested by Watters *et al.* (2000) is cannot be ruled out, for it is based on models in a low–q regime, which is difficult to access with our Nbody simulations yet. However, our experimental data seem to show that Spitzer's (1969) criterion for the stability boundary, eq. (30), appears too strong, especially at mass ratios μ close to 1. This has also been found by similar studies.

Another fact concerns the fact that $\mu_{\rm crit} \approx 2$ is the point, which was already recognized as the transition of an equipartition–dominated and a gravothermal–dominated collapse (Ch.9.3). Below $\mu_{\rm crit}$, the core collapse proceeds slowlier than the theory proclaims, because equipartition governs the initial phase. When $\mu > \mu_{\rm crit}$, the gravothermal instability always wins the competition between the two effects: Before the thermal equilibrium can fully be settled, the massive stars have already segregated to the centre and collapse independently from the light stars. With the total fraction q being high, the massive component appears almost self–gravitating and is decoupled from the beginning.

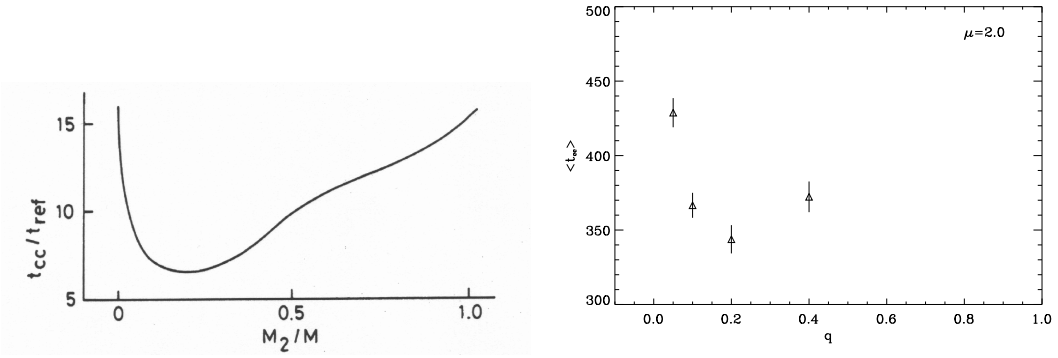

Figure 11.5: Core collapse time $t_{\rm cc}$ as a function of q. The individual mass ratio, μ, was fixed to 2.0. *Left*: Gas models by Bettwieser & Inagaki (1985) show a broad minimum for the core collapse times in terms of the relaxation time. The value of q for fastest evolution is $\approx$ 0.1–0.2. *Right*: Results of the Nbody models for the four series discussed here. The time on the vertical axis is given in Nbody units.

Bettwieser & Inagaki (1985) showed that there is an "optimal" q, that favours the collapse of a two–component system. If q is small, the collapse of the heavier component proceeds in the external field of the lighter stars, and the collapse time decreases rapidly. On the other hand, if q is very large, the amount of thermal energy contained in the core of the massive stars is so large that the core of the light ones cannot receive all the redundant energy. Hence the tendency to collapse is postponed, because the heat gained has to be dumped away into the halo and this process is slowlier than the tendency to equipartition. Finally, the extreme cases $q \to 0$ and $q \to 1$ approach the single–mass value for a negligible contribution of the heavy and light component, respectively. This is the reason why the core collapse time attains a minimum at a certain fraction of the heavier stars (Bettwieser & Inagaki 1985). The Nbody models confirm this, indeed (Figure 11.5).

12 Summary and outlook

We have studied mass segregation and equipartition in idealized star clusters containing two mass components. The results provide potential insight into the evolution of young star clusters, dynamics of star forming regions, and the degree of initial segregation which is needed to match the observations. Also, this study is of theoretical interest to check the classical ideas on equipartition and the thermodynamic behaviour of self–gravitating systems.

The models presented here are to isolate the relevant physical processes. Therefore, we neglected stellar evolution, primordial binaries, and a tidal field. Point masses are used for the numerical simulations, which only have two different mass species as the most simple approximation of a realistic mass spectrum. The parameter space was widely analysed for both parameters: the ratio of individual star masses, $\mu = m_2/m_1$, that was varied from 1.25 to 50; and the fraction of the total heavy masses, $q = M_2/M_{\rm tot}$, that was chosen to be 0.05, 0.1, 0.2, or 0.4. We also directed our attention to the value $q = 0.1$, which was claimed by Inagaki & Wiyanto (1984) to exhibit the fastest evolution time. For this fraction, we modelled different particle numbers, with N ranging from 1000 to $20,\,000$. For all other cases we used a particle number of $N = 2500$. The statistical significancy of the data was considerably improved by ensemble–averages: A large number of physically equivalent runs differing just by a random seed for an initial setup was performed, and the data base was gathered for an overall average.

For the first time we have empirically checked the borders between an equipartition stable and unstable configuration as given by Spitzer (1969) with the accurate direct N–body method. His criterion involves the parameters q and μ and is given in eq. (30). We also tested other theories differing in the assumptions and find that the basic processes differ only by a relatively small amount when predicting the approach to equipartition. Moreover, we determined the ranges of the longest and shortest core collapse time by comparing different initial setups of the particles: On one hand, the pre–segregated state with all the heavy masses being already in the inner regions of the cluster, and, on the other hand, the anti–segregated models with the heavies having the longest way to sink to the centre.

From the results of our simulations we draw the following conclusions on the global cluster evolution:

1. The evolution of a self–gravitating system with two mass–components depends strongly on the ratio of the individual masses, $\mu = m_2/m_1$. When μ is larger than ≈ 2, the heavy masses fall to the centre and reduce the relaxation time proportional to $1/\mu$. Subsidiary, the core collapse time is shortened in the same way (Fig. 9.4). Smaller μ's go into equipartition which slows down the evolution. Extraordinary large μ's give rise to a small number of heavy particles, and the situation turns into a process of dynamical friction.

2. There is a competition between equipartition of energies and gravothermal instability. If μ is close to unity, equipartition hinders the gravothermal collapse in the initial phase, but will never prevent it. As the heavy stars congregate in the centre regions, they decouple from the light component and perform their own collapse. When μ exceeds a critical value of about 2, equipartition can never be achieved (Fig. 11.3).

3. The boundary between the stable and unstable regimes is close to the theory by Lightman & Fall (1978) when q is $\gtrsim 0.2$. For q lower than ≈ 0.1, all other theories on equipartition (Ch. 6) seem to show a better agreement, but it is difficult to assess that range with N–body simulations because the absolute number of very heavy particles is too low in our standard N (Fig. 11.4). When q becomes larger than 0.1, Spitzer's (1969) criterion appears too strong, and his theory fails: According to eq. (30) no equipartition should be possible at all, while our models as well as the Monte Carlo simulations by Watters *et al.* (2000) show the contrary. The cause is probably that Spitzer assumed a *global* equilibrium when deriving the analytical

formulae. His basic ideas on the processes, however, are still in fair accordance with our results.

4. Segregation proceeds on the relaxation time scale simultaneously with the evolution of the cluster. The maximum level of segregation is attained when the core has collapsed and begins to expand. Then, the mass shells in the cluster have also adjusted to a stable balance of an in–going and outgoing mass flux (Fig.9.5). After the core collapse, the degree of stratification remains constant.

5. In the extreme ranges of segregation, we find that the core collapse times are too long in either cases, the pre– and anti–segregation, to explain the observed mass stratification in young star forming regions dynamically (Fig. 10.4). It is likely that a primordial segregation of the gas cloud occurs before the first heavy stars form in the centre. The adoption of a realistic mass spectrum may accelerate the segregation time even more and would reveal new insights, though.

6. The escape rate shows two branches along the μ–axis indicating two different mechanisms being on work (Fig. 9.8e). For mass ratios resembling the equal–mass case, the escape seems to be governed by evaporational effects in the pre–collapse phase. Since the core collapse time decreases for a moderately rising μ, evaporation does not advance far, such that the mass loss is also reduced. For high μ's (> 3), we believe that escapes are rather a matter of ejections; the very massive particles distribute their kinetic energy to a large number of stars, and the escape rate increases roughly with μ. The details of these processes, however, need more analysis tracing the path of the escapers or a countercheck with other simulation methods. As for the equal–mass case, the escape rate is about 0.25 and consistent with other N–body simulations (Wielen 1975, Giersz & Heggie 1994a, Baumgardt *et al.* 2002).

7. Light masses play an important role in the heat transfer from the core to the halo. Even a small fraction of them moderates the heat flux between the central source and the outer sink. The "optimal" fraction q of heavy to light stars is about 0.15–0.20 in accord with previous results from gaseous models (Fig. 11.5).

Our results gained with the N–body method confirm previous simulations with other techniques (gas models, Monte Carlo), but also reveal hidden effects like the small "deceleration" of the gravothermal collapse due to equipartition. Further astrophysical assumptions are likely to alter the results, e.g. the introduction of primordial binaries in various fractions, a tidal field that accelerates the collapse as well as the dissolution of clusters, or rotation. Multiple mass components or a continuous spectrum make the analysis more complex but are important for the understanding of the observations. Our variation of μ can principally be generalized by merging into a multi–mass model, but care has to be taken when defining the parameters. The new parameters appearing for the models are to be checked, e.g. the slope of the initial mass function (if a power–law is assumed), and how the ratio of the highest mass to the mean mass, $m_{\max}/\langle m \rangle$, influences the segregation.

Another subject is the long–term evolution facing gravothermal oscillations (as in Figure 2.2). So far, this has been analysed and simulated for single–mass systems only. Questions are related to the oscillation period, its amplitude, and the minimum particle number for obtaining the oscillations when at least a second mass is present.

Practical applications of such two–components studies can be imagined for any kind of modelling where gravitation plays a significant role. Examples may be the strata of the upper atmosphere; merging of chemical alloys under weightlessness in space missions; nuclear and plasma physics; coagulation of rocky–sized asteroids to form planetesimals and protoplanets; collisions of galaxies with different masses. Finally, demands on large–particle computation also drive the technical developments to new limits such that theories can be verified (not even not) by simulations as an alternative to common observations.

Appendix: Data tables

The following tables contain the mean values of the simulations of star clusters and are organised as follows. The title specifies the Series, q, and particle number.
Column 1: model name and μ
Column 2: $\langle t_{\rm cc} \rangle$, mean core collapse time
Column 3: $\langle \Phi_{\rm min} \rangle$, depth of central potential
Column 4: $\langle r_{\rm c} \rangle$, mean core radius in the moment of core bounce
Column 5: $\langle N_{\rm c} \rangle$, number of particles in the core at the time of smallest core radius
Column 6: $\langle \xi_{\rm min} \rangle$, mean of the closest approach to equipartition
Column 7: $\langle N_{\rm esc} \rangle$, number of escaped stars until core collapse time
Column 8: $\langle E_{\rm esc} \rangle$, mean energy of escapers

Equal–mass: N = 1000

model	$\langle t_{\rm cc} \rangle$	$\langle \Phi_{\rm min} \rangle$	$\langle r_{\rm c} \rangle$	$\langle N_{\rm c} \rangle$	$\langle \xi_{\rm min} \rangle$	$\langle N_{\rm esc} \rangle$	$\langle E_{\rm esc} \rangle$
EQMASS01	**345.8** ±5.2	−**4.72** ±0.10	**0.0208** ±0.0020	**11.2** ±0.4	—	**26.6** ±1.1	**0.88** ±0.18

Equal–mass: N = 2500

model	$\langle t_{\rm cc} \rangle$	$\langle \Phi_{\rm min} \rangle$	$\langle r_{\rm c} \rangle$	$\langle N_{\rm c} \rangle$	$\langle \xi_{\rm min} \rangle$	$\langle N_{\rm esc} \rangle$	$\langle E_{\rm esc} \rangle$
EQMASS02	**716.0** ±12.0	−**6.02** ±0.16	**0.0086** ±0.0006	**14.8** ±0.8	—	**64.2** ±3.1	**0.89** ±0.24

Equal–mass: N = 5000

model	$\langle t_{\rm cc} \rangle$	$\langle \Phi_{\rm min} \rangle$	$\langle r_{\rm c} \rangle$	$\langle N_{\rm c} \rangle$	$\langle \xi_{\rm min} \rangle$	$\langle N_{\rm esc} \rangle$	$\langle E_{\rm esc} \rangle$
EQMASS05	**1210.2** ±10.6	−**7.58** ±0.27	**0.0045** ±0.0003	**17.7** ±0.8	—	**117.1** ±5.0	**0.71** ±0.26

Equal–mass: N = 10,000

model	$\langle t_{\rm cc} \rangle$	$\langle \Phi_{\rm min} \rangle$	$\langle r_{\rm c} \rangle$	$\langle N_{\rm c} \rangle$	$\langle \xi_{\rm min} \rangle$	$\langle N_{\rm esc} \rangle$	$\langle E_{\rm esc} \rangle$
EQMASS10	**2312.9** ±34.7	−**8.75** ±0.47	**0.0025** ±0.0004	**21.3** ±2.2	—	**256.3** ±7.1	**2.55** ±1.43

Series I: q = 0.1, N = 1000

model (μ)	$\langle t_{\rm cc} \rangle$	$\langle \Phi_{\rm min} \rangle$	$\langle r_{\rm c} \rangle$	$\langle N_{\rm c} \rangle$	$\langle \xi_{\rm min} \rangle$	$\langle N_{\rm esc} \rangle$	$\langle E_{\rm esc} \rangle$
A (1.25)	**309.1** ±5.8	−**4.60** ±0.11	**0.0206** ±0.0009	**11.1** ±0.4	**1.002** ±0.002	**22.9** ±1.2	**0.70** ±0.17
B (1.5)	**256.0** ±5.1	−**4.10** ±0.07	**0.0275** ±0.0011	**11.7** ±0.3	**1.011** ±0.005	**18.4** ±1.1	**0.70** ±0.11
C (2.0)	**162.6** ±3.5	−**3.52** ±0.04	**0.0400** ±0.0016	**12.0** ±0.5	**1.043** ±0.010	**9.5** ±0.5	**0.78** ±0.24
D (3.0)	**86.1** ±2.1	−**3.27** ±0.06	**0.0596** ±0.0026	**12.0** ±0.6	**1.264** ±0.033	**4.8** ±0.4	**1.02** ±0.26
E (5.0)	**45.8** ±1.4	−**3.24** ±0.06	**0.0797** ±0.0040	**12.5** ±0.8	**1.892** ±0.071	**0.0** ±0.0	**0.00** ±0.00
F (10.0)	**25.4** ±0.9	−**3.65** ±0.08	**0.0954** ±0.0039	**12.1** ±0.7	**3.426** ±0.187	**4.1** ±0.4	**1.28** ±0.33
G (25.0)	**18.0** ±0.7	−**4.72** ±0.12	**0.0785** ±0.0030	**7.3** ±0.4	**4.992** ±0.237	**12.9** ±0.2	**1.09** ±0.12

Series I: q **= 0.1,** N **= 2500**

model (μ)	$\langle t_{\rm cc}\rangle$	$\langle\Phi_{\rm min}\rangle$	$\langle r_{\rm c}\rangle$	$\langle N_{\rm c}\rangle$	$\langle\xi_{\rm min}\rangle$	$\langle N_{\rm esc}\rangle$	$\langle E_{\rm esc}\rangle$
A (1.25)	**677.8** ±8.1	−**5.51** ±0.12	**0.0100** ±0.0005	**15.9** ±0.7	**1.000** ±0.000	**61.3** ±2.0	**0.77** ±0.27
B (1.5)	**558.4** ±8.8	−**5.02** ±0.11	**0.0137** ±0.0006	**15.9** ±0.8	**1.001** ±0.000	**45.2** ±2.2	**0.55** ±0.14
C (2.0)	**366.6** ±8.4	−**4.06** ±0.11	**0.0207** ±0.0011	**14.4** ±1.0	**1.043** ±0.028	**24.9** ±1.6	**1.18** ±0.28
D (3.0)	**180.1** ±2.9	−**3.50** ±0.10	**0.0336** ±0.0019	**16.2** ±2.3	**1.188** ±0.017	**9.7** ±0.6	**0.70** ±0.12
E (5.0)	**86.1** ±3.3	−**3.17** ±0.10	**0.0567** ±0.0043	**17.0** ±1.4	**1.807** ±0.056	**7.3** ±0.8	**1.43** ±0.27
F (10.0)	**40.2** ±2.0	−**3.45** ±0.15	**0.0811** ±0.0054	**19.9** ±1.8	**3.218** ±0.086	**8.0** ±0.7	**0.89** ±0.12
G (25.0)	**21.8** ±1.1	−**4.11** ±0.18	**0.0905** ±0.0048	**19.7** ±1.7	**7.150** ±0.282	**12.4** ±0.9	**0.86** ±0.15
H (50.0)	**17.9** ±1.1	−**6.16** ±0.36	**0.0792** ±0.0039	**11.7** ±1.0	**11.245** ±0.556	**25.2** ±2.6	**0.98** ±0.15

Series I: q **= 0.1,** N **= 5000**

model (μ)	$\langle t_{\rm cc}\rangle$	$\langle\Phi_{\rm min}\rangle$	$\langle r_{\rm c}\rangle$	$\langle N_{\rm c}\rangle$	$\langle\xi_{\rm min}\rangle$	$\langle N_{\rm esc}\rangle$	$\langle E_{\rm esc}\rangle$
A (1.25)	**1183.7** ±17.7	−**6.92** ±0.18	**0.0055** ±0.0004	**19.8** ±0.7	**1.000** ±0.000	**103.9** ±5.0	**0.44** ±0.13
B (1.5)	**993.8** ±10.3	−**5.85** ±0.12	**0.0071** ±0.0003	**16.9** ±1.0	**1.000** ±0.000	**76.9** ±3.2	**0.57** ±0.14
C (2.0)	**642.6** ± 4.4	−**4.62** ±0.20	**0.0117** ±0.0011	**15.8** ±1.4	**1.016** ±0.008	**38.0** ±1.9	**0.47** ±0.09
D (3.0)	**331.5** ±11.6	−**3.72** ±0.08	**0.0204** ±0.0013	**16.8** ±1.4	**1.189** ±0.037	**19.3** ±2.6	**1.08** ±0.45
E (5.0)	**157.9** ± 6.3	−**3.36** ±0.12	**0.0302** ±0.0025	**14.9** ±1.1	**1.715** ±0.039	**14.2** ±1.9	**1.38** ±0.27
F (10.0)	**64.3** ± 3.5	−**3.11** ±0.09	**0.0742** ±0.0055	**29.4** ±2.8	**3.738** ±0.256	**10.4** ±1.0	**2.17** ±1.01
G (25.0)	**33.3** ± 0.9	−**4.43** ±0.34	**0.0842** ±0.0025	**29.1** ±1.4	**7.394** ±0.214	**17.7** ±1.2	**0.97** ±0.09
H (50.0)	**22.4** ± 0.7	−**5.64** ±0.43	**0.0789** ±0.0089	**26.2** ±3.5	**12.962** ±0.358	**25.8** ±3.1	**1.15** ±0.18

Series I: q **= 0.1,** N **= 10,000**

model (μ)	$\langle t_{\rm cc}\rangle$	$\langle\Phi_{\rm min}\rangle$	$\langle r_{\rm c}\rangle$	$\langle N_{\rm c}\rangle$	$\langle\xi_{\rm min}\rangle$	$\langle N_{\rm esc}\rangle$	$\langle E_{\rm esc}\rangle$
A (1.25)	**2169.9** ±24.7	−**8.35** ±0.52	**0.0027** ±0.0003	**20.0** ±2.7	**1.000** ±0.000	**227.3** ±3.9	**0.40** ±0.11
B (1.5)	**1886.8** ± 8.6	−**7.05** ±0.39	**0.0042** ±0.0001	**20.8** ±1.0	**1.008** ±0.006	**172.3** ±9.3	**0.35** ±0.06
C (2.0)	**1218.0** ±20.1	−**5.85** ±0.37	**0.0053** ±0.0007	**15.8** ±1.8	**1.035** ±0.014	**91.3** ±4.3	**0.78** ±0.17
D (3.0)	**595.1** ± 8.5	−**3.97** ±0.17	**0.0107** ±0.0010	**15.0** ±1.9	**1.170** ±0.024	**35.3** ±3.4	**1.03** ±0.27
E (5.0)	**277.6** ± 9.7	−**4.18** ±0.32	**0.0235** ±0.0004	**19.8** ±1.4	**1.700** ±0.029	**19.3** ±1.4	**0.63** ±0.08
F (10.0)	**123.5** ± 2.1	−**3.80** ±0.31	**0.0351** ±0.0055	**22.3** ±3.9	**3.065** ±0.108	**25.5** ±2.0	**1.19** ±0.04
G (25.0)	**52.4** ± 2.3	−**4.92** ±0.42	**0.0741** ±0.0108	**36.8** ±6.1	**8.040** ±0.440	**29.0** ±2.9	**2.05** ±0.82
H (50.0)	**37.5** ± 0.6	−**6.82** ±0.95	**0.0894** ±0.0059	**47.8** ±8.9	**14.478** ±0.859	**42.3** ±5.3	**0.93** ±0.28

Series I: q **= 0.1,** N **= 20,000**

model (μ)	$\langle t_{\rm cc}\rangle$	$\langle\Phi_{\rm min}\rangle$	$\langle r_{\rm c}\rangle$	$\langle N_{\rm c}\rangle$	$\langle\xi_{\rm min}\rangle$	$\langle N_{\rm esc}\rangle$	$\langle E_{\rm esc}\rangle$
A (1.25)	**3859.0** ±00.0	−**8.62** ±0.00	**0.0021** ±0.0000	**33.0** ±0.0	**1.000** ±0.000	**422.0** ±0.0	**0.52** ±0.00
B (1.5)	**3318.0** ± 0.0	−**9.09** ±0.00	**0.0030** ±0.0000	**36.0** ±0.0	**1.016** ±0.000	**292.0** ±0.0	**0.79** ±0.00
C (2.0)	**2236.0** ± 0.0	−**5.64** ±0.00	**0.0044** ±0.0000	**23.0** ±0.0	**1.081** ±0.000	**140.0** ±0.0	**0.34** ±0.00
D (3.0)	**1094.0** ± 0.0	−**3.84** ±0.00	**0.0114** ±0.0000	**34.0** ±0.0	**1.170** ±0.000	**55.0** ±0.0	**0.56** ±0.00
E (5.0)	**608.0** ± 0.0	−**4.21** ±0.00	**0.0103** ±0.0000	**16.0** ±0.0	**1.770** ±0.000	**65.0** ±0.0	**2.82** ±0.00
F (10.0)	**213.0** ± 0.0	−**3.70** ±0.00	**0.0241** ±0.0000	**24.0** ±0.0	**2.950** ±0.000	**38.0** ±0.0	**1.34** ±0.00
G (25.0)	**78.0** ± 0.0	−**4.95** ±0.00	**0.0863** ±0.0000	**88.0** ±0.0	**7.680** ±0.000	**30.0** ±0.0	**1.41** ±0.00
H (50.0)	**48.5** ± 0.0	−**7.92** ±0.00	**0.0447** ±0.0000	**25.0** ±0.0	**14.046** ±0.000	**48.0** ±0.0	**0.78** ±0.00

Series II: q **= 0.1,** N **= 2500, INS**

model (μ)	$\langle t_{\rm cc}\rangle$	$\langle\Phi_{\rm min}\rangle$	$\langle r_{\rm c}\rangle$	$\langle N_{\rm c}\rangle$	$\langle\xi_{\rm min}\rangle$	$\langle N_{\rm esc}\rangle$	$\langle E_{\rm esc}\rangle$
A (1.25)	**623.9** ±11.1	−**5.64** ±0.10	**0.0098** ±0.0005	**15.2** ±0.5	—	**57.5** ±2.8	**0.89** ±0.22
B (1.5)	**501.5** ± 9.1	−**5.05** ±0.10	**0.0133** ±0.0008	**14.4** ±0.8	—	**42.0** ±2.5	**1.30** ±0.56
C (2.0)	**304.4** ± 8.0	−**4.09** ±0.12	**0.0225** ±0.0018	**15.2** ±1.0	—	**16.9** ±1.1	**0.35** ±0.18
D (3.0)	**139.4** ± 4.6	−**3.51** ±0.07	**0.0330** ±0.0023	**13.5** ±0.9	—	**8.5** ±0.9	**0.15** ±0.11
E (5.0)	**73.6** ± 3.0	−**3.51** ±0.08	**0.0437** ±0.0026	**12.3** ±0.8	—	**8.4** ±0.8	**1.43** ±0.40
F (10.0)	**32.4** ± 1.7	−**3.58** ±0.13	**0.0722** ±0.0059	**16.3** ±1.9	—	**5.9** ±0.8	**1.01** ±0.29
G (25.0)	**18.3** ± 0.9	−**5.28** ±0.33	**0.0845** ±0.0070	**16.3** ±2.9	—	**13.6** ±1.5	**0.78** ±0.11
H (50.0)	**15.2** ± 0.9	−**5.52** ±0.27	**0.0892** ±0.0050	**13.9** ±1.4	—	**25.7** ±2.2	**0.82** ±0.10

Series II: q **= 0.1,** N **= 2500, OUT**

model (μ)	$\langle t_{\rm cc}\rangle$	$\langle\Phi_{\rm min}\rangle$	$\langle r_{\rm c}\rangle$	$\langle N_{\rm c}\rangle$	$\langle\xi_{\rm min}\rangle$	$\langle N_{\rm esc}\rangle$	$\langle E_{\rm esc}\rangle$
A (1.25)	**673.7** ± 8.6	−**6.08** ±0.16	**0.0088** ±0.0004	**14.8** ±0.6	—	**61.4** ±2.5	**1.03** ±0.41
B (1.5)	**646.1** ±11.3	−**5.12** ±0.14	**0.0129** ±0.0008	**17.1** ±0.9	—	**50.1** ±2.5	**0.66** ±0.14
C (2.0)	**508.5** ±10.8	−**4.16** ±0.12	**0.0227** ±0.0014	**18.2** ±1.2	—	**32.6** ±1.6	**1.77** ±0.42
D (3.0)	**304.1** ± 7.3	−**3.23** ±0.05	**0.0476** ±0.0026	**24.8** ±1.8	—	**13.0** ±0.8	**1.10** ±0.30
E (5.0)	**153.7** ± 4.7	−**2.98** ±0.06	**0.0756** ±0.0042	**29.6** ±2.8	—	**8.5** ±0.6	**1.40** ±0.32
F (10.0)	**92.7** ± 3.0	−**3.23** ±0.08	**0.0892** ±0.0033	**23.8** ±1.6	—	**10.0** ±0.9	**2.17** ±0.47
G (25.0)	**52.5** ± 1.5	−**4.58** ±0.27	**0.0857** ±0.0037	**17.5** ±1.2	—	**17.0** ±1.6	**1.76** ±0.26
H (50.0)	**47.6** ± 2.3	−**6.86** ±0.29	**0.0664** ±0.0032	**9.7** ±0.7	—	**32.0** ±2.8	**1.94** ±0.32

Series III: q **= 0.05,** N **= 2500**

model (μ)	$\langle t_{\rm cc}\rangle$	$\langle\Phi_{\rm min}\rangle$	$\langle r_{\rm c}\rangle$	$\langle N_{\rm c}\rangle$	$\langle\xi_{\rm min}\rangle$	$\langle N_{\rm esc}\rangle$	$\langle E_{\rm esc}\rangle$
K (1.25)	**689.3** ± 7.8	−**5.88** ±0.21	**0.0094** ±0.0005	**16.0** ±0.6	**1.000** ±0.000	**60.7** ±2.5	**0.53** ±0.12
L (1.5)	**605.3** ±11.8	−**5.19** ±0.19	**0.0140** ±0.0009	**17.2** ±0.8	**1.001** ±0.000	**51.0** ±2.7	**0.61** ±0.16
M (2.0)	**428.8** ± 9.8	−**3.89** ±0.11	**0.0264** ±0.0022	**19.2** ±1.4	**1.009** ±0.008	**25.8** ±1.7	**0.82** ±0.28
N (3.0)	**219.3** ± 7.4	−**3.20** ±0.06	**0.0443** ±0.0028	**19.5** ±1.6	**1.092** ±0.034	**9.3** ±1.1	**0.85** ±0.27
P (5.0)	**96.1** ± 4.5	−**3.07** ±0.06	**0.0672** ±0.0046	**23.6** ±2.4	**1.510** ±0.034	**4.3** ±0.7	**1.60** ±0.54
Q (10.0)	**44.9** ± 1.4	−**3.34** ±0.11	**0.0896** ±0.0053	**23.5** ±2.4	**2.638** ±0.068	**4.2** ±0.6	**1.06** ±0.19
R (25.0)	**27.6** ± 1.2	−**4.53** ±0.21	**0.0903** ±0.0046	**19.0** ±1.9	**4.348** ±0.290	**9.0** ±1.4	**1.37** ±0.44

Series IV: q **= 0.2,** N **= 2500**

model (μ)	$\langle t_{\rm cc}\rangle$	$\langle\Phi_{\rm min}\rangle$	$\langle r_{\rm c}\rangle$	$\langle N_{\rm c}\rangle$	$\langle\xi_{\rm min}\rangle$	$\langle N_{\rm esc}\rangle$	$\langle E_{\rm esc}\rangle$
T (1.25)	**657.1** ±11.0	−**5.88** ±0.17	**0.0102** ±0.0006	**15.2** ±0.9	**1.001** ±0.000	**62.5** ± 2.6	**0.81** ±0.21
U (1.5)	**549.4** ± 7.6	−**5.00** ±0.14	**0.0134** ±0.0009	**14.6** ±0.8	**1.000** ±0.002	**49.5** ± 2.7	**1.17** ±0.28
V (2.0)	**343.8** ± 9.5	−**4.51** ±0.11	**0.0166** ±0.0011	**12.3** ±0.6	**1.067** ±0.012	**26.7** ± 2.2	**1.04** ±0.35
W (3.0)	**174.0** ± 3.9	−**3.87** ±0.11	**0.0244** ±0.0020	**11.8** ±0.8	**1.334** ±0.016	**16.9** ± 1.3	**0.61** ±0.04
X (5.0)	**86.3** ± 2.2	−**3.55** ±0.09	**0.0391** ±0.0028	**12.0** ±0.9	**2.069** ±0.059	**13.9** ± 0.8	**0.81** ±0.08
Y (10.0)	**48.6** ± 2.4	−**3.97** ±0.16	**0.0564** ±0.0041	**11.9** ±1.0	**4.063** ±0.161	**21.1** ± 1.6	**1.06** ±0.11
Z (25.0)	**22.7** ± 1.0	−**4.72** ±0.24	**0.0869** ±0.0049	**15.5** ±1.6	**9.676** ±0.267	**30.1** ±1.97	**0.74** ±0.07

Series V: q **= 0.4,** N **= 2500**

model (μ)	$\langle t_{\rm cc} \rangle$	$\langle \Phi_{\rm min} \rangle$	$\langle r_{\rm c} \rangle$	$\langle N_{\rm c} \rangle$	$\langle \xi_{\rm min} \rangle$	$\langle N_{\rm esc} \rangle$	$\langle E_{\rm esc} \rangle$
T*I* (1.25)	**639.7** ± 9.9	−**5.79** ±0.16	**0.0092** ±0.0007	**14.0** ±0.8	**1.000** ±0.000	**63.0** ±2.4	**0.68** ±0.13
U*I* (1.5)	**523.2** ± 8.2	−**5.24** ±0.12	**0.0117** ±0.0006	**14.4** ±0.8	**1.007** ±0.003	**51.4** ±2.7	**0.81** ±0.22
V*I* (2.0)	**372.3** ±10.3	−**4.95** ±0.15	**0.0149** ±0.0007	**13.3** ±0.6	**1.094** ±0.013	**42.3** ±2.9	**0.85** ±0.24
W*I* (3.0)	**212.8** ± 4.3	−**4.27** ±0.10	**0.0195** ±0.0014	**11.3** ±0.6	**1.436** ±0.039	**38.7** ±2.4	**0.57** ±0.03
X*I* (5.0)	**130.7** ± 4.0	−**4.19** ±0.14	**0.0274** ±0.0015	**10.4** ±0.6	**2.200** ±0.047	**43.7** ±2.9	**0.81** ±0.05
Y*I* (10.0)	**66.8** ± 2.5	−**4.26** ±0.12	**0.0440** ±0.0026	**9.9** ±0.5	**4.316** ±0.087	**50.9** ±3.5	**0.88** ±0.05

List of symbols

a	gravitational acceleration; eq. (42)
c	heat capacity, $dE/d\langle T\rangle$; eq. (9)
E	total energy of a cluster $E = K + W$; eq. (8), (60)
f	distribution function, eq. (1)
G	gravitational constant, $6.672{\cdot}10^{-11}$ $\mathrm{m^3kg^{-1}s^{-2}}$, in NB-units set to 1.
k_B	Boltzmann's constant, $k_\mathrm{B} = 1.3806 \cdot 10^{-23}$ $\mathrm{JK^{-1}}$; eq. (7)
K	total kinetic energy $K = \frac{1}{2}M\langle v^2\rangle$; eq. (23), (60)
m	mass of an individual particle
M_i	total mass of species i in a multi–component cluster; Ch. 6
M, M_tot	total mass of the cluster; Ch. 6
N	total number of stars; Ch. 6
N_c	number of stars inside core radius; Ch. 9.6
N_esc	number of escaped stars before core collapse time; Ch. 9.5
N_i	number of particles of species i in a multi–component cluster; Ch. 6; eq. (57)
q	mass fraction of heavy component; Ch. 6, eq. (55), (56)
r	distance from cluster centre
r_c	core radius; Ch. (9.1)
r_h	radius containing half the cluster mass
R	size of the cluster, equivalent to the virial radius $R = -GM^2/W$; eq. (60)
S_f	Scale factor for evolutionary time scales; Ch. (9.6), eq. (71)
t_cc	core collapse time; eq. (17), (65)
t_cr	crossing time $t_\mathrm{cr} = r/v$; eq. (12),
t_dyn	dynamical time $t_\mathrm{dyn} = \sqrt{3\pi/16G\rho}$; eq. (13)
t_eq	equipartition time; eq. (18)
t_rx	local relaxation time; eq. (14)
t_rh	relaxation time at half–mass radius r_h; eq. (15)
t_NB	time in Nbody units; Ch. 8.3, eq. (63)
T	Temperature of a point–mass system; eq. (7)
v	velocity of a star
v_esc	escape velocity; eq. (10)
W	total gravitational energy of the cluster; eq. (23), (60)
γ	factor in the Coulomb logarithm; Ch. 9.6
η	accuracy parameter for time steps; eq. (52)
μ	ratio of individual high and low mass stars; Ch. 6; eq. (55)
ξ	equipartition parameter; eq. (74)
ξ_min	value of closest approach to equipartition; Ch. 11
ρ	mean density inside the half–mass radius
ρ_c	density at cluster centre; Ch. 6
Φ	gravitational potential; eq. (2)
χ	critical value for mass instability; eq. (30)
$\langle ... \rangle$	average value of a quantity

Literaturverzeichnis

[1] **Aarseth S.J. (1963)**: *Mon. Not. Roy. Astron. Soc. 126*, p223

[2] **Aarseth S.J. (1985)**: "Direct methods for N–body simulations", in: *Multiple Time Scales*, Brackbill J. & Cohen B. (eds.), Ch. 12, p377

[3] **Aarseth S.J. (1993)**: "Direct methods for N–body simulations", in: *Galactic Dynamics and N–body simulations*, Contopoulos G. et. al. (eds.), Symposium in Thessaloniki, Greece

[4] **Aarseth S.J. (1999a)**: *Publ. Astron. Soc. Pac. 111*, p1333

[5] **Aarseth S.J. (1999b)**: *Celect. Mech. Dyn. Astron. 73*, p127

[6] **Aarseth S.J., Hénon M., Wielen R. (1974)**: *Astron. Astrophys. 37*, p183

[7] **Ahmad A. & Cohen L. (1973)**: *J. Comput. Phys. 12*, p389

[8] **Antonov, V.A. (1962)**: *Vest. Leningr. Gos. Univ. 7*, p135; English transl. in: *Dynamics of star clusters*, Goodman J. & Hut P. (eds.), IAU Symp. 113 (1985), p525

[9] **Bailyn C.D. (1992)**: *Annual Rev. Astron. Astrophys. 33*, p133

[10] **Baumgardt H. (2001)**: *Mon. Not. Roy. Astron. Soc. 325*, p1323

[11] **Baumgardt H., Hut P., Heggie D.C. (2002)**: *Mon. Not. Roy. Astron. Soc. 336*, p1069

[12] **Bettwieser E. & Inagaki S. (1985)**: *Mon. Not. Roy. Astron. Soc. 213*, p473

[13] **Binney J. & Tremaine S. (1987)**: *Galactic Dynamics*, Princeton University Press, New Jersey, USA

[14] **Bonnell I.A. & Davies M.B. (1998)**: *Mon. Not. Roy. Astron. Soc. 295*, p691

[15] **Chandrasekhar S. (1942)**: *Principles of Stellar Dynamics*, Chicago University Press, Illinois, USA

[16] **Chernoff D.F & Weinberg M.D. (1990)**: *ApJ 351*, p121

[17] **Cohn H. (1980)**: *ApJ 242*, p765

[18] **Deiters S., Fuchs B., Just A., Spurzem R., Wielen R. (2001)**: *"Dynamics of Star Clusters and the Milky Way"*, Proceedings of the star2000–Conference, A.S.P. Conf. Ser. 208, San Francisco, USA

[19] **Elson R.A.W. (1999)**: "Stellar Dynamics in Globular Clusters", p208 in: *Globular Clusters*, C. Martinez R. et. al. (eds.), X Canary Islands Winter School of Astrophysics, Cambridge University Press

[20] **Fregeau J.M, Joshi K.J., Portegies Zwart S.F., Rasio F.A. (2002)**: *ApJ 570*, p171

[21] **Giersz M. & Heggie D.C. (1994a)**: *Mon. Not. Roy. Astron. Soc. 268*, p257

[22] **Giersz M. & Heggie D.C. (1994b)**: *Mon. Not. Roy. Astron. Soc. 270*, p298

[23] **Giersz M. & Heggie D.C. (1996)**: *Mon. Not. Roy. Astron. Soc. 279*, p1037

[24] **Goodman J. (1987)**: *ApJ 313*, p576

[25] **Heggie D.C. & Mathieu R.D. (1986)**: "Standardised units and time scales", in: *The Use of Supercomputers in Stellar Dynamics*, Hut P. & McMillan S. (eds.), p233

[26] **Hénon M. (1965)**: *Ann. d'Astrophys. 28*, p62

[27] **Hénon M. (1969)**: *Astron. & Astrophys. 2*, p151

[28] **Hénon M. (1971)**: *Astrophys. Space Sci. 14*, p151

[29] **Hillenbrand L.A. & Hartmann L.W. (1998)**: *ApJ 492*, p492

[30] **Inagaki S. & Wiyanto P. (1984)**: *Publ. Astron. Soc. Japan 36*, p391

[31] **Khalisi E. & Spurzem R. (2001)**: *ASP Conf. Ser. 228*, p479; see [18].

[32] **King I.R. (1962)**: *Astron. J. 67*, p471

[33] **King I.R. (1966)**: *Astron. J. 71*, p64

[34] **Kustaanheimo P. & Stiefel E.L. (1965)**: *J. für Reine Angewandte Mathematik 218*, p204

[35] **Lightman A.P. & Fall S.M. (1978)**: *ApJ 221*, p567

[36] **Lynden–Bell D. & Wood R. (1968)**: *Mon. Not. Roy. Astron. Soc. 138*, p495

[37] **Makino J. (1991)**: *Publ. Astron. Soc. Japan 43*, p859

[38] **Makino J. & Aarseth S.J. (1992)**: *Publ. Astron. Soc. Japan 44*, p141

[39] **Makino J., Taji M., Ebisuzaki T., Sugimoto D. (1997)**: *ApJ 480*, p432

[40] **Meylan G. & Heggie D.C. (1997)**: *Astron. Astrophys. Rev. 8*, p1

[41] **Makino J. & Hut, P. (1988)**: *ApJ Suppl. 68*, p833

[42] **Michie R.W. (1963)**: *Mon. Not. Roy. Astron. Soc. 125*, p127

[43] **Mikkola S. (1997)**: "Numerical Treatment of Small Stellar Systems with Binaries", in: *Visual Double Stars: Formation, Dynamics and Evolutionary Tracks*, Docobo J.A., Elipe A., & McAlister H. (eds.), p269

[44] **Murray S.D. & Lin D.N.C. (1996)**: *ApJ 467*, p728

[45] **Plummer H.C. (1911)**: *Mon. Not. Roy. Astron. Soc. 71*, p460

[46] **Podsiadlowski P. & Price N.M (1992)**: *Nature 359*, p305

[47] **Quinlan G.D. (1996)**: *New Astronomy 1*, p255

[48] **Spitzer L. jr. (1940)**: *Mon. Not. Roy. Astron. Soc. 100*, p396

[49] **Spitzer L. jr. (1969)**: *ApJ 158*, L139

[50] **Spitzer L. jr. (1987)**: *Dynamical Evolution of Globular Clusters*, Princeton University Press, New Jersey, USA

[51] **Spurzem R. (1994)**: "Gravothermal Oscillations", in: *Ergodic Concepts in Stellar Dynamics*, Gurzadyan V.G. & Pfenniger D. (eds.), p170

[52] **Spurzem R. (1999)**: *J. Comput. Appl. Math. 109*, p407

[53] **Spurzem R. & Aarseth S.J. (1996)**: *Mon. Not. Roy. Astron. Soc. 282*, p19

[54] **Spurzem R., Khalisi E., Lin D.N.C. (2002)**: to be submitted to *Mon. Not. Roy. Astron. Soc.*

[55] **Spurzem R. & Takahashi K. (1995)**: *Mon. Not. Roy. Astron. Soc. 272*, p772

[56] **Sugimoto D. & Bettwieser E. (1983)**: *Mon. Not. Roy. Astron. Soc. 204*, p19P

[57] **Takahashi K. (1995)**: *Publ. Astron. Soc. Japan 47*, p561

[58] **von Hoerner S. (1960)**: *Zeitschrift f. Astrophysik 50*, p184

[59] **Watters W.A., Joshi K.J. & Rasio F.A. (2000)** *ApJ 539*, p331

[60] **Wielen R. (1971)**: *Astron. Astrophys. 13*, p309

[61] **Wielen R. (1975)**: "Dynamics of Star Clusters: Comparison of Theory with Observations and Simulations", in: *Dynamics of Stellar Systems*, IAU Symp. 69, Hayli A. (ed.), p119

Acknowledgements

I thank Prof. Dr. Roland Wielen for giving me the opportunity of writing this PhD–thesis at the Astronomisches Rechen–Institut, and Priv.–Doz. Dr. Rainer Spurzem who introduced the subject to me and conducted the details of the work throughout the years. Without his permanent and patient care the thesis would have never reached this form.
I am indebted to Dr. Holger Baumgardt (Tokyo/Japan), Prof. Dr. Mirek Giersz (Warsaw/Poland), and Dr. Marc Hemsendorf (Rutgers/USA) for many fruitful discussions, scientific assistance, and encouragement on various occasions. Dr. Chingis Omarov (Almaty/Kazachstan) helped in the utilization of the simulations on the CRAY T3E, and the Höchstleistungsrechenzentrum Stuttgart provided the platform for the performance of the parallel computations. Prof. Dr. Douglas Lin (Santa Cruz/USA) gave the idea to Chapter 10. I am also grateful to Prof. Dr. Hans–Walter Rix (Max–Planck–Institut für Astronomie, Heidelberg/Germany) who rendered an expert opinion for the work. Thanks also to the system administrator Dr. Peter Schwekendiek for giving valuable support in all questions about computers as well as all other colleagues and our working group. Financial support was given by the Astronomische Gesellschaft e.V. for the participation on several conferences and by the Astronomisches Rechen–Institut.
Last but not least, I thank my parents for the personal pre–education in order to achieve this academic step.